

THERMAL AND THERMOMECHANICAL STUDIES OF BEAM-BASED
POWDER-BED ADDITIVE MANUFACTURING PROCESSES

by

BO CHENG

Y. KEVIN CHOU, COMMITTEE CHAIR

K. CLARK MIDKIFF
PAUL G. ALLISON
MARK E. BARKEY
LAURENTIU NASTAC

A DISSERTATION

Submitted in partial fulfillment of the requirements
for the degree of Doctor of Philosophy
in the Department of Mechanical Engineering
in the Graduate School of
The University of Alabama

TUSCALOOSA, ALABAMA

2016

ABSTRACT

Powder-bed beam-based metal additive manufacturing (AM) such as electron beam additive manufacturing (EBAM) and selective laser melting (SLM) has a potential to offer innovative solutions to many challenges faced in the manufacturing industry. However, due to complex heat transport and thermomechanical interactions, the physical process of powder-bed AM has not been fully understood. This dissertation research focuses on the process thermal analysis, thermomechanical modeling and deformation studies of powder-bed metal AM parts.

The primary objectives of this research are: (1) to develop a 3D finite element (FE) thermal model to study the powder porosity effect in EBAM, validated by near infrared thermography; (2) to apply the developed thermal model and study, supported by experiments, the thermal response under different process parameters; (3) to simulate the SLM process using the developed 3D thermal model; (4) to develop a 3D thermomechanical FE model to study temperature, stress and deformation characteristics in EBAM overhang parts for different powder sintering conditions; (5) to investigate different support structures for overhang deformation in EBAM; (6) to investigate an overhang support design method for structure optimization.

The major findings are summarized as follows. (1) For beam process parameters of 632 mm/s speed, 6.7 mA current and 0.55 mm diameter, the peak temperature is ~ 2700 °C

and melt pool size is $2.94 \times 1.09 \times 0.12$ mm (length, width and depth). (2) Process parameters affect thermal characteristics. For 482 vs. 1595 mm/s speed, given 7.7 mA current and 0.65 mm diameter, the peak temperatures are 2572 vs. 2326 °C and the melt pool lengths are 2.35 vs. 1.25 mm. (3) In SLM, the residual heat can increase the melt pool size from raster scanning; e.g., the melt pool depth changes from ~0.085 mm to ~0.11 mm at given parameters. (4) In thermomechanical simulations, the results revealed that decreasing the powder-bed porosity (50% vs. 35%) can reduce the process temperatures, part residual stresses and overhang deformations. (5) A contact-free heat support beneath an overhang may effectively minimize overhang deformations. (6) The proposed support design methodology may eliminate part overhang deformations using less support materials.

LIST OF ABBREVIATIONS AND SYMBOLS

ABBREVIATIONS:

2D, 3D	Two Dimensional, Three Dimensional
2PP	Two Photon Polymerization
3DP	Three Dimensional Printing
AM	Additive Manufacturing
ASTM	American Society for Testing and Materials
CAD	Computer-Aided Design
DoD	Drop on Demand
DPP	Dry Powder Printing
DMD	Directed Metal Deposition
EBM	Electron Beam Melting
EBAM	Electron Beam Additive Manufacturing
FE	Finite Element
LENS	Laser Engineering Net Shape
LOM	Laminated Object Material
NASA	National Aeronautics and Space Administration
NIR	Near Infrared
NIST	National Institute of Standards and Technology

PJT	PolyJet Technology
SF	Speed Function
SMS	Selective Mask Sintering
SL	Stereolithography
SLM	Selective Laser Melting
SLS	Selective Laser Sintering
UC	Ultrasonic Consolidation

SYMBOLS:

d_P	Beam Penetration Depth
f	Volumetric Fraction of Liquid
I_b	Electron Beam Current
L_f	Latent Heat of Fusion
T	Temperature
t_{layer}	Powder Layer Thickness
T_L	Liquidus Temperature
$T_{preheat}$	Preheating Temperature
T_{ref}	Reference Temperature
T_S	Solidus Temperature
U_o	Acceleration Voltage
c	Specific Heat Capacity

ρ	Density
k	Thermal Conductivity
v_s	Beam Scanning Speed
Φ_E	Beam Diameter
η	Beam Absorption Efficiency
φ	Powder Porosity
ε	Emissivity
P	Laser Beam Power
α_e	Coefficient of Expansion
$\{\varepsilon\}$	Total Strain Matrix
$\{\varepsilon^{th}\}$	Thermal Strain Matrix
$[D]$	Stress–strain Matrix
$\{\sigma\}$	Stress Matrix
$\sigma_{allowable}$	Allowable Stress
$\sigma_{i,j...}$	The Stress of Anchor $i, j \dots$
$\delta_{allowable}$	Allowable Deformation Tolerance
δ_{range}	User-defined Deformation Tolerance Range
$U_{current}$	Current Step Overhang Deformation
U_k	Overhang Deformation of K's Iteration
$U_{required}$	Ideal Overhang Deformation (for All Solid Substrate Case)
$U_{support}^k$	Overhang Deformation of K's Iteration with The Application of Heat Support

v^i, v^j	Vertices i, j
V_{current}	Current Support Anchor Volume
L_{overhang}	The Overhang Length
$X_{\vec{v}^j}$	X-direction Distance To Overhang Edge for v^j

ACKNOWLEDGMENTS

First and foremost, my most sincere thanks go to my advisor, Dr. Kevin Chou, for his endless encouragement, generous advice, and support during my Ph.D. period. I would not be where I am today without Dr. Chou's academic insights and expertise. In addition, I would like to thank him for introducing me to the wonders of scientific world.

Also, I would like to express my grateful acknowledgement to my committee members, Dr. K. Clark Midkiff, Dr. Paul G. Allison, Dr. Mark E. Barkey, Dr. Laurentiu Nastac, for their helpful advices and inspiring discussions on this work.

I want to express my sincere gratitude for my friends at The University of Alabama (UA) throughout my study. Special thanks to the past and present members in our group, Dr. Ping Lu, Dr. Xibing Gong, Mr. Steven Price, Mr. Subin Shrestha, Ms. Tahmina Keya, Mr. Xiaoqing Wang, for their assistance in my research.

Special thanks are also extended to UA and the Mechanical Engineering Department for providing me with such a wonderful opportunity to pursue my Ph.D. study in Tuscaloosa.

I would also like to thank the financial support from NASA (No. NNX11AM11A) and National Science Foundation (CMMI 1335481). Financial supports from UA Graduate Council Fellowship and the AL EPSCoR GRSP are also acknowledged.

Last but not least, I would like to give my eternal gratitude to my beloved parents, my uncle's family and my extended families, for their love, and for always being there for me.

CONTENTS

ABSTRACT.....	ii
LIST OF ABBREVIATIONS AND SYMBOLS	iv
ACKNOWLEDGMENTS	viii
LIST OF TABLES	xiv
LIST OF FIGURES	xv
CHAPTER 1 INTRODUCTION	1
1.1 Background and Motivation.....	1
1.2 Research Objectives and Scope.....	9
1.3 Outline.....	10
References	11
CHAPTER 2 LITERATURE REVIEW.....	13
2.1 Powder Bed AM Process Thermal Modeling.....	13
2.2 Process Parameters Study for Electron and Laser Melting Process.....	16
2.3 Thermomechanical Modeling of Powder Bed AM	21
2.3.1 General Metal AM Numerical Study	21
2.3.2 Powder-bed EBAM Thermomechanical Study.....	23
References	24
CHAPTER 3 ON PROCESS TEMPERATURE IN POWDER-BED ELECTRON BEAM	

ADDITIVE MANUFACTURING: MODEL DEVELOPMENT AND VALIDATION.....	29
Abstract	29
3.1 Introduction	30
3.2 Modeling and Simulation	33
3.2.1 Thermal Modeling.....	33
3.2.2 Finite Element Methodology	38
3.3 Results and Discussion.....	41
3.3.1 Typical Simulation Example.....	41
3.3.2 Powder Porosity Effect	45
3.4 Conclusion.....	48
Acknowledgements	49
References	49
 CHAPTER 4 ON PROCESS TEMPERATURE IN POWDER-BED ELECTRON BEAM ADDITIVE MANUFACTURING: PROCESS PARAMETER EFFECTS.....	 52
Abstract	52
4.1 Introduction	53
4.2 Research Approach.....	54
4.3 Results and Discussion.....	57
4.3.1 Beam Speed Effects.	57
4.3.1.1 Part Surface Morphology and Microstructures.....	57
4.3.1.2 Simulation Result Comparisons	60
4.3.2 Beam Current and Beam Diameter Effects.....	63

4.4 Conclusion.....	66
Acknowledgements	67
References	67
CHAPTER 5 MELT POOL EVOLUTION STUDY IN SELECTIVE LASER MELTING ...	69
Abstract	69
5.1 Introduction	69
5.2 Selective Laser Melting Model Construction.....	73
5.2.1 Governing Equation	73
5.2.2 Heat Input Equation	73
5.2.3 Material Property Modeling.....	74
5.2.4 Model Configuration.....	76
5.3 Results and Discussion.....	78
5.3.1 Model Validation.....	78
5.3.2 Typical Example of Simulated Results	79
5.3.3 Raster Length Effect on Melt Pool Evolution.....	81
5.3.4 Process Parameters Effect.....	83
5.4 Conclusion.....	84
Acknowledgements	85
References	85
CHAPTER 6 THERMOMECHANICAL INVESTIGATION OF POWDER SINTERING EFFECT FOR OVERHANG FABRICATIONS IN ELECTRON BEAM ADDITIVE MANUFACTURING.....	89

Abstract	89
6.1 Introduction	90
6.2 Finite Element Modeling Approach	94
6.3 Results and Discussion.....	97
6.3.1 Typical Example of Simulation Results.....	97
6.3.2 Powder Sintering Effect Analysis	101
6.4 Conclusion.....	105
Acknowledgements	105
References	105
CHAPTER 7 GEOMETRIC CONSIDERATION OF SUPPORT STRUCTURES IN PART OVERHANG FABRICATIONS BY ELECTRON BEAM ADDITIVE MANUFACTURING.....	107
Abstract	107
7.1 Introduction	108
7.2 Finite Element Modeling for Overhang Study.....	112
7.2.1 Thermal Analysis	112
7.2.2 Structural Analysis	112
7.2.3 Material Properties Modeling	113
7.2.4 Numerical Model Configuration.....	113
7.3 Overhang and Support Structure Simulation Study	117
7.4 Results and Discussion.....	122
7.4.1 Overhang Length Effect.....	122

7.4.2 Support Column Effect	123
7.4.3 Solid Piece Gap Effect	125
7.5 Conclusion.....	129
Acknowledgements	130
References	130
CHAPTER 8 SUPPORT STRUCTURE DESIGN FOR OVERHANG FABRICATION IN ELECTRON BEAM ADDITIVE MANUFACTURING	133
Abstract	133
8.1 Introduction	134
8.2 Support Structure Design Framework.....	137
8.3 Simulation Based Support Structure Design Procedure.....	139
8.4 Finite Element Model Configuration	142
8.5 Results and Discussion.....	143
8.5.1 Typical Process for Heat Support Design	143
8.5.2 Typical Process for Anchor Support Design	145
8.6 Conclusion.....	150
References	150
CHAPTER 9 CONCLUSIONS AND RECOMMENDATIONS FOR FUTURE RESEARCH.....	152
9.1 Conclusions	152
9.2 Contributions of This Study	154
9.3 Recommendations for Future Research	155

LIST OF TABLES

Table 1.1. AM classification (Vaezi <i>et al.</i> , 2013).....	2
Table 3.1. Parameter list used in EBAM simulations.....	40
Table 5.1. Parameter list used in simulations for In718.	77
Table 5.2. Simulation and experiment comparison.	78
Table 6.1. Melt pool size dimension of layer-1(unit: μm).....	99

LIST OF FIGURES

Figure 1.1. General AM process.....	3
Figure 1.2. Schematic of EBAM process.....	5
Figure 1.3. Schematic of an EBAM machine (Jamshidinia <i>et al.</i> , 2013a).....	6
Figure 1.4. EBAM Machine: (a) overall outside, (b) inside of the build chamber.....	7
Figure 1.5. Metal parts build by electron beam melting:(a) car upright, (b) thigh bone and (c) dental implant.	8
Figure 3.1. Temperature dependent specific heat, density and thermal conductivity of Ti-6Al-4V (Mills, 2002; Rai, 2008; Yang <i>et al.</i> , 2010).....	36
Figure 3.2. Temperature dependent thermal conductivity.	38
Figure 3.3. An illustration of thermal model and part geometry in finite element simulations.	39
Figure 3.4. Typical simulation result: (a) temperature contour with melt pool geometry, (b) temperature profile, and (c) cooling rate.	42
Figure 3.5. Temperature comparisons between simulation and experiment ($v= 632.6$ mm/s, $i = 6.7$ mA, $d= 0.55$ mm): (a) contour, and (b) profile.	44
Figure 3.6. Model validation with another set of experiments with repeated tests ($v= 728$ mm/s, $i = 7.2$ mA, $d= 0.55$ mm).	45
Figure 3.7. Temperature contours and molten pool geometries for powder layer of various levels of porosity.....	47
Figure 3.8. Simulated melt pool sizes for different levels of powder porosity for the top layer.....	47

Figure 3.9. Simulated temperatures comparing profiles between using powder vs. solid properties as the top layer.	48
Figure 4.1. A CAD model used in EBAM experiments for temperature measurements.....	56
Figure 4.2. Fabricated parts from EBAM experiments with different speed function (SF) values.	58
Figure 4.3. EBAM build part surface morphology vs. SF: (a) stereoscopic images, (b) white-light interferometric images, and (c) surface roughness.	59
Figure 4.4. Cooling rates associated with different beam speeds.	60
Figure 4.5. Temperature profile comparisons, simulation vs. experiment, for 4 beam speeds	62
Figure 4.6. Melt pool size comparisons, simulation vs. experiment, for 4 SF values: (a) length, and (b) width.	63
Figure 4.7. Melt pool size and shape illustration (simulations) at 4 different beam speeds. ...	63
Figure 4.8. Beam current effects on EBAM process temperatures, simulation vs. experiment: (a) profile, and (b) melt pool size ($v= 506$ mm/s, $d=0.65$ mm).	64
Figure 4.9. Beam diameter effects on EBAM process temperatures, simulation vs. experiment: (a) profile, and (b) melt pool size ($v= 671$ mm/s, $i= 6.7$ mA).	66
Figure 5.1. Patch scanning strategy.	71
Figure 5.2. In718 solid (Dye <i>et al.</i> , 2001) and powder thermal properties.....	76
Figure 5.3. An example of 3D FEM model for multi-path scanning with fine mesh.....	77
Figure 5.4. Comparison between SLM simulation and literature data for In718.	78
Figure 5.5. Comparison between SLM simulation and literature data for Ti64.	79
Figure 5.6. Example of temperature and melt pool evolution in raster scan.	80
Figure 5.7. (a) Max melt pool size in different raster path, (b) melt pool shape.	81
Figure 5.8. Melt pool evolution in a single track.	82

Figure 5.9. Melt pool size in different scanning path.	83
Figure 5.10. Melt pool length evolution vs. different process parameters.	84
Figure 5.11. Raster length effect on different process parameters cases.	84
Figure 6.1. Required support structures in SLM process (Mumtaz <i>et al.</i> , 2011).....	91
Figure 6.2. (a) Anchorless Bi3Zn SLM part (Mumtaz <i>et al.</i> , 2011); (b) Ti6Al4V-10Cu EBAM part (Vora <i>et al.</i> , 2013).	92
Figure 6.3. (a) Part mesh and geometry, and (b) scan pattern.	95
Figure 6.4. Temperature dependent material mechanical properties of Ti-6Al-4V (Huang <i>et al.</i> , 2008).	96
Figure 6.5. Temperature contour (top view) at the end of three-layer deposition.	97
Figure 6.6. (a) Nodes location at first layer (scanning region), and (b) Temperature history information of the 2 nodes above powder and solid substrates.	98
Figure 6.7. Temperature profiles around electron beam center (0 mm) above solid and powder substrates for initial and final path of layer-1.	99
Figure 6.8. Melt pool size and shape of layer-1 in the powder and solid substrates at initial and final scanning paths.....	99
Figure 6.9. von Mises stress contour after final cooling (powder hidden).	100
Figure 6.10. von Mises stress evolution of 2 nodes above solid and powder substrates.	101
Figure 6.11. Temperature profiles on the scanning paths for two different powder porosity levels.	102
Figure 6.12. von Mises stress comparison after final cooling for different powder porosity levels	103
Figure 6.13. von Mises stress on different scanning paths of the third layer after final cooling for the models with different porosity levels.	104
Figure 7.1. An example of overhang model and associated warping defect.	111

Figure 7.2. Model geometric information.....	114
Figure 7.3. Flow chart of numerical simulation procedure used for the overhang model developed for EBAM.....	116
Figure 7.4. Temperature induced deformation.	117
Figure 7.5. Temperature contours of electron beam scanning on layer-2 for overhang substrate vs. solid substrate cases.	119
Figure 7.6. (a) and (b) Typical example of residual stress contours after final cooling (to room temperature); (c) typical example of top surface deformation plots after final cooling.	120
Figure 7.7. Geometric considerations of different support structure.....	122
Figure 7.8. (a) Typical example of deformation contours after final cooling for overhang length case (L=15 mm); (b) different overhang lengths (top surface deformation plots).	123
Figure 7.9. Typical example of deformation contours and top surface deformation plots after final cooling for $W_c=1.0$ mm case.	124
Figure 7.10. Simulation results comparison of different support column material usage cases (top surface deformation plots).	125
Figure 7.11. Typical example of deformation contours and top surface deformation plots after final cooling for Gap=0.63 mm case.	127
Figure 7.12. (a) Typical example of temperature plots (inter-cooling step between layer-2 and layer-3); (b) temperature contours (electron beam scanning on layer-3); (c) deposited layer top surface temperature profiles (electron beam scanning on layer-3).....	128
Figure 7.13. Simulation results comparison of different gap distance cases (top surface deformation plots).....	129
Figure 8.1. General idea of stress related support distribution.	138
Figure 8.2. Overhang support design flow chart.....	142
Figure 8.3. Model meshing and geometrical information.....	143

Figure 8.4. Deformation comparison of heat support cases and non-heat support case..... 145

Figure 8.5. Deformation comparison between first layer (cooled to preheating temperature) and all 3 layer deposition (cooled down to room temperature). 146

Figure 8.6. Empirical design of initial (1st round) support anchor, and deformation comparison after first layer deposition between with/without anchor support cases. 147

Figure 8.7. Second round support anchor application. 148

Figure 8.8. Third round support anchor application. 149

CHAPTER 1

INTRODUCTION

1.1 Background and Motivation

Additive Manufacturing (AM) is defined by a range of technologies that are capable of translating virtual solid model data into physical models in a quick and easy process. Generally, three dimensional data of solid object is broken down into a series of 2D cross-sections of a finite thickness. Then the generated cross-sections are fed into AM machines so that they can be combined, adding them together in a layer-by-layer fashion to form the physical part. The build part is reproduced without having to adjust for manufacturing processes, e.g., tooling, undercuts, draft angles or other features (Gibson *et al.*, 2010).

Although there are a large number of technologies in this field, such as selective laser melting (SLM), Laminated Object Material (LOM), Laser Engineering Net Shape (LENS) and Fused Deposition Modeling (FDM), AM technologies have been standardized and classified by the ASTM International Committee F42 into seven areas listed below and their process description, typical techniques and material usages are summarized in Table 1.1 (Vaezi *et al.*, 2013; Monzón *et al.*, 2014).

1. Vat photopolymerization;
2. Material extrusion;
3. Powder bed fusion;
4. Directed energy deposition;

5. Sheet lamination;

6. Material jetting;

7. Binder jetting.

Table 1.1. AM classification (Vaezi *et al.*, 2013)

Process	Description	Typical Techniques	Materials
Photopolymer vat	Liquid photopolymer is selectively cured using a light source	SL, 2PP	Photo-curable polymers
Material extrusion	Material selectively is dispensed through a nozzle or extruder	Extrusion freeforming techniques	Polymers, ceramics, metals
Powder-bed fusion	Thermal energy selectively fuses regions of powder-bed material	SLS, SLM, EBM, SMS	Polymers, Metals, Ceramics
Directed energy deposition	Focused thermal energy melts materials as deposited	LENS, DMD	Metals, ceramics
Sheet lamination	Material sheets are bonded together and selectively cut in each layer to create a desired 3D object	LOM, UC	Metals, Ceramics, Polymers
Material jetting	Droplets of build material are selectively deposited layer by layer	DoD Inkjet printing, PJT	Polymers, metals, ceramics
Binder jetting	Liquid bonding ink is selectively spread to join solid powder material	3DP	Polymers, Metals, Ceramics

Despite tremendous technologies and industrial applications, they share almost the same processing steps, to some degree at least, from virtual model to physical part. Different products will involve AM in different ways and to different degrees. Generally, all AM parts start from computer aided design model and transfer to machine by required data conversion method, then the part building will be processed mainly in any kind of AM machines, finally part post process such as cleaning may be needed before actual usage. Figure 1.1 has clearly shows generally process of any AM technology.

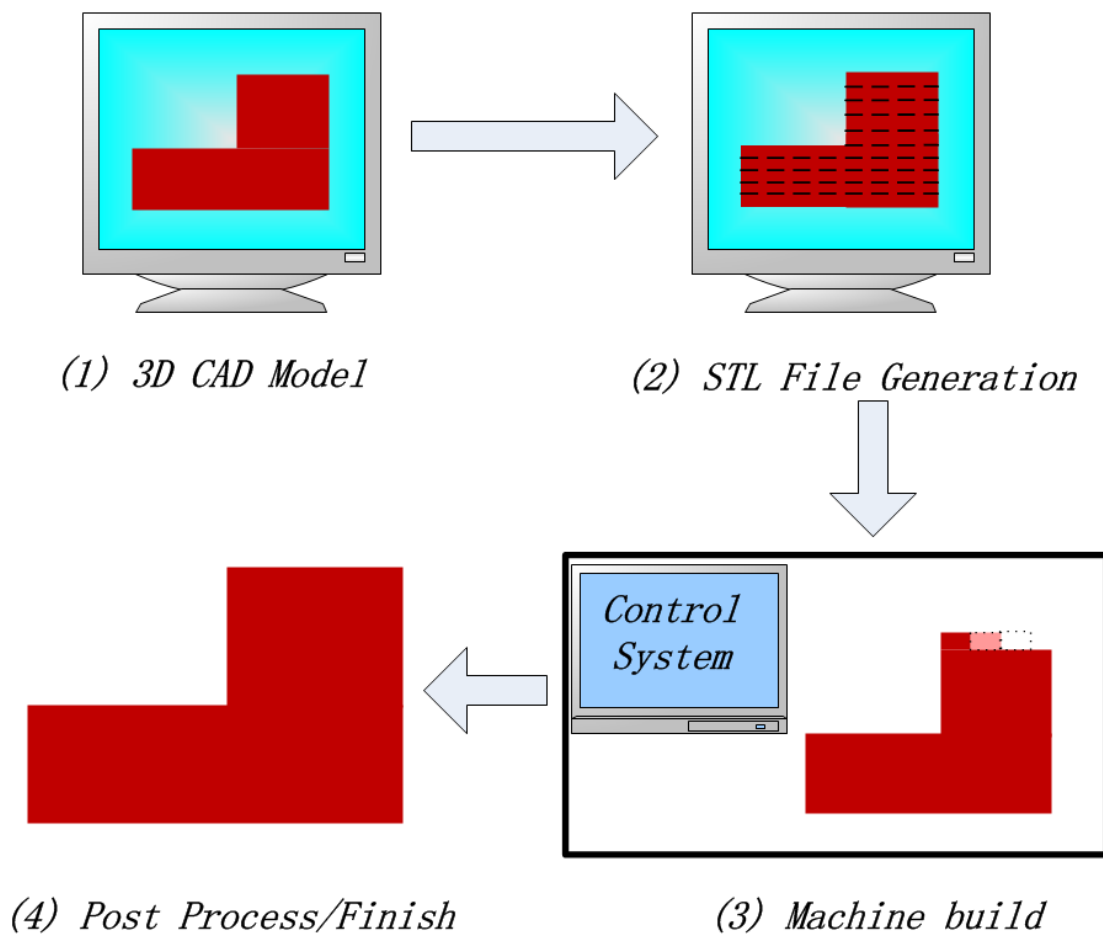


Figure 1.1. General AM process.

When compared to traditional manufacturing processes, additive manufacturing technologies have the following major advantages (Huang *et al.*, 2013):

- (1) Material efficiency: AM utilizes raw materials efficiently by building parts layer

by layer with minimum material requirement while large amount of materials need to be removed in traditional subtractive manufacturing.

(2) Resource efficiency: AM does not require additional resources such as fixtures and cutting tools in addition to the main machine tool in traditional manufacturing processes.

(3) Part flexibility: AM parts with complex features are made possible due to no tooling constraints in manufacturing process.

(4) Production flexibility: no costly setups requirements are for AM machines thus they are economical in small batch production. In addition, the quality of the parts depends on the manufacturing process rather than personal skills.

Although additive manufacturing has noticeable advantages, some challenges and drawbacks are still needed to be solved:

(1) Geometric accuracy: material shrinkage and distortion problem during AM process would affect build part dimensional accuracy (Paul *et al.*, 2014).

(2) Process control: AM building process parameters should be controlled to maintaining good dimensional accuracy (Sammons *et al.*, 2013)

Among all the other AM technologies, the powder-based electron beam additive manufacturing (EBAM), developed and commercialized by Arcam AB in recent years, provides an effective alternative for processing of titanium (Ti) alloy and also other metal alloys parts used in different industries. EBAM utilizes a high-energy electron beam, as a moving heat source, to melt and fuse metal powders and fabricate parts in a layer-by-layer building fashion in the powder-bed chamber under vacuum condition. The major process steps of EBAM, shown in Figure 1.2, include distributing powder layers, powder preheating,

and selectively powder melting, etc. In preheating, the system utilizes a high-energy focused electron beam to raster-scan at a high speed, e.g., 15 m/sec, and at a high beam current (~30 mA) to lightly sinter the top powder layer. The process is followed by melting, contour-melting and hatch-melting, in a selective area, driven by three-dimensional (3D) CAD data. After the completion of one layer building, another layer of powder will be distributed, preheated, and selectively melted, with such a cycle repeated. The build process occurs in a chamber with a nominal vacuum of 10^{-4} torr (Gaytan *et al.*, 2009).

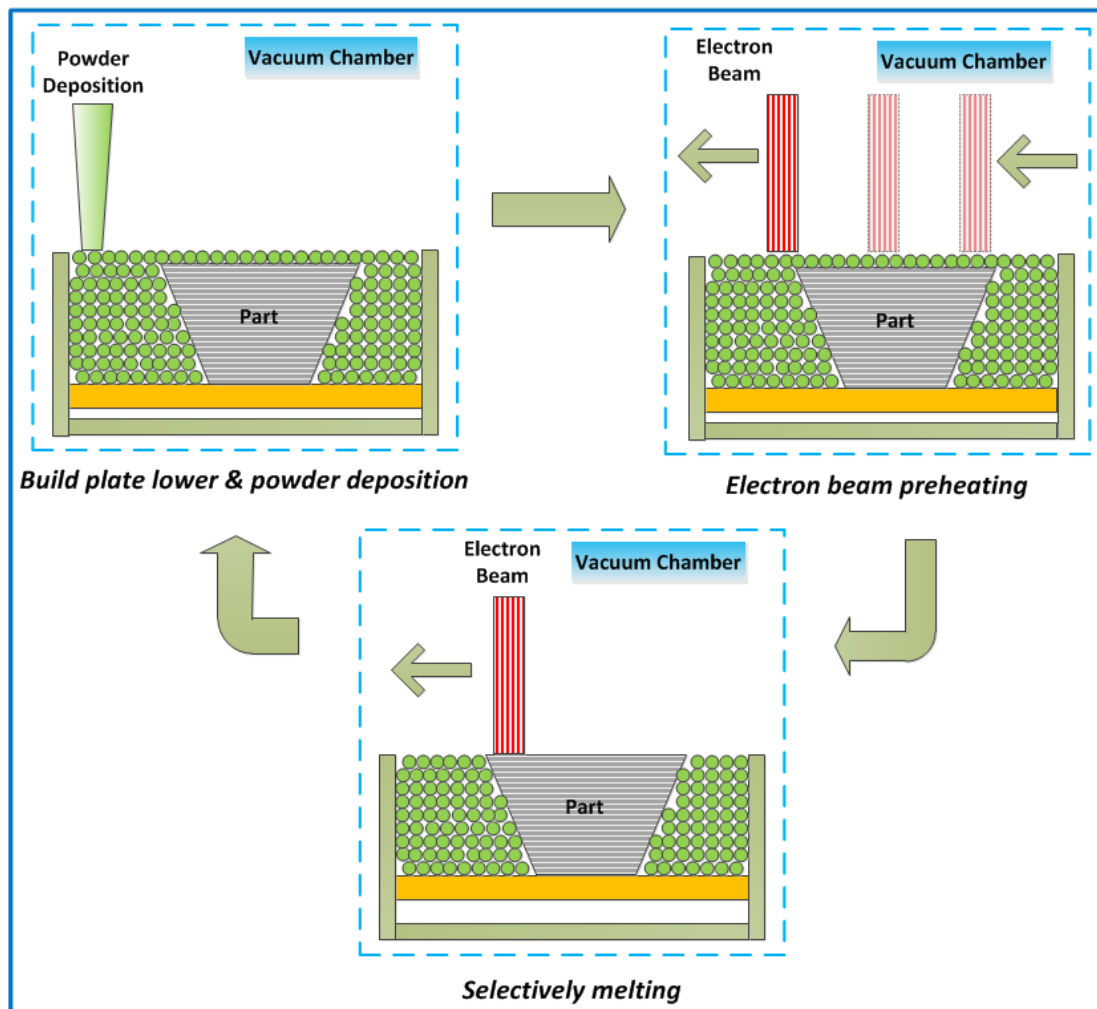


Figure 1.2. Schematic of EBAM process

The principle of general EBAM machine is very similar to that of a scanning electron microscope. A heated tungsten filament emits electrons which are accelerated to certain

kinetic energy (e.g., ~ 60 keV). The electron beam is controlled by two magnetic coils that the first magnetic lens is applied to focus the beam to desired diameter while the second one deflects the focused beam to the desired region on the building area (Biamino *et al.*, 2011).

Figure 1.3 describes general configuration of an EBAM machine.

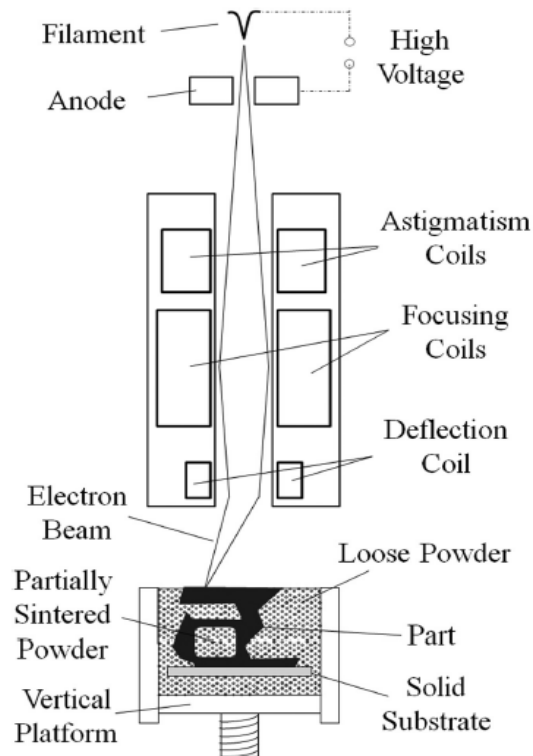


Figure 1.3. Schematic of an EBAM machine (Jamshidinia *et al.*, 2013a)

Figure 1.4 shows an example of an Arcam S12 EBAM system. The electron gun is located in the upper area of the machine while the main build chamber is placed below. The viewport has a glass window through which actual building process in the build chamber could be observed. Unused powder will be stored in the powder hopper and be spread in a layer-by-layer fashion with certain layer thickness. Build plate is used to hold entire powder-bed and lower down at one layer thickness at a time. Slit area is noted on the heat shield that covers the build area, thus observation from outside is made possible.

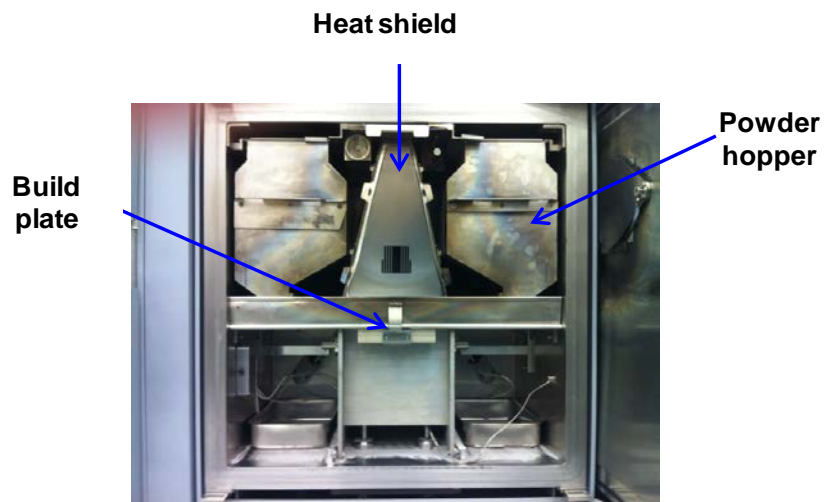
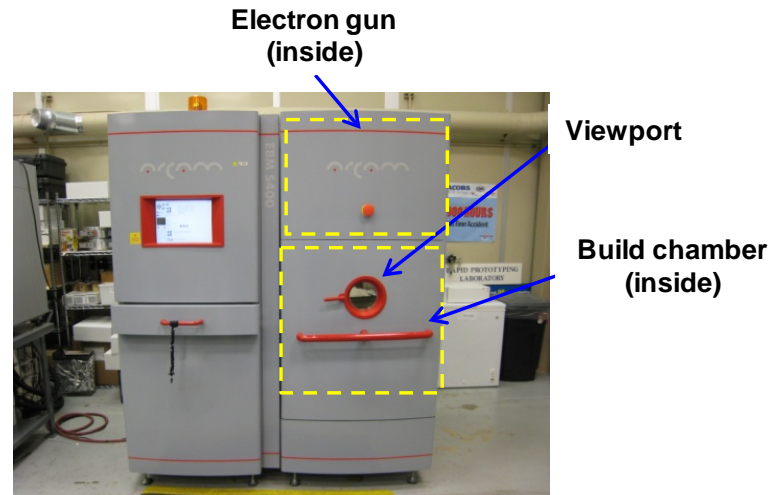


Figure 1.4. EBAM Machine: (a) overall outside, (b) inside of the build chamber.

Because EBAM has many unique characteristics such as high energy efficiency, high scan speed, and moderate operation cost, the technology has attracted, in recent years, increased interests from different industries. The use of an electron beam offers extensive features such as higher build rates due to increased penetration depths and rapid scanning speeds. Many researchers have been studying the EBAM technology from different aspects and for various applications. There are frequently reported EBAM part designs, such as race car upright (Petrovic *et al.*, 2011), thigh bone (Qi *et al.*, 2006) and dental implant (Chahine *et al.*, 2009), shown in Figure 1.5.

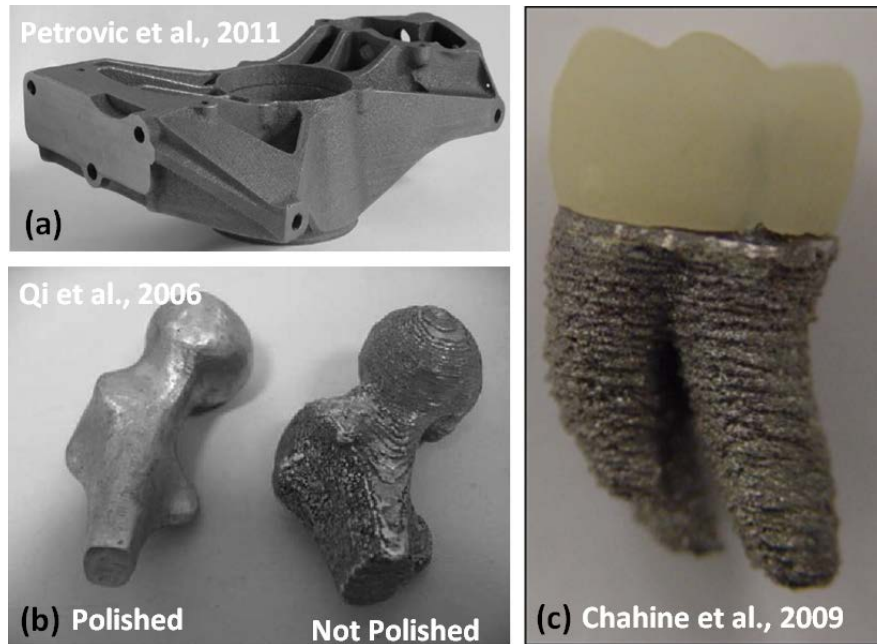


Figure 1.5. Metal parts build by electron beam melting:(a) car upright, (b) thigh bone and (c) dental implant.

However, there are several process difficulties such as melt ball formation and layer delamination (Zäh and Lutzmann, 2010) in EBAM that prevent wide industrial applications. In addition, process aspects, such as the thermal response and thermomechanical phenomenon of the EBAM process, still need to be fully understood. Thus, the understanding and controlling the EBAM process, as well as other powder bed AM process, are of great importance for build part quality control.

First, the thermal response is complicated in powder bed AM process. The powder material has different thermal properties with solid material, thus powder porosity may play a key role on process temperature distributions. The experimental calibration of powder conductivity is also of great interest, it helps to improve model predicting accuracy.

Second, the influence of process parameters on part quality is still unknown. Three beam process parameters, namely, beam speed, diameter and current, which would affect the melt pool size, are critical to influence the final part quality. In addition, the resulted cooling

rate may affect the microstructure evolution of the build components.

Third, the investigation of thermomechanical characteristics in overhang fabrications has not been fully studied yet, very few literatures concerning thermomechanical study could be found. In addition, the geometrical considerations of overhang supporting structures are needed since the understanding of part warping problem could help to improve part quality.

1.2 Research Objectives and Scope

This research intends to investigate the thermal as well as thermomechanical characteristics in powder bed additive manufacturing process, with objectives centered on a better understanding of temperature distribution, process parameter effect, residual stress as well as part distortion.

The objectives of this research include the following.

1. To create a 3D numerical thermal model incorporating temperature dependent material properties, moving heat source and latent heat of fusion to investigate the effect of powder porosity in EBAM process.
2. To validate the developed thermal model with experiments.
3. To investigate the process parameters effect on temperature distribution, melt pool size as well as part surface quality through numerical modelling.
4. To extend the thermal model for SLM process.
5. To create a 3D numerical thermomechanical model incorporating layer addition feature to study the powder sintering effect in overhang process.
6. To create a 2D numerical multi-layer thermomechanical model to initially study the warping problems in overhang fabrications.

7. To develop an overhang support design method framework.

This study would provide contributions to the fundamental understanding of thermomechanical response of powder bed additive manufacturing process. Based on these investigations, process optimizations may be provided for part quality control.

First of all, a finite element (FE) EBAM thermal model will be constructed based on the physical process and actual boundary conditions will be included. Validation with experiments about process temperature measurement will be conducted. Then temperature distributions, powder porosity effect as well as process parameter effect on thermal response will be investigated utilizing the FE model. This thermal model will be extended to simulate the thermal response in SLM raster scan process. Based on the thermal model, thermomechanical model will also be created to study various temperature and stress issues in EBAM overhang fabrication. In addition, overhang support design framework will be proposed to generate support structures with the minimum material usage.

1.3 Outline

The layout of this proposal is as followings:

Chapter 2 presents a literature review on the powder bed AM technology, thermal simulation of general metal AM, and also the thermomechanical modeling method of metal AM including SLM and EBAM process.

In Chapter 3, a novel thermal model about EBAM process is developed. The FE model is first verified with experiment results, and then the powder porosity effects on temperature characteristics are studied.

In Chapter 4, numerical studies of process parameters effect have been presented. The FE model developed in Chapter 3 is extended to investigate beam speed, current as well as diameter effect on melt pool sizes and temperature distributions.

In Chapter 5, the developed thermal model is applied to study the temperature distribution and melt pool evolution in SLM process.

In Chapter 6, a 3D thermomechanical FE model is developed and applied to study the temperature and stress problem in overhang structure with the consideration of different powder sintering conditions.

In Chapter 7, a 2D thermomechanical FE model is developed and applied to study the different geometric considerations of part overhang and support design.

In Chapter 8, the 3D thermomechanical FE model is utilized to develop a novel overhang support design method.

The last chapter proposed the future work of this research.

References

- Biamino, S., Penna, A., Ackelid, U., Sabbadini, S., Tassa, O., Fino, P., Badini, C. (2011). Electron beam melting of Ti-48Al-2Cr-2Nb alloy: microstructure and mechanical properties investigation. *Intermetallics*, 19(6), 776-781.
- Chahine, G., Atharifar, H., Smith, P., & Kovacevic, R. (2009). Design Optimization of a Customized Dental Implant Manufactured via Electron Beam Melting®. *International Solid Freeform Fabrication Symposium*, Austin, TX, USA, August 3-5, 2009, 631-640.
- Gaytan, S. M., Murr, L. E., Medina, F., Martinez, E., Lopez, M. I., & Wicker, R. B. (2009). Advanced metal powder based manufacturing of complex components by electron beam melting. *Materials Technology*, 24, 180-190.
- Gibson, I., Rosen, D. W., & Stucker, B. (2010). *Additive manufacturing technologies*: Springer.

- Huang, S. H., Liu, P., Mokasdar, A., & Hou, L. (2013). Additive manufacturing and its societal impact: a literature review. *The International Journal of Advanced Manufacturing Technology*, 67(5-8), 1191-1203.
- Jamshidinia, M., Kong, F., & Kovacevic, R. (2013). Numerical modeling of heat distribution in the electron beam melting® of Ti-6Al-4V. *Journal of Manufacturing Science and Engineering*, 135(6), 061010.
- Monzón, M., Ortega, Z., Martínez, A., & Ortega, F. (2014). Standardization in additive manufacturing: activities carried out by international organizations and projects. *The International Journal of Advanced Manufacturing Technology*, 1-11.
- Paul, R., Anand, S., & Gerner, F. (2014). Effect of thermal deformation on part errors in metal powder based additive manufacturing processes. *Journal of Manufacturing Science and Engineering*, 136(3), 031009.
- Petrovic, V., Vicente Haro Gonzalez, J., Jorda Ferrando, O., Delgado Gordillo, J., Ramon Blasco Puchades, J., & Portoles Grinan, L. (2011). Additive layered manufacturing: sectors of industrial application shown through case studies. *International Journal of Production Research*, 49(4), 1061-1079.
- Qi, H., Yan, Y., Lin, F., He, W., & Zhang, R. (2006). Direct metal part forming of 316L stainless steel powder by electron beam selective melting. *Proceedings of the Institution of Mechanical Engineers, Part B: Journal of Engineering Manufacture*, 220(11), 1845-1853.
- Sammons, P. M., Bristow, D. A., & Landers, R. G. (2013). Height dependent laser metal deposition process modeling. *Journal of Manufacturing Science and Engineering*, 135(5), 054501.
- Vaezi, M., Chianrabutra, S., Mellor, B., & Yang, S. (2013). Multiple material additive manufacturing – Part 1: a review. *Virtual and Physical Prototyping*, 8(1), 19-50.
- Zäh, M. F., & Lutzmann, S. (2010). Modelling and simulation of electron beam melting. *Production Engineering. Research and Development*, 4, 15-23.

CHAPTER 2

LITERATURE REVIEW

The objective of this research is to investigate thermal and thermomechanical characteristics of powder bed AM process by experiments as well as by means of finite element method. This chapter presents a literature review of fundamentals of thermal and thermomechanical modeling studies, especially with a focus on EBAM process.

2.1 Powder Bed AM Process Thermal Modeling

Though there is a large pool of powder bed AM literature, the primary focus has been part microstructures, properties and different applications, etc., while modeling of the AM process has been relatively rare. The process physics of powder bed AM is complex and challenging to model, which involves mass and heat transport, phase changes, and interactions among thermal, mechanical, and metallurgical phenomena. On the other hand, there is a rich body of process modeling literature for processes similar to powder bed AM, to some extent, such as electron beam welding (EBW) (Hemmer and Grong, 1999; Rouquette *et al.*, 2007; Liu *et al.*, 2010; Luo *et al.*, 2010; Lacki and Adamus, 2011), laser deposition or melting (Wang *et al.*, 2008; Roberts *et al.*, 2009), and laser welding (LW) (Lankalapalli *et al.*, 1996; Tsirkas *et al.*, 2003), etc. In EBW and LW, because of the resultant keyhole phenomenon from an incident electron or laser beam, the heat source is generally modeled as a conical volumetric body heat flux right beneath the top workpiece surface (Lankalapalli *et al.*, 1996; Tsirkas *et al.*, 2003; Wang *et al.*, 2008; Liu *et al.*, 2010; Luo *et al.*, 2010; Zäh and

Lutzmann, 2010; Lacki and Adamus, 2011). The heat intensity is assumed with a Gaussian distribution horizontally and with a linear (or quadratic) decay along the penetration depth (Lankalapalli *et al.*, 1996; Tsirkas *et al.*, 2003; Rouquette *et al.*, 2007; Wang *et al.*, 2008; Liu *et al.*, 2010; Lacki and Adamus, 2011). Lankalapalli *et al.* (Lankalapalli *et al.*, 1996) derived a closed-form solution of temperature distribution with the assumption of two-dimensional (2D) heat conduction and a conical keyhole, while the penetration depth was numerically predicted as a three-dimensional (3D) condition. The mathematical-physical model presented by Lankalapalli *et al.* was widely used in EBW (Rouquette *et al.*, 2007; Liu *et al.*, 2010; Luo *et al.*, 2010; Lacki and Adamus, 2011), laser deposition (Wang *et al.*, 2008) and LW (Tsirkas *et al.*, 2003). The state of the art in this field includes the simulation with the Level-Set Method from such as Qi and Mazumder (Qi, Huan *et al.*, 2006), Wen and Shin (Wen and Shin, 2010) or the Volume-of-Fluid Method such as Choi *et al.* (Choi *et al.*, 2005). These two methods are able to capture the convection in a molten pool and even the free-surface boundary. However, due to substantially high computational costs and limited commercial code access, finite element (FE) modeling is still one of the most efficient ways to simulate the EBAM process. To incorporate the effect of heat convection (of a molten pool) in FE thermal models, Taylor *et al.* (Taylor *et al.*, 2002), De and DebRoy (De and Debroy, 2007) used an effective thermal conductivity, a large value compared to a solid, of the liquid metal in a molten pool, which was proved to be of a reasonable approach.

On the other hand, the application of metallic powder and powder-bed distinguishes EBAM or SLM from EBW. Especially for EBAM process, a layer of metal powder is distributed by a rake, followed by preheating for powder light-sintering, which is considered

as the initial state for the major process stage in each layer deposition, e.g., melting. It is well known that thermal properties of metallic powder are significantly different from those of the corresponding solid bulk material (Lin *et al.*, 1985; Sih and Barlow, 2004). In addition, since sintering takes place in the powder-bed during preheating, usually about 700 to 800 °C for Ti-6Al-4V, before the melting stage, the degree of sintering will affect the powder properties, which should be considered as well for comprehensive thermal modeling. Sih and Barlow (Sih and Barlow, 2004) developed a porosity-dependent model to predict the emissivity for different material conditions and environments. A few porosity-dependent model of the thermal conductivity of metal powder have been developed for selective laser melting (SLM) in a gas surrounding (Kolossof *et al.*, 2004; Patil and Yadava, 2007; Roberts *et al.*, 2009), which is different from EBAM, vacuum instead. Tolochko *et al.* (Tolochko *et al.*, 2003) investigated the mechanisms of selective laser sintering (SLS) and heat transfer in Ti powder. A model was derived to predict the effective thermal conductivity of Ti powder-bed in a vacuum. All of the aforementioned studies considered that metallic powder materials have the same specific heat and latent heat of fusion as the solid bulk materials.

For EBAM process simulations, Mahale (Mahale, 2009) applied both a finite element method and a finite difference method to develop a 3D model by defining the scan path into COMSOL Multiphysics using Matlab for simulation of the EBAM process of Al 7075. On the other hand, Zäh and Lutzmann (Zäh and Lutzmann, 2010) conducted a thermal analysis of EBAM with FE analysis, taking account of the metallic powder properties in the powder layer. Based on adequate parameters simulations and corresponding experiment study, a process window that prevents from melt ball formations and delaminations can be decided.

Jamshidinia et al. (Jamshidinia *et al.*, 2013a) recently developed a thermal-fluid flow model of EBAM incorporating powder thermal properties to study the influence of process parameters. The effects of the flow convection in temperature distributions and molten pool geometry were investigated. The authors indicated that ignoring heat convection inside the melt pool would form a melt pool narrower and shorter, but of a deeper penetration and higher maximum temperatures.

2.2 Process Parameters Study for Electron and Laser Melting Process

Because metal AM processes are typically operated at a very high energy-density and a fast moving speed, temperatures, temperature gradients and heating and cooling rates can be extremely high, localized and rapid. Therefore, the process itself is very sensitive to process parameters among other factors. It is, therefore, necessary to investigate and establish the relationship between powder bed AM process parameters and process characteristics such as melt pool sizes. Mahamood et al. (Mahamood *et al.*, 2013) studied the effect of laser power density on the evolving properties of laser metal deposited titanium alloy. The results show that the higher the laser power density employed, the smoother the obtained surface. The microhardness initially increased as the laser power density was increased and then decreased as the power density was further increased. Further, Zhao et al. (Zhao *et al.*, 2013) recently investigated the effects of interpass idle time on thermal stresses in multipass multilayer weld-based rapid prototyping using numerical simulations and experiments. The authors reported that the residual stresses of deposition workpiece decrease with the increase of interpass idle time, whereas the interpass and interlayer stresses on the central line of substrate increase with the increase of interpass idle time.

There are only a few reports about EBAM process parameter effects in literature. Zäh and Lutzmann (Zäh and Lutzmann, 2010) and Zäh and Kahnert (Zäh and Kahnert, 2009) utilized the developed thermal model to investigate various combinations of the process parameters such as the beam scan speed and the beam power to determine the shape of resultant melt pools, which are related to final part microstructures. Based on adequate parameters simulation and corresponding experiment study, a process window that exhibit the absence of melt ball formation and delamination can be decided. Jamshidinia et al. (Jamshidinia *et al.*, 2013a) developed a thermal-fluid model for the EBAM process incorporating the powder thermal properties to study the influence of process parameters. The simulation results show that under given conditions, higher beam current results in a larger molten pool size and a faster scanning can result in a decrease in the molten pool width as well as an increase of the length. Gong et al. (Gong *et al.*, 2013) experimentally studied process parameters effects on defects in Ti-6Al-4V parts fabricated by an EBAM machine. Four process parameters: the beam current, the beam focus offset, the beam line offset and the beam speed, were varied to study the part surface porosity. Generally, from their experiments part porosity increased with increasing beam line offset and scanning speed, while porosity decreased with increasing beam current. The focus offset value did not significantly change the porosity until 16 mA, after that porosity increased with continuous increase of focus offset under given conditions. Hrabe and Quinn (Hrabe and Quinn, 2013) researched the effects that part size and distance from the build plate had on the microstructure and mechanical properties of EBAM manufactured Ti-6Al-4V parts. They found that distance from the build plate had no influence on part properties, however the part

size was found to have a small effect on the ultimate tensile strength and yield strength of the parts.

Process parameter effects on melt pool geometry have also been studied for part quality control in metal AM. In a wire-fed electron beam freeform fabrication process, Soylemez and Beuth (Soylemez *et al.*, 2010) established a process map for constant melt pool cross-sectional areas and constant length/depth ratios over a range of the electron beam power and the beam velocity. Such a process map may ensure engineers to choose a beam power and a travel speed for user-specified values of a deposition rate, a melt pool cross sectional area and a melt pool length-depth ratio.

On the other hand, there are relatively more studies of process parameter effects in laser-based metal AM reported in the literature. Experimental methods to study process parameters effects in selective laser sintering (SLS) have been reported by many researchers. Miller *et al.* (Miller *et al.*, 1997) applied a factorial approach to investigate the build sample strength as a function of individual parameters, e.g., the scanning speed, the laser power and the hatch spacing, as well as parameter interactions. The beam spot size was also considered in the developed mathematical model to improve the accuracy. Song and Koenig (Song and Koenig, 1997) examined the influence of the laser beam power, the scanning speed and the hatch spacing to the part quality characteristics such as the surface roughness, the density and the bonding between layers and curl on a bronze powder. The authors indicated that the surface roughness of build samples decreases with a decrease of the hatch spacing and the scanning speed. In addition, the density increases with a higher energy density as a mean of reducing the hatch spacing or the scanning speed. Simchi and Pohl (Simchi and Pohl, 2003)

also experimentally studied the effects of process parameters on the part density, the surface morphology as well as the microstructure in a laser sintering process. The authors found that intensifying the laser energy input could lead to a higher densification and smoother surfaces. Moreover, increasing the energy input over $0.8 \text{ kJ}\cdot\text{mm}^{-3}$ led to the formation of horizontally elongated pores while the sintered density remained almost constant. Chatterjee et al. (Chatterjee *et al.*, 2003) reported that the build sample hardness increased with a decrease of the layer thickness while the laser hatching space on hardness was considered relatively insignificant. In addition, increasing the layer thickness and hatching space could result in increased porosity.

For selective laser melting (SLM), Yadroitsev et al. (Yadroitsev *et al.*, 2007) carried out a parametric study using Inco 904L powder, and determined the optimal parameters of the powder layer thickness and the power input per unit speed as 0.05 mm thickness and power/speed as 270~420 W·s/m. It was also indicated that the greater the value of the power/speed ratio is, the larger the remelted scanning line is. Further, Meier and Haberland (Meier and Haberland, 2008) experimentally demonstrated that the part porosity decrease with increasing the laser power; the authors also showed that a high scanning speed must be accompanied with a high power and a short hatch distances to obtain a dense nonporous part. In a laser metal deposition shaping (LMDS) study, Zhang et al. (Zhang *et al.*, 2007) conducted multiple experiments using a nickel-based super alloy to systematically investigate the process parameters effect, such as the laser power, the spot diameter and the scanning velocity on the build part characteristics. The study showed fully dense and near-net-shaped metallic parts can be directly obtained through optimal process parameters by melting

coaxially fed powder with a laser.

Wang and Felicelli (Wang and Felicelli, 2007) developed a 3D finite element model to predict the temperature distribution and phase transformation in the Laser Engineered Net Shaping (LENS) process using stainless steel 410 powder. The process parameters effects were studied using the model. The simulation results showed that a higher scanning speed could reduce the proportion of tempered martensite, and thus, a more uniform microstructure as well as hardness distributions were expected. In another LENS process study, Neela and De (Neela and De, 2009) presented a 3D finite element thermal model to study the influence of the laser power, the scanning velocity, the powder flow rate, and the idle time between layer depositions on the thermal circles. The authors concluded that the final properties and dimensional accuracy of the deposited layers would be greatly influenced by the mutual effects of these parameters.

In a laser-based sintering study, Patil and Yadava (Patil and Yadava, 2007) developed a transient finite element (FE)-based thermal model to calculate temperature distributions within a single metallic layer. The effect of process parameters such as the laser power and the beam diameter on temperature distribution was studied on titanium material. The simulation results indicated that the temperature on the top surface would increase with an increase of laser power. In addition, an increase of the beam diameter would also increase surface temperature, but beyond 0.1 mm beam diameter, the temperature decreased if continuously increasing the beam diameter under given conditions. Dong et al. (Dong *et al.*, 2009) developed a thermal model incorporating temperature-dependent material properties while no phase change effect considered. Based on the simulations, the authors noted that

powder-bed surface maximum temperatures decreased along with the increase of the beam speed. The authors also found that increasing the laser spot diameter could reduce the surface temperature due to the decrease of the laser beam power intensity. In another laser-based metal AM study, Kumar and Roy (Kumar and Roy, 2009) developed a numerical heat transfer model incorporating Marangoni–Rayleigh–Benard convection to investigate the influence of input parameters to the melt pool dimensions and melt pool average temperature. The authors showed that a higher scanning speed would cause decrease in the melt size, the rate of cooling by the surrounding cold substrate increased and the microstructure becomes finer. It was also shown that the maximum and average melt pool temperatures decreased with the increase of the scanning speed.

2.3 Thermomechanical Modeling of Powder Bed AM

2.3.1 General Metal AM Numerical Study

The laser based metal additive manufacturing studies have been reviewed first since there are relatively more studies of experimental and finite element (FE) modelling works in this field. In a multi-Layer laser Direct Metal Deposition (DMD) process, Liu et al. (Liu et al., 2013) have presented a 3D sequentially coupled thermo-mechanical FE model to predict residual stresses and deformations. The temperature, residual stress and deflections have been explored. Based on simulation, the cooling rate in DMD process can be as high as 3000 K/s. In addition, stress distribution along x, y, z direction has been investigated. The model prediction ability has been verified by experiment value. Kamara et al. (Kamara *et al.*, 2011) investigated the residual stress generated from the deposition of multiple-layer wall of Waspaloy structure on Inconel 718 substrate in a laser DMD process. The residual stress

characteristic in Waspaloy wall that was built from the deposition of 20 layers with each consisting of 6 parallel tracks has been studied using ANSYS. The FE simulation results revealed that the stress along the length of the wall oscillated about a stress-free state while the stress was found to vary with position along the height of the wall. What is more, the wall was near stress-free close to the substrate. The tensile stress in scanning direction of the deposited wall increased with number of layers, on the contrary, the stress in the building direction of the wall was close to zero. The predicted results were validated by comparing with published experimental data. Of a Wire and Arc Additive Layer Manufacturing (WAALM) study, Ding et al. (Ding *et al.*, 2011) utilized FE method to study the thermomechanical performance of large multi-layer wall shaped WAALM structures. Simulation results about temperature distribution, stress distribution and distortions were verified by experiments. The simulation study also indicated that both of the developed steady state and transient model could predict the heating and cooling cycles during the WAALM process. Stress across the deposit was uniform with very little influence of succeeding layers. In addition, Clamping and unclamping significantly affected the stress redistribution. In a Selective Laser Melting (SLM) process, Zaeh and Branner (Zaeh and Branner, 2010) studied the effect of layer thickness on t-shaped cantilever part deformation using a 3D FE thermomechanical model. The simulation indicated that smaller layer thickness sizes were responsible for larger deformations due to inserted energy had to be distributed into reduced layer volumes. Dai and Shaw (Dai and Shaw, 2002) numerically investigated the effect of laser scanning strategy on residual thermal stresses and distortion of a flat nickel plate in ANSYS, the findings revealed that proper laser scanning patterns could

result in less out-of-plane distortion. Nickel et al. (Nickel *et al.*, 2001) presented a 3D FE study on deposition pattern of laser deposited metal parts produced by the shape deposition manufacturing (SDM). The results clearly pointed out that the deposition pattern had a significant effect on part deflection. Specifically, for a plate geometry, a raster pattern with lines oriented 90 degree from the beam's long axis produced the lowest deflections for a beam substrate, while the spiral pattern scanned from the outside to the inside produced low and uniform deflections. Matsumoto et al (Matsumoto *et al.*, 2002) has proposed a FE method for calculating the distribution of temperature and stress within a single metallic layer formed on the powder-bed in SLM process. FE study showed the stress distribution in the solidified part caused by the temperature change during forming showed a stripe pattern of compressive and tensile stresses. The amount of the deflection of the solid layer increased as the track length increased. In addition, when the neighboring track began to solidify, a large tensile stress between the solidified tracks appeared at the side end of the solid part, which might cause the cracking of the layer. They suggested that to prevent part deficiency, it was better to divide the area into small segments with strong frames and short track scanning in each segment.

2.3.2 Powder-bed EBAM Thermomechanical Study

However, there are limited literature on the study of thermo-mechanical process of EBAM, Jamshidinia et al. (Jamshidinia *et al.*, 2013b) developed a coupled Computational Fluid Dynamic (CFD) - Finite Element Method (FEM) model to study the heat and thermal stress distribution in electron beam melting process. Their simulation results showed that the formation of an outward flow in the molten pool of Ti-6Al-4V could be caused by negative temperature coefficient of surface tension. Their study also indicated that electron beam

scanning speed would have influence on the thermal stresses, specifically, the minimum electron beam scanning speed of 100 mm/s resulted in the maximum thermal stress in melting step and minimum thermal stresses in cooling stress.

References

- Chatterjee, A., Kumar, S., Saha, P., Mishra, P., & Choudhury, A. R. (2003). An experimental design approach to selective laser sintering of low carbon steel. *Journal of Materials Processing Technology*, 136(1), 151-157.
- Choi, J., Han, L., & Hua, Y. (2005). Modeling and experiments of laser cladding with droplet injection. *Journal of Heat Transfer*, 127(9), 978-986.
- Dai, K., & Shaw, L. (2002). Distortion minimization of laser-processed components through control of laser scanning patterns. *Rapid Prototyping Journal*, 8(5), 270-276.
- De, A., & DebRoy, T. (2007). Improving reliability of heat and fluid flow calculation during conduction mode laser spot welding by multivariable optimisation. *Science and Technology of Welding and Joining*, 11, 143-153.
- Ding, J., Colegrove, P., Mehnen, J., Ganguly, S., Sequeira Almeida, P., Wang, F., & Williams, S. (2011). Thermo-mechanical analysis of Wire and Arc Additive Layer Manufacturing process on large multi-layer parts. *Computational Materials Science*, 50(12), 3315-3322.
- Dong, L., Makradi, A., Ahzi, S., & Remond, Y. (2009). Three-dimensional transient finite element analysis of the selective laser sintering process. *Journal of materials processing technology*, 209(2), 700-706.
- Gong, H., Rafi, K., Starr, T., & Stucker, B. (2013). The effects of processing parameters on defect regularity in ti-6al-4v parts fabricated by selective laser melting and electron beam melting. 24th Annual International Solid Freeform Fabrication Symposium - An Additive Manufacturing Conference, Austin, TX, USA, August 12-14, 2013.
- Hemmer, H., & Grong, Ø. (1999). Prediction of penetration depths during electron beam welding. *Science and Technology of Welding & Joining*, 4(4), 219-225.
- Hrabe, N., & Quinn, T. (2013). Effects of processing on microstructure and mechanical properties of a titanium alloy (Ti-6Al-4V) fabricated using electron beam melting (EBM), part 1: Distance from build plate and part size. *Materials Science and Engineering: A*, 573, 264-270.

- Jamshidinia, M., Kong, F., & Kovacevic, R. (2013a). Numerical modeling of heat distribution in the electron beam melting® of Ti-6Al-4V. *Journal of Manufacturing Science and Engineering*, 135(6), 061010.
- Jamshidinia, M., Kong, F., & Kovacevic, R. (2013b). The coupled CFD-FEM model of Electron Beam Melting® (EBM). *Mechanical Engineering Research*, Paper 4.
- Kamara, A., Marimuthu, S., & Li, L. (2011). A numerical investigation into residual stress characteristics in laser deposited multiple layer waspaloy parts. *Journal of Manufacturing Science and Engineering*, 133(3), 031013.
- Kolossov, S., Boillat, E., Glardon, R., Fischer, P., & Locher, M. (2004). 3D FE simulation for temperature evolution in the selective laser sintering process. *International Journal of Machine Tools and Manufacture*, 44(2-3), 117-123.
- Kumar, A., & Roy, S. (2009). Effect of three-dimensional melt pool convection on process characteristics during laser cladding. *Computational Materials Science*, 46(2), 495-506.
- Lacki, P., & Adamus, K. (2011). Numerical simulation of the electron beam welding process. *Computers & Structures*, 89(11-12), 977-985.
- Lankalapalli, K., Tu, J. F., & Gartner, M. (1996). A model for estimating penetration depth of laser welding processes. *Journal of Physics D: Applied Physics*, 29, 1831.
- Lin, T. H., Watson, J. S., & Fisher, P. W. (1985). Thermal conductivity of iron-titanium powders. *Journal of Chemical & Engineering Data*, 30(4), 369-372.
- Liu, C., Wu, B., & Zhang, J. (2010). Numerical Investigation of Residual Stress in Thick Titanium Alloy Plate Joined with Electron Beam Welding. *Metallurgical and Materials Transactions B*, 41(5), 1129-1138.
- Liu, H., Sparks, T. E., Liou, F. W., & Dietrich, D. M. (2013). Numerical analysis of thermal stress and deformation in multi-layer laser metal deposition processes. 24th Annual International Solid Freeform Fabrication Symposium - An Additive Manufacturing Conference, , Austin, TX, USA, August 12-14, 2013.
- Luo, Y., Liu, J., & Ye, H. (2010). An analytical model and tomographic calculation of vacuum electron beam welding heat source. *Vacuum*, 84(6), 857-863.
- Mahale, T. R. (2009). Electron beam melting of advanced materials and structures. Ph.D. thesis, North Carolina State University, Raleigh, NC.
- Mahamood, R. M., Akinlabi, E. T., Shukla, M., & Pityana, S. (2013). Characterizing the

effect of laser power density on microstructure, microhardness, and surface finish of laser deposited titanium alloy. *Journal of Manufacturing Science and Engineering*, 135(6), 064502.

Matsumoto, M., Shiomi, M., Osakada, K., & Abe, F. (2002). Finite element analysis of single layer forming on metallic powder bed in rapid prototyping by selective laser processing. *International Journal of Machine Tools and Manufacture*, 42(1), 61-67.

Meier, H., & Haberland, C. (2008). Experimental studies on selective laser melting of metallic parts. *Materialwissenschaft und Werkstofftechnik*, 39(9), 665-670.

Miller, D., Deckard, C., & Williams, J. (1997). Variable beam size SLS workstation and enhanced SLS model. *Rapid Prototyping Journal*, 3(1), 4-11.

Neela, V., & De, A. (2009). Three-dimensional heat transfer analysis of LENSTM process using finite element method. *The International Journal of Advanced Manufacturing Technology*, 45(9-10), 935-943.

Nickel, A., Barnett, D., & Prinz, F. (2001). Thermal stresses and deposition patterns in layered manufacturing. *Materials Science and Engineering: A*, 317(1), 59-64.

Patil, R. B., & Yadava, V. (2007). Finite element analysis of temperature distribution in single metallic powder layer during metal laser sintering. *International Journal of Machine Tools and Manufacture*, 47(7-8), 1069-1080.

Qi, H., Mazumder, J., & Ki, H. (2006). Numerical simulation of heat transfer and fluid flow in coaxial laser cladding process for direct metal deposition. *Journal of Applied Physics*, 100(2), 024903.

Roberts, I. A., Wang, C. J., Esterlein, R., Stanford, M., & Mynors, D. J. (2009). A three-dimensional finite element analysis of the temperature field during laser melting of metal powders in additive layer manufacturing. *International Journal of Machine Tools and Manufacture*, 49(12-13), 916-923.

Rouquette, S., Guo, J., & Le Masson, P. (2007). Estimation of the parameters of a Gaussian heat source by the Levenberg-Marquardt method: Application to the electron beam welding. *International Journal of Thermal Sciences*, 46(2), 128-138.

Sih, S. S., & Barlow, J. W. (2004). The prediction of the emissivity and thermal conductivity of powder beds. *Particulate Science and Technology*, 22, 291-304.

Simchi, A., & Pohl, H. (2003). Effects of laser sintering processing parameters on the microstructure and densification of iron powder. *Materials Science and Engineering: A*, 359(1), 119-128.

- Song, Y.-A., & Koenig, W. (1997). Experimental study of the basic process mechanism for direct selective laser sintering of low-melting metallic powder. *CIRP Annals-Manufacturing Technology*, 46(1), 127-130.
- Soylemez, E., Beuth, J. L., & Taminger, K. (2010). Controlling melt pool dimensions over a wide range of material deposition rates in electron beam additive manufacturing. 21st Annual International Solid Freeform Fabrication Symposium - An Additive Manufacturing Conference, Austin, TX, August 9-11, 2010, pp. 571-582.
- Taylor, G. A., Hughes, M., Strusevich, N., & Pericleous, K. (2002). Finite volume methods applied to the computational modelling of welding phenomena. *Applied Mathematical Modelling*, 26(2), 311-322.
- Tolochko, N. K., Arshinov, M. K., Gusarov, A. V., Titov, V. I., Laoui, T., & Froyen, L. (2003). Mechanisms of selective laser sintering and heat transfer in Ti powder. *Rapid Prototyping Journal*, 9, 314-326.
- Tsirkas, S. A., Papanikos, P., & Kermanidis, T. (2003). Numerical simulation of the laser welding process in butt-joint specimens. *Journal of Materials Processing Technology*, 134(1), 59-69.
- Wang, L., & Felicelli, S. (2007). Process modeling in laser deposition of multilayer SS410 steel. *Journal of Manufacturing Science and Engineering*, 129(6), 1028-1034.
- Wang, L., Felicelli, S., Gooroochurn, Y., Wang, P. T., & Horstemeyer, M. F. (2008). Optimization of the LENS process for steady molten pool size. *Materials Science & Engineering A (Structural Materials: Properties, Microstructure and Processing)*, 474, 148-156.
- Wen, S., & Shin, Y. C. (2010). Modeling of transport phenomena during the coaxial laser direct deposition process. *Journal of Applied Physics*, 108(4), 044908.
- Yadroitsev, I., Bertrand, P., & Smurov, I. (2007). Parametric analysis of the selective laser melting process. *Applied surface science*, 253(19), 8064-8069.
- Zhang, K., Liu, W., & Shang, X. (2007). Research on the processing experiments of laser metal deposition shaping. *Optics & Laser Technology*, 39(3), 549-557.
- Zhao, H., Zhang, G., Yin, Z., & Wu, L. (2013). Effects of Interpass Idle Time on Thermal Stresses in Multipass Multilayer Weld-Based Rapid Prototyping. *Journal of Manufacturing Science and Engineering*, 135(1), 011016.
- Zäh, M. F., & Branner, G. (2010). Investigations on residual stresses and deformations in

selective laser melting. *Production Engineering*, 4(1), 35-45.

Zäh, M. F., & Kahnert, M. (2009). The effect of scanning strategies on electron beam sintering. *Production Engineering*, 3(3), 217-224.

Zäh, M. F., & Lutzmann, S. (2010). Modelling and simulation of electron beam melting. *Production Engineering. Research and Development*, 4, 15-23.

CHAPTER 3

ON PROCESS TEMPERATURE IN POWDER-BED ELECTRON BEAM ADDITIVE MANUFACTURING: MODEL DEVELOPMENT AND VALIDATION

Abstract

Powder-bed beam-based metal additive manufacturing (AM) such as electron beam additive manufacturing (EBAM) has a potential to offer innovative solutions to many challenges and difficulties faced in the manufacturing industry. However, the complex process physics of EBAM has not been fully understood, hindering part quality consistency, efficient process development and process optimizations, etc., for effective EBAM usage. In this study, numerical approach is used to research the process temperatures and other thermal characteristics in EBAM using Ti-6Al-4V powder. The objective of this study was to develop a comprehensive thermal model, using a finite element method, to predict temperature distributions and history in the EBAM process. Experimental results were employed to validate the developed model.

The major results are summarized as follows. The thermal conductivity of Ti-6Al-4V powder is one of critical factors for temperature predictions. At a beam speed of about 680 mm/s, a beam current of about 7.0 mA and a diameter of 0.55 mm, the peak process temperature is on the order around 2700 °C, and the melt pools have dimensions of about 2.94 mm, 1.09 mm and 0.12 mm, in length, width and depth, respectively. In general, the simulations are in reasonable agreement with the experimental results with an average error of 32 % for the melt pool sizes. From the simulations, the powder porosity is found critical to

the thermal characteristics in EBAM. Increasing the powder porosity will increase the melt pool size. On the other hand, increasing the porosity will elevate the peak process temperature.

3.1 Introduction

With recent swift advances, additive manufacturing (AM) has witnessed itself fiercely reshaping the future of the manufacturing industry across virtually every sector. Metal AM such as powder-bed fusion and directed energy deposition processes has emerged as cost-effective alternatives to potential main-stream manufacturing processes. In addition, metal AM has sparked numerous ideas for design and manufacturing innovations that turn impossible-to-make to design freedom, and turn inefficient productions into sustainable supply chains. The powder-bed electron beam additive manufacturing (EBAM) process, using an electron beam to melt and fuse metal powder, is one of a few AM technologies capable of making full-density functional metallic parts, especially suitable for complex-shaped components, e.g., near-net-shape parts for medical implants and internal cavities and channels, which are difficult to make by conventional manufacturing means (Arcam website, 2013; Gong *et al.*, 2012; Biamino *et al.*, 2011).

The major process steps of EBAM include distributing powder layers, powder preheating, and selectively powder melting, etc. In preheating, the system utilizes a high-energy focused electron beam to raster-scan at a high speed, e.g., 15 m/sec, and at a high beam current (~30 mA) to lightly sinter the top powder layer, which may help to reduce residual stress. The process is followed by melting, contour-melting and hatch-melting, in a selective area, driven by three-dimensional (3D) CAD data. After the completion of one layer

building, another layer of powder will be distributed, preheated, and selectively melted, with such a cycle repeated. The build process occurs in a chamber with a nominal vacuum of 10⁻⁴ torr (Gaytan *et al.*, 2009). The general procedures for EBAM of metal components can be found from an animation made available by the Oak Ridge National Laboratory (ORNL) (ORNL youtube, 2014). Compared to laser-based powder-bed metal AM, EBAM is able to achieve a deeper energy penetration, a higher energy absorption rate, a higher power, and a higher scan rate, all translated to a higher production rate. In addition, EBAM parts have a lower impurity and porosity and lower residual stresses compared to laser-based counterparts. However, EBAM parts generally exhibit poor surface finish and poor dimensional accuracy. Because of the vacuum needed and associated x-ray emission, EBAM is also less accessible to the build chamber for process monitoring.

EBAM has been increasingly investigated for producing parts from a wide range of applications, from turbine blades to acetabular cup hip replacements, using commercial powder made of different metals and alloys. Ti-6Al-4V is one of the first and most widely used materials in EBAM, because Ti alloys have superior mechanical properties and biocompatibility, and because fabrications of Ti alloys by conventional manufacturing are difficult due to a high melting point and chemical affinity (Heinl *et al.*, 2007). In general, mechanical properties of EBAM parts are comparable to or even better than parts made by conventional processes. Moreover, because of a high energy source as well as a vacuum working environment, EBAM has also been attempted using other metal-based powder including tool steels (Cormier *et al.*, 2004), copper (Ramirez *et al.*, 2011), nickel-based superalloys (Murr *et al.*, 2011), and intermetallic, etc.

Commercialization of the EBAM technology has been successful; however, despite of many potential advantages over conventional manufacturing technologies, EBAM still encounters several part and process defects such as melt ball formations, porosity, and layer delaminations (Zäh and Lutzmann, 2010), and yet, the mechanism related to those defects, due to process conditions, have not been fully understood. Predictable physics-based modeling of EBAM process phenomena are required to investigate process characteristics such as melt pool sizes and shapes and temperature fields, etc. It is also desired to facilitate process simulations in order to determine appropriate ranges of process parameters that are potentially correlated to the avoidance of part defects.

To achieve better and cost-effective EBAM usage for widespread applications, fundamental understanding of the EBAM process physics, especially its thermal characteristics, is required. There is an increasing need to bridge the gap between EBAM applications and process modeling and simulations. However, only few studies of EBAM process modeling exist in literature and several critical factors have not been properly addressed. Moreover, process temperatures measurements in EBAM for model validations have not been widely available.

The objective of this research is to develop a comprehensive thermal model for the EBAM process temperature predictions and further validated by experimental temperature measurements. A 3D thermal model for EBAM was developed using FE software, ABAQUS, incorporating volumetric Gaussian distribution heat source, porosity-dependent thermal properties. Temperature measurements during EBAM fabrications using an NIR thermal imager were attempted for model validations. The model was also applied to investigate the

powder porosity effect on temperature profiles and melt pool sizes in EBAM.

3.2 Modeling and Simulation

3.2.1 Thermal Modeling

The governing equation of heat transport in the EBAM process, with the assumption of negligible convection flow, is:

$$\nabla \left(\frac{k_{(T)}}{\rho_{(T)}c_{(T)}} \nabla T \right) + \frac{\dot{Q}_{(x,y,z,T)}}{\rho_{(T)}c_{(T)}} = \frac{\partial T}{\partial t} + v_s \frac{\partial T}{\partial x}, \quad (1)$$

where T is temperature, $\dot{Q}_{(x,y,z)}$ is the absorbed heat flux, c is specific heat capacity, ρ is density, k is thermal conductivity, v_s is the speed, assumed constant, of the moving electron beam heat source in the x direction.

The latent heat of fusion, L_f , was considered in this model to trace the solid-liquid interface of the molten pool. When the temperature drops to between the solidus and liquidus points, T_S and T_L , respectively, the latent heat of fusion was modeled as an additional term of the internal thermal energy per unit mass, dU . Hence, the enthalpy is defined as:

$$H(T) = \int cdT + L_f f, \quad (2)$$

where f is the volumetric fraction of the liquid, which is defined as:

$$f = \begin{cases} 0 & T < T_S, \\ \frac{T - T_S}{T_L - T_S} & T_S \leq T \leq T_L, \\ 1 & T > T_L \end{cases} \quad (3)$$

To simulate the heat input distribution in EBAM, the electron beam energy is modeled as a conical moving heat source with a Gaussian distribution, with the intensity varies along the depth. In this study, the energy input was modeled as Eqn. (4), which is modified from

Zäh and Lutzmann (Zäh and Lutzmann, 2010); the heat intensity decreases with the increase of the penetration depth (Zäh and Lutzmann, 2010),

$$\dot{Q}_{(x,y,z)} = \eta \times \frac{H_s \times I_z}{S} \quad (4)$$

with

$$I_z = \frac{1}{0.75} \left(-2.25 \left(\frac{z}{S} \right)^2 + 1.5 \left(\frac{z}{S} \right) + 0.75 \right),$$

$$H_s = \frac{2U_o I_b}{\pi \Phi_E^2} \exp \left\{ -\frac{2[(x-x_s)^2 + (y-y_s)^2]}{\Phi_E^2} \right\}.$$

in which the parameters include electron beam efficiency coefficient: η (including efficiency values for the beam control and energy conversion at the part surface), voltage: U_o , current: I_b , penetration depth: S , and beam diameter: Φ_E . While x_s and y_s are the instantaneous horizontal position of the heat source (electron beam) center. Thus, the 3D heat source can be determined, combining the Gaussian heat source H_s (Cline and Anthony, 1977) and the penetration function I_z .

To implement the volumetric heat source in the FE model, a user subroutine of DFLUX was developed in FORTRAN. The subroutine was to be called at the beginning of each iteration. Then, it reads the simulation time to determine the location of the heat source center, so that the domain of the volumetric heat flux can be determined. The magnitude of the heat flux assigned at each nodule is then interpolated using Eqn. (4).

As mentioned earlier, the EBAM process is conducted in vacuum (Heinl *et al.*, 2007), convection between the powder-bed surface and the environment can be ignored. Hence, only radiation was considered for the thermal boundary condition between the powder or part

surfaces and the surrounding. On the other hand, the solid substrate and powder layer were assigned with a uniform temperature distribution, resulted from preheating, T_{preheat} , as the initial thermal condition. Further, the temperature of the solid substrate bottom was assigned with a constant temperature of T_{preheat} as the thermal boundary condition.

The material considered in this study was Ti-6Al-4V powder. Because a wide range of temperatures can be expected in EBAM of Ti-6Al-4V, temperature-dependent material properties were needed and incorporated in this study. Temperature dependent properties of solid Ti-6Al-4V alloy have been reported: density (Rai, 2008; Yang *et al.*, 2010), specific heat (Mills, 2002), and thermal conductivity (Yang *et al.*, 2010). The results are summarized in Figure 3.1, and were utilized in the thermal model, except the thermal conductivity, which was measured (discussed below). On the other hand, to account for heat convection in the molten pool during melting, an effective thermal conductivity above the melting point was used, according to Liu *et al.* (Liu *et al.*, 2010).

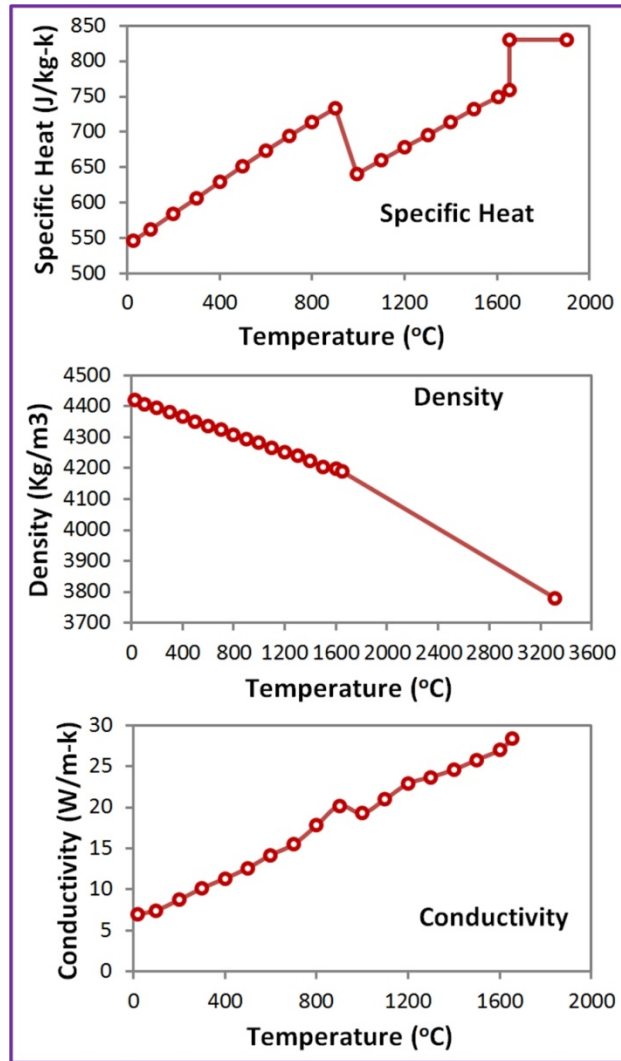


Figure 3.1. Temperature dependent specific heat, density and thermal conductivity of Ti-6Al-4V (Mills, 2002; Rai, 2008; Yang *et al.*, 2010).

As indicated earlier, thermal properties of metallic powder are considerably different from those of the solid material. Several studies have been conducted for the emissivity and thermal conductivity of metallic powder. Sih and Barlow (Sih and Barlow, 2004) developed a porosity-dependent emissivity model for a metallic powder-bed, which considered the emissivity of the solid bulk material, the emissivity of the gap between adjacent powder particles, the area fraction of the surface that is occupied by the radiation emitting holes, and the porosity of the powder-bed. The emissivity of Ti-6Al-4V used in the model was estimated from literature; Yang *et al.* experimentally estimated the emissivity of Ti-6Al-4V as 0.7 (Yang

et al., 2010). Due to the very localized high temperature zone (order of mm) and a high temperature in the build chamber, it was found the radiation was insignificant, also insensitive to the emissivity value.

There have also been some studies of the thermal conductivity of powder, considering conductance between particles through the necks formed from sintering. However, most models for metallic powder include heat conduction of the gas void in the pore, different from the condition in EBAM due to the vacuum in the chamber (Heinl *et al.*, 2007). Tolochko *et al.* (Tolochko *et al.*, 2003) developed a thermal conductivity model for Ti powder in a study of SLS. The model considered the effective thermal conductivity due to radiation and effective thermal conductance due to heat conduction through powder necks, which is related to the powder diameter and packing, related to the porosity. On the other hand, many researchers indicated that the specific heat and latent heat of fusion of powders can be considered the same as those of the solid material (Lin *et al.*, 1985; Tolochko *et al.*, 2003; Kolossov *et al.*, 2004; Sih and Barlow, 2004; Patil and Yadava, 2007; Roberts *et al.*, 2009; Zäh and Lutzmann, 2010).

During preheating in EBAM, a certain portion of sintered powder is expected, which clearly shows inter-particle necks and may affect the thermal conductivity of the powder. The thermal conductivity of Ti-6Al-4V powder preserved in the powder-bed condition from EBAM has been experimentally measured (Gong *et al.*, 2013a). With the experimental data of thermal conductivities, linear interpolation method was then applied for both the solid and powder thermal conductivity values at different temperatures, and the phase change range between 900 °C and 995 °C, was considered as well (Yang *et al.*, 2010). Figure 3.2 shows the

interpolated thermal conductivity for both solid and powder Ti-6Al-4V.

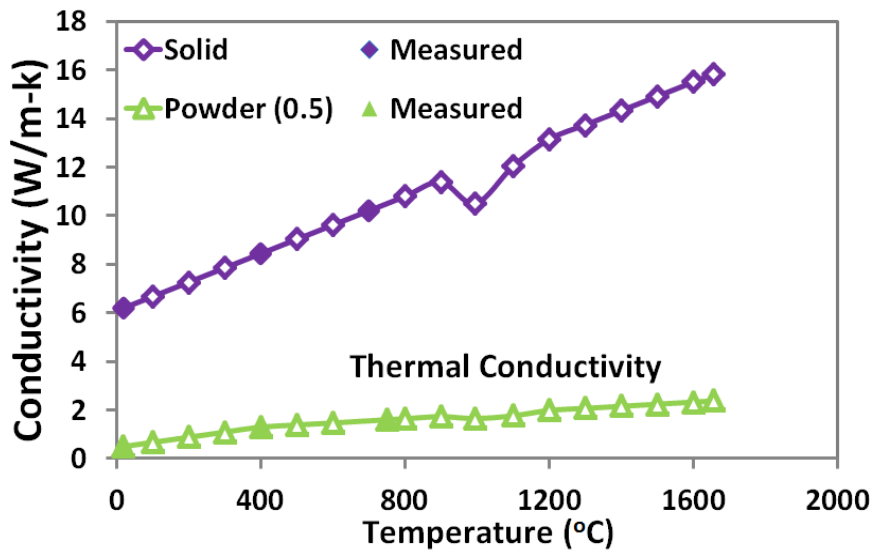


Figure 3.2. Temperature dependent thermal conductivity.

3.2.2 Finite Element Methodology

A 3D FE thermal simulation was developed and realized using commercial software (ABAQUS) to study the complex thermal phenomenon in EBAM. Figure 3.3 shows the model configuration and thermal boundary conditions. As a single scan path was simulated in this model, the base material was modeled as a solid. Then, a thin layer of powder on the top of the substrate was considered as a newly added material, which has the powder thermal properties. The electron beam heating occurs at the top surface of the powder layer and travels along the x-axis with a constant speed. To simplify the physical process, at the center of the area where the electron beam passes, if temperatures exceed the melting point, the node remains in the mesh. In addition, a symmetric condition was considered, and therefore, only a half of the computational domain was modeled and a semi-circular Gaussian heat flux distribution was defined as well. Because of a high energy intensity and a fast travel speed in EBAM, temperature gradients are expected to be very high, and thus, finer meshing was

required along the scanning path of the electron beam, also to directly incorporate the incident Gaussian heat-flux region. Coarser meshing was then used in the regions away from the heat affected zone. The fine meshing approach is necessary to enable calculations of the temperature contours, especially in the high temperature zone, with high accuracy, while without longer computational time. The model has a substrate dimension of 21 mm × 2.5 mm × 10 mm (x×y×z), and heat transfer elements (DC3D8) were used for the whole model. The element size in the scanning area was 50 μm × 50 μm × 17.5 μm (x×y×z) with the mesh size gradually increases with the distance away from the primary scanning area. The total element number for the thermal model is about 71000. The typical computational time for one simulation case is around 30 hours using two Inter(R) Xeon(R) E5 CPUs.

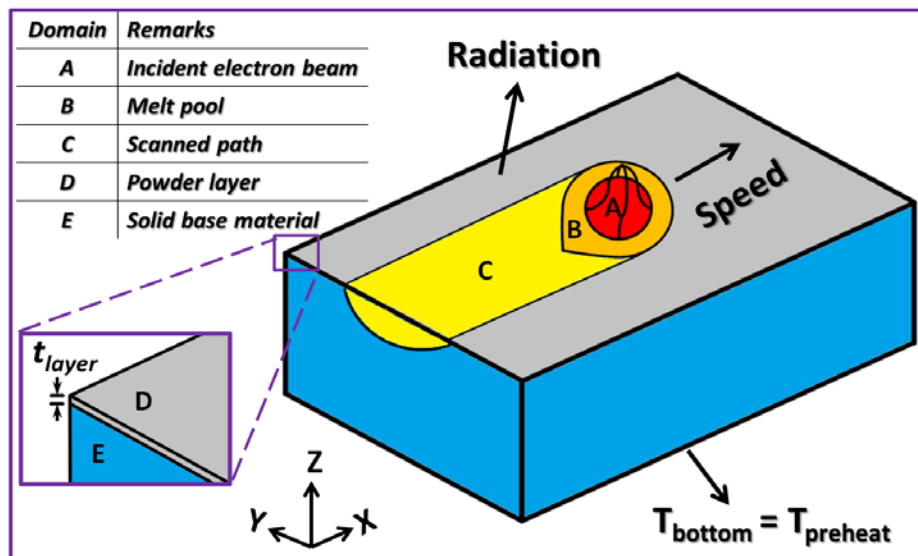


Figure 3.3. An illustration of thermal model and part geometry in finite element simulations.

Because the material state changes, e.g., powder to liquid and then to solid, a subroutine, UMATHT was embedded to assign material properties according to its state change. An internal state variable, as a material index, was defined to specify the material as powder or solid at a time frame. The material index can be 0 or 1 (0 – powder, 1 – solid). The

change criterion is: the material is melted and under cooling (i.e. $T > T_m$ & $dT/dt < 0$). After the subroutine is called in the beginning of every iteration check, it reads the material index of each node to determine the correct material properties to be assigned. As the state change in EBAM can only be one-way (i.e., from powder to solid), the material index will be locked as 1 whenever it becomes solid.

Process parameters used in simulations included fixed operating conditions such as the acceleration voltage, the powder layer thickness, and the preheat temperature, etc., as well as parameters subject to changes including the beam speed, the beam current and the beam diameter. Detailed process modeling and simulation parameters are listed in Table 3.1.

Table 3.1. Parameter list used in EBAM simulations.

Parameters	Values
Solidus temperature, T_S (°C)	1605 (Boyer et al., 1998)
Liquidus temperature, T_L (°C)	1655 (Boyer et al., 1998)
Latent heat of fusion, L_f (kJ/Kg)	40 (Boyer et al., 1998)
Electron beam diameter, Φ (mm)	0.55
Absorption efficiency, η	0.9 (Rouquette <i>et al.</i> , 2007)
Scan speed, v (mm/sec)	630~1415
Acceleration voltage, U (kV)	60 (Gaytan <i>et al.</i> , 2009)
Beam current, I_b (mA)	6.7
Powder layer thickness, t_{layer} (mm)	0.07
Porosity, ϕ	0.5
Beam penetration depth, d_p (mm)	0.062 (Zäh and Lutzmann, 2010)
Preheat temperature, $T_{preheat}$ (°C)	730

3.3 Results and Discussion

3.3.1 Typical Simulation Example

The FE thermal model was first implemented with parameters listed in Table 3.1, and the porosity of the powder layer was set at 0.5. The substrate was treated as solidified materials from previous layer depositions. One example of actual process parameters obtained from the experiments has also been incorporated into the FE model: 632.6 mm/s scanning speed and 6.7 mA beam current. The beam diameter was approximately as 0.55 mm for the focus offset used in the experiment, 19 mA (Al-Bermani *et al.*, 2010; Gong *et al.*, 2013b). The electron acceleration voltage is always 60kV. A single straight scan simulation was conducted and the temperature profile along the scanning path was extracted for further analysis.

Figure 3.4 shows thermal characteristics in the EBAM process. Figure 3.4 (a) shows the temperature contours in the entire model at the end of scanning; the melt pool shape and size are shown too, plotted with the threshold value of the melting point of Ti-6Al-4V. As expected, the high temperature zone, near the molten pool, is rather small, with the remaining part approaching a uniform temperature. Figure 3.4 (b) illustrates the temperature profile along the center line of the scan path with the beam center at 0 of the horizontal axis. Extremely rapid temperature rise and fall near the beam center are noted, with the peak temperature reaching between 2700 °C and 2800 °C. In addition, a plateau is noted corresponding to the latent heat of fusion for the phase change.

Figure 3.4 (c) shows the heating and cooling rate history at one location from the scan path. The horizontal dashed line indicates the boundary between heating and cooling. The

plateau is noted again in Figure 3.4 (c); it takes around 2 to 3 μs , which is generally just the duration that the cooling rate drops to a very low value. The abrupt drop in the heating period, which can be identified in the figure, indicates the phase change event. Another sharp transition occurred at around 9.5 ms indicates the change from the latent heat effect to solid-state cooling.

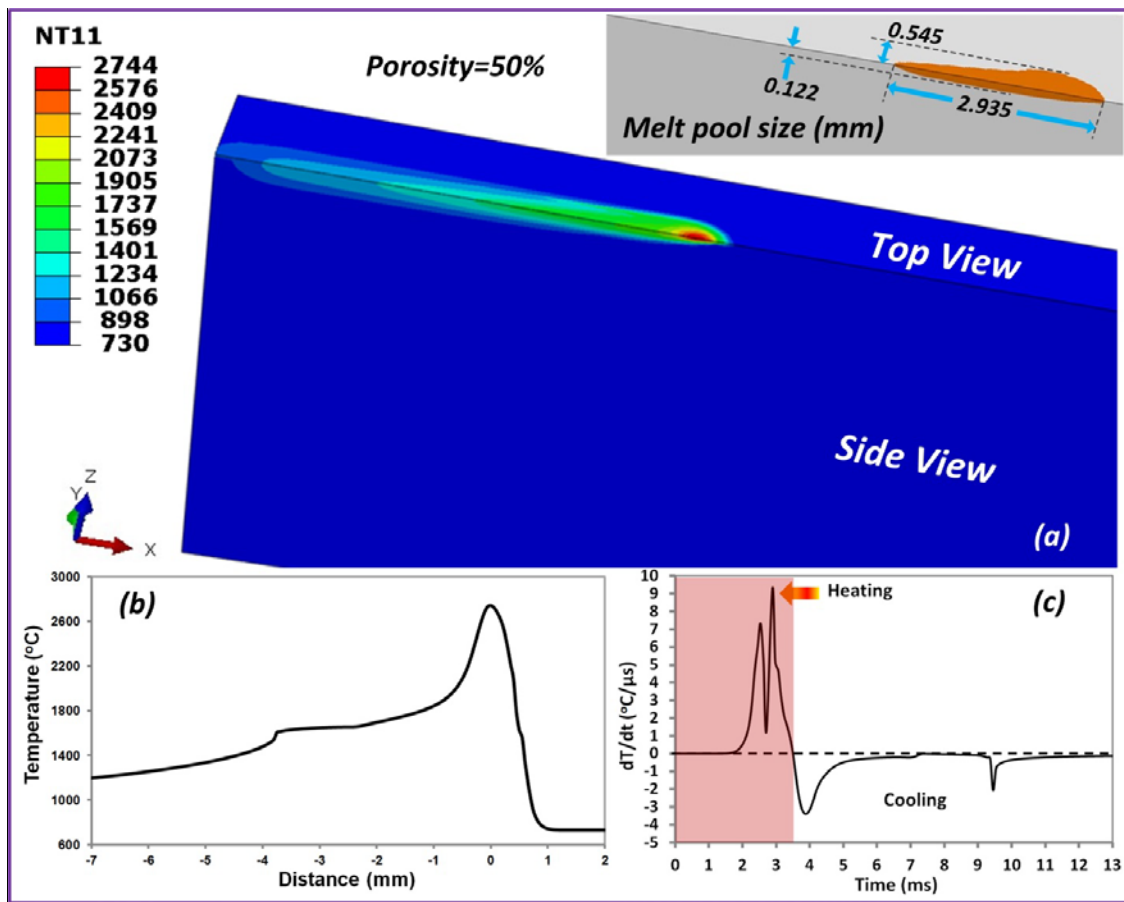


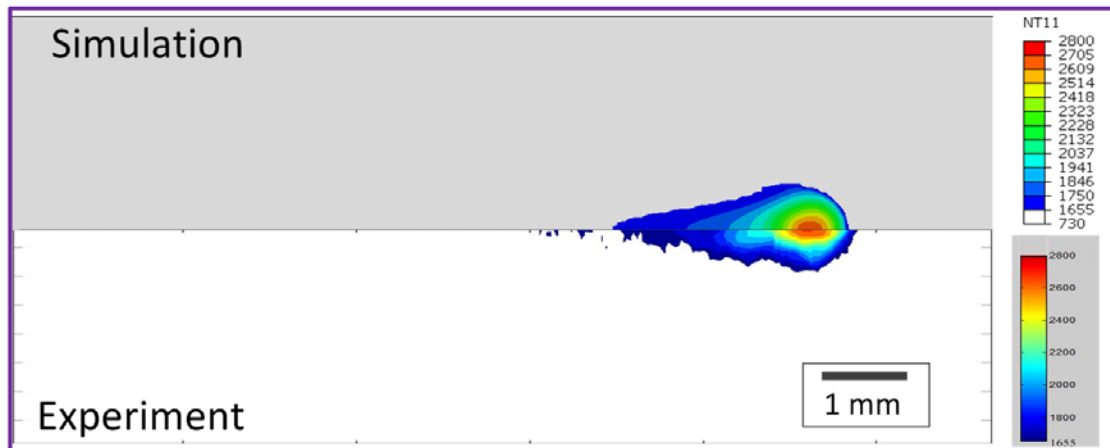
Figure 3.4. Typical simulation result: (a) temperature contour with melt pool geometry, (b) temperature profile, and (c) cooling rate.

3.3.2 Model Validation by Experiments

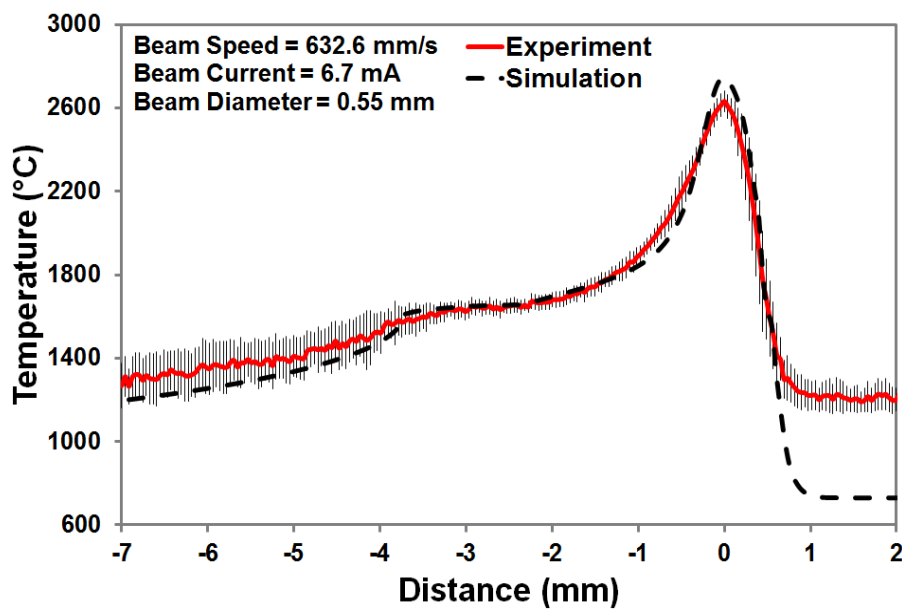
The setting of the FE thermal simulations was adjusted accordingly with two sets of experimental process parameters to verify the numerical model. Price (Price, 2014) has utilized a NIR thermal camera to capture process temperature and melt pool dimensions, and also developed temperature conversion method. The same method has been used in this study

for thermal model validation, detailed information can be found in (Price, 2014). The first set of parameters was: Speed Function (SF) 36, 26.53 mm build height and 19 mA focus offset, equivalent to 632.6 mm/sec scanning speed, 6.7 mA beam current and 0.55 mm beam diameter. The single scan simulations were conducted and the temperature profiles were compared, shown in Figure 3.5. Figure 3.5 (a) compares the melt pool shape and size between the simulation and the experiment. The comparison between simulations and experiments temperature profiles are shown in Figure 3.5 (b). Note that the NIR was unable to discern temperatures below 1100 °C, because of the detectable in the setting, and thus, data in the front of the melt pool cannot be used for comparisons (distance from 0.5 mm to 2 mm). The second set of process parameters were: SF36, 16.87 mm build height and 19 mA focus offset, equivalent to 728 mm/sec scanning speed, 7.2 mA beam current and estimated 0.55 mm beam diameter. The experimental average melt pool has a length of 2.72 mm and a width of 0.72 mm, while the simulation results show a length of 2.95 mm, a width of 1.09 mm, and a depth of 0.120 mm, with the error of 8.4% and 50.8% for the length and width, respectively. The comparison between simulations and experiments temperature profiles are shown in Figure 3.6. The experimental result is the average data from the two repeated builds of the experiment and the error bars show the range of standard deviations from the two tests. For both sets, it can be noted that the maximum temperature between the simulation and the experiment are fairly close, order of 100°C difference. The heating region, phase change region and cooling region matches reasonably well. For the second set, the cooling region from the maximum temperature to liquidus temperature shows some deviations. It can be concluded that, in general, the simulation results are in reasonable agreement with the

experiment, with an average error of 32 % for the melt pool sizes.



(a)



(b)

Figure 3.5. Temperature comparisons between simulation and experiment ($v = 632.6$ mm/s, $i = 6.7$ mA, $d = 0.55$ mm): (a) contour, and (b) profile.

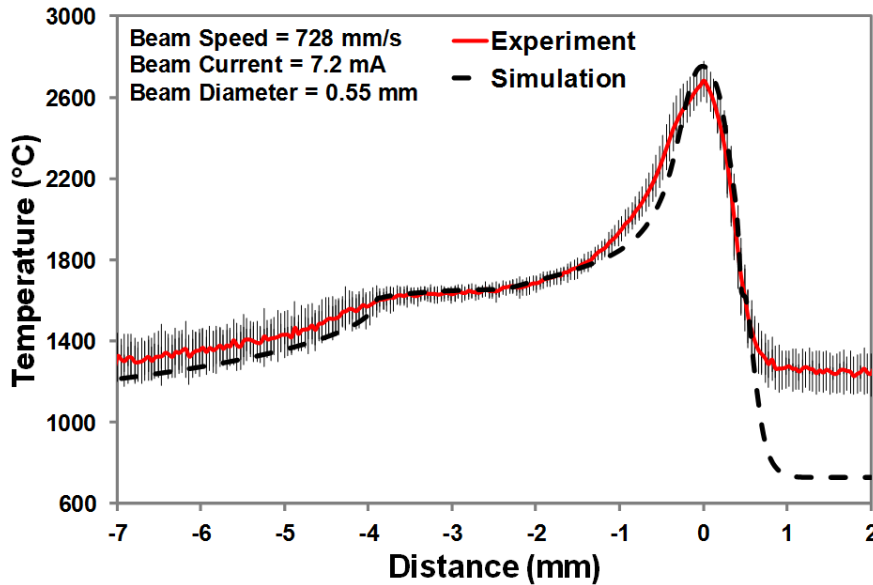


Figure 3.6. Model validation with another set of experiments with repeated tests ($v= 728$ mm/s, $i = 7.2$ mA, $d= 0.55$ mm).

3.3.2 Powder Porosity Effect

It has been pointed out that the powder porosity play a crucial role in the thermal behaviors in the EBAM process, governing the maximum process temperatures, melt pool sizes, and cooling rates, etc. Thus, a set of simulations with varied levels of the powder porosity (0 to 0.65) was conducted to shed light of the powder porosity effect on the thermal characteristics in EBAM. Figure 3.7 shows the temperature contours and molten pool geometries at various levels of porosity: 0 to 0.65 in the powder layer. Based on results in Figure 3.7 and Figure 3.8, a higher maximum temperature occurs at a higher porosity. In addition, the molten pool sizes increases in all dimensions (length, width and depth) with the increase of the powder porosity. This is due to a greater thermal resistance around the scan path, so that the heat is dissipated backward along the scan path and the depth as well as width direction. In the case of 0 porosity, the material is a solid, which is not realistic; however, it was tested to evaluate the possible error resulted from a simplified assumption

(i.e., using properties of a solid). Figure 3.9 compare the 2D temperature profile between a powder layer and a layer of solid.

Due to the significance decrease in the thermal conductivity from solid to powder and less packing density, the maximum temperature for the powder-layer case (50% porosity) increases to 2744°C, which is around 380 °C higher than that of the solid layer case. As a result, a wider and deeper melt pool occurs, shown in Figure 3.8. Meanwhile, a longer melt pool is also seen with the application of the powder top layer. This could be attributed to the occurrence of the material state change after the powder is melted and solidified. The solidified material has the properties of the solid bulk material, i.e. thermal conductivity increases to the level of solid materials. Because of a low thermal conductivity along the transverse direction and ahead of the scan path, the heat resistance is much lower along the opposite direction of the scan path. Therefore, the heat dissipation is more dominant along the backward direction, and thus, more heat is confined in the scan path. As a result, the melt pool is elongated.

Moreover, a solid top layer results in a lower heating-cooling rate due to a rather low thermal resistance around the scan path. More heat can dissipate from the heat source, and hence, there is not much heat stored in the fusion zone so that the heating and cooling rates are much lower than those of the powder-layer cases. It can also be observed that the solid top layer has a noticeably lower cooling rate than the case with a powder top layer (50% porosity), also shown in Figure 3.9. For the powder top layer case, the temperature is to drop approximately to 1655 °C about 2.4 mm away from the beam center, while it is about 1.75 mm away from the beam center for the solid top layer. Plateaus are noted from the

simulations for both simulations, as a result of more mass and more confined heat required for latent heat fusion effect in the scan path, the plateau of the solid top layer is longer than that of the powder top layer. Moreover, the temperatures after the fusion boundary are lower than those of the powder top layer. Thus, it is obvious that the simulation using solid properties would have underestimated the part surface temperatures and the melt pool size.

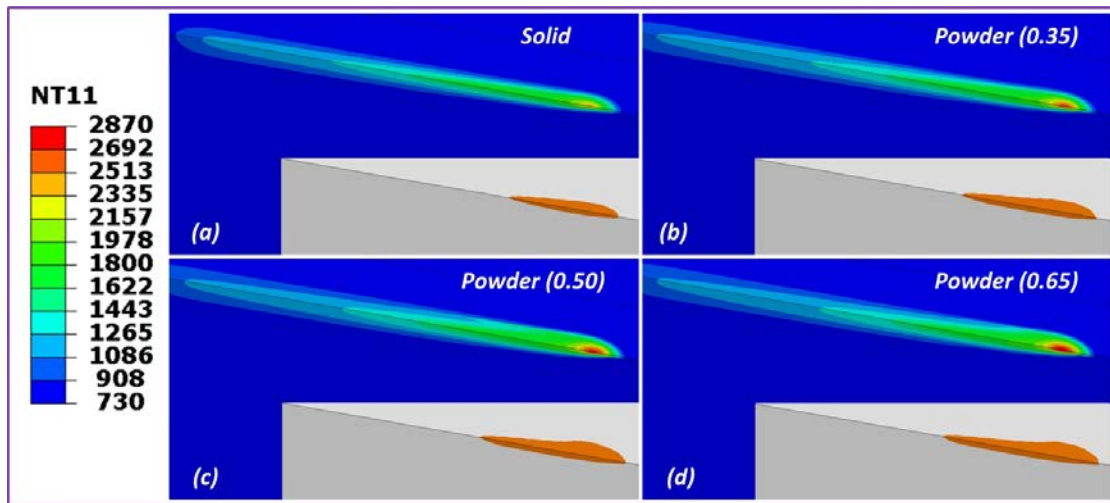


Figure 3.7. Temperature contours and molten pool geometries for powder layer of various levels of porosity.

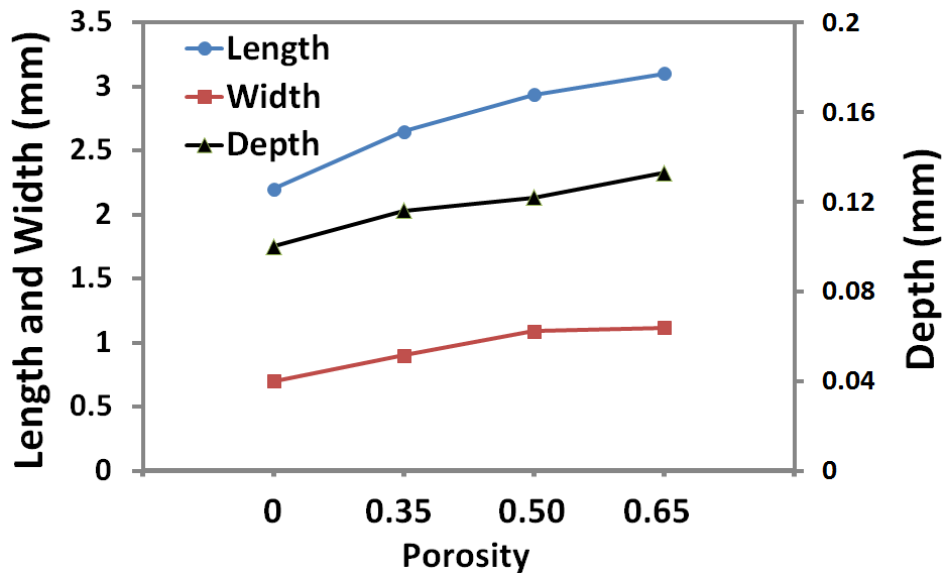


Figure 3.8. Simulated melt pool sizes for different levels of powder porosity for the top layer.

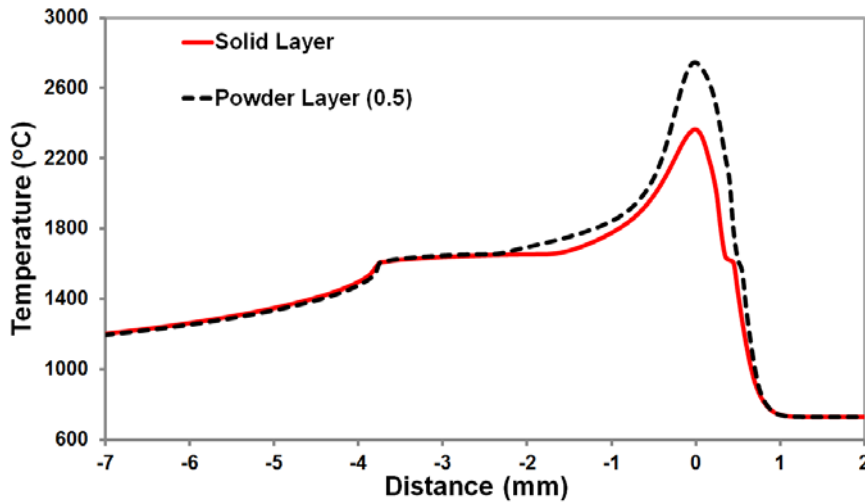


Figure 3.9. Simulated temperatures comparing profiles between using powder vs. solid properties as the top layer.

3.4 Conclusion

In this study, a 3D thermal model, using an FE method, was developed for EBAM process temperature simulations. The model incorporated a moving heat source with a Gaussian volumetric intensity, temperature-dependent properties and latent heat of fusion, etc. Moreover, the thermal conductivity of preheated Ti-6Al-4V powder, preserved as in the powder-bed condition, was measured at different temperatures and implemented in the FE model. The experimental data, temperatures and melt pool sizes, was compared against the simulations for model validations. The major findings can be summarized as follows.

1. The peak process temperatures in EBAM using Ti-6Al-4V powder are on the order around 2700 °C, and the melt pools have dimensions of about 2.94 mm, 1.09 mm and 0.12 mm, in length, width and depth, respectively, at a beam speed of 632.6 mm/s to 728 mm/s, a beam current of 6.7 mA to 7.2 mA, and a diameter of 0.55 mm.

2. In general, simulation results agree reasonably well with multiple sets in the experiments, especially temperature profiles in the rapid heating and cooling curves, as well

as in the phase change curve. The average error of the melt pool sizes is 32 %.

3. From simulations, the powder porosity is found critical to the thermal characteristics in EBAM. Increasing the powder porosity will increase the melt pool size (e.g., length from 2.65 mm to 3.1 mm for a porosity level of 0.35 and 0.65). On the other hand, increasing the porosity will elevate the peak temperature, from 2610 °C to 2870 °C for 0.35 and 0.65 porosity, respectively.

Acknowledgements

This research is supported by NASA, No. NNX11AM11A, and is in collaboration with Marshall Space Flight Center (Huntsville, AL), Advanced Manufacturing Team in Nonmetallic Branch.

References

- Al-Bermani, S., Blackmore, M., Zhang, W., & Todd, I. (2010). The origin of microstructural diversity, texture, and mechanical properties in electron beam melted Ti-6Al-4V. *Metallurgical and materials transactions a*, 41(13), 3422-3434.
- Available from Arcam website. Available from: <http://www.arcam.com/>. Accessed June 21, 2013.
- Available from ORNL youtube website. Available from: <http://www.youtube.com/watch?v=BxxIVLnAbLw>. Accessed April 04, 2014.
- Biamino, S., Penna, A., Ackelid, U., Sabbadini, S., Tassa, O., Fino, P., Badini, C. (2011). Electron beam melting of Ti-48Al-2Cr-2Nb alloy: microstructure and mechanical properties investigation. *Intermetallics*, 19(6), 776-781.
- Boyer, R., Welsch, G., & Collings, E. W. (Eds.). (1998). *Materials Properties Handbook: Titanium Alloys* (2nd ed.). Materials Park, OH, USA.
- Cline, H., & Anthony, T. (1977). Heat treating and melting material with a scanning laser or electron beam. *Journal of Applied Physics*, 48(9), 3895-3900.
- Cormier, D., Harrysson, O., & West, H. (2003). Characterization of H13 steel produced via electron beam melting. 14th Annual Solid Freeform Fabrication Symposium,

University of Texas, Austin, Texas, 4-6 August 2003.

- Gaytan, S. M., Murr, L. E., Medina, F., Martinez, E., Lopez, M. I., & Wicker, R. B. (2009). Advanced metal powder based manufacturing of complex components by electron beam melting. *Materials Technology*, 24, 180-190.
- Gong, H., Rafi, K., Karthik, N., Starr, T., & Stucker, B. (2013b). Defect morphology in ti-6al-4v parts fabricated by selective laser melting and electron beam melting. 24th Annual International Solid Freeform Fabrication Symposium - An Additive Manufacturing Conference, Austin, TX, USA, August 12-14, 2013.
- Gong, X., Anderson, T., & Chou, K. (2012). Review on powder-based electron beam additive manufacturing technology. ASME/ISCIE 2012 International Symposium on Flexible Automation, St. Louis, MO, June 18-20, 2012, ISFA2012-7256.
- Gong, X., Cheng, B., Price, S., & Chou, K. (2013a). Powder-bed electron-beam-melting additive manufacturing: powder characterization, process simulation and metrology. ASME District F Early Career Technical Conference, Birmingham, AL, November 2-3, 2013.
- Heinl, P., Rottmair, A., Korner, C., & Singer, R. F. (2007). Cellular titanium by selective electron beam melting. *Advanced Engineering Materials*, 9(5), 360-364.
- Kolossov, S., Boillat, E., Glardon, R., Fischer, P., & Locher, M. (2004). 3D FE simulation for temperature evolution in the selective laser sintering process. *International Journal of Machine Tools and Manufacture*, 44(2-3), 117-123.
- Lin, T. H., Watson, J. S., & Fisher, P. W. (1985). Thermal conductivity of iron-titanium powders. *Journal of Chemical & Engineering Data*, 30(4), 369-372.
- Liu, C., Wu, B., & Zhang, J. (2010). Numerical investigation of residual stress in thick titanium alloy plate joined with electron beam welding. *Metallurgical and Materials Transactions B*, 41(5), 1129-1138.
- Mills, K. C. (2002). Recommended values of thermophysical properties for selected commercial alloys: Woodhead Publishing.
- Murr, L., Martinez, E., Gaytan, S., Ramirez, D., Machado, B., Shindo, P., Ciscel, D. (2011). Microstructural architecture, microstructures, and mechanical properties for a nickel-base superalloy fabricated by electron beam melting. *Metallurgical and Materials Transactions A*, 42(11), 3491-3508.
- Patil, R. B., & Yadava, V. (2007). Finite element analysis of temperature distribution in single metallic powder layer during metal laser sintering. *International Journal of Machine*

Tools and Manufacture, 47(7-8), 1069-1080.

- Price, S. (2014). On temperature measurements and analysis in electron beam additive manufacturing using near infrared thermography. Master thesis, The University of Alabama, Tuscaloosa, AL.
- Rai, R. (2008). Modeling of heat transfer and fluid flow in keyhole mode welding. Ph.D. thesis, The Pennsylvania State University, State College, PA.
- Ramirez, D. A., Murr, L. E., Martinez, E., Hernandez, D. H., Martinez, J. L., Machado, B. I., Wicker, R. B. (2011). Novel precipitate–microstructural architecture developed in the fabrication of solid copper components by additive manufacturing using electron beam melting. *Acta Materialia*, 59(10), 4088-4099.
- Roberts, I. A., Wang, C. J., Esterlein, R., Stanford, M., & Mynors, D. J. (2009). A three-dimensional finite element analysis of the temperature field during laser melting of metal powders in additive layer manufacturing. *International Journal of Machine Tools and Manufacture*, 49(12-13), 916-923.
- Rouquette, S., Guo, J., & Le Masson, P. (2007). Estimation of the parameters of a Gaussian heat source by the Levenberg-Marquardt method: application to the electron beam welding. *International Journal of Thermal Sciences*, 46(2), 128-138.
- Sih, S. S., & Barlow, J. W. (2004). The prediction of the emissivity and thermal conductivity of powder beds. *Particulate Science and Technology*, 22, 291-304.
- Tolochko, N. K., Arshinov, M. K., Gusarov, A. V., Titov, V. I., Laoui, T., & Froyen, L. (2003). Mechanisms of selective laser sintering and heat transfer in Ti powder. *Rapid Prototyping Journal*, 9, 314-326.
- Yang, J., Sun, S., Brandt, M., & Yan, W. (2010). Experimental investigation and 3D finite element prediction of the heat affected zone during laser assisted machining of Ti6Al4V alloy. *Journal of Materials Processing Technology*, 210(15), 2215-2222.
- Zäh, M. F., & Lutzmann, S. (2010). Modelling and simulation of electron beam melting. *Production Engineering. Research and Development*, 4, 15-23.

CHAPTER 4

ON PROCESS TEMPERATURE IN POWDER-BED ELECTRON BEAM ADDITIVE MANUFACTURING: PROCESS PARAMETER EFFECTS

Abstract

Build part certification has been one of the primary roadblocks for effective usage and broader applications of metal additive manufacturing (AM) technologies including powder-bed electron beam additive manufacturing (EBAM). Process sensitivity to operating parameters, among others such as powder stock variations, is one major source of property scattering in EBAM parts. Thus, it is important to establish quantitative relations between the process parameters and process thermal characteristics that are closely correlated with the AM part properties.

In this study, process parameter effects on the thermal characteristics in EBAM with Ti-6Al-4V powder were investigated, using the system-specific setting called “speed function” index that controls the beam speed and the beam current during a build. EBAM parts were fabricated using different levels of speed function (SF) index (20 to 65) and examined in the part surface morphology. In addition, the thermal model, developed Chapter 3, was further employed for EBAM temperature predictions, and then compared with the experimental results.

The major results are summarized as follows. SF setting strongly affects the EBAM part quality including the surface morphology and surface roughness. In general, a higher SF index tends to produce parts of rougher surfaces with more pore features. Increasing the beam

speed will reduce the peak temperatures; also reduce the melt pool sizes. Simulations conducted to evaluate the beam speed effects are in reasonable agreement compared to the experimental measurements in temperatures and melt pools sizes. However, the results of a lower SF case, SF20, show larger differences between the simulations and the experiments, about 58% for the melt pool size. Moreover, the higher the beam current, the higher the peak process temperatures, also the larger the melt pool. On the other hand, increasing the beam diameter monotonically decreases the peak temperature and the melt pool length.

4.1 Introduction

The benefits of metal additive manufacturing (AM) have been globally recognized lately. Metal AM has the potential to revolutionize product design and manufacturing in the entire manufacturing enterprise. In particular, metal AM using the powder-bed-fusion process, e.g., electron beam additive manufacturing (EBAM), has advanced substantially to enter into major manufacturing arenas such as transportation and medical industries. However, there are still several technical challenges to be addressed including powder characterization, AM standards, process modeling and control, and part qualification, etc. are the major areas of strong research needs. It has also been reported that metal parts made by AM processes generally have large scattering in mechanical properties. According to a recent workshop on metal AM, part quality consistency, among other issues, is the major barrier to overcome in order to increase and broaden effective usage of metal AM (Jurren, K.(ed), 2012.). The main obstacles for part certification in metal AM processes include variations in powder materials, deviations in process condition, and lack of relevant knowledge to fully understand the relation between feedstock materials, process physics and variables, and part

properties. Presently, metal AM part fabrications and the selection of process parameters are a trial-and-error iterative process, requiring repeated runs.

Since EBAM is a rather complex physical process, it is important to have fundamental understanding of how process parameters affect thermal characteristics. In Chapter 3, a comprehensive thermal model has been developed to investigate the process temperatures in EBAM. In addition, the thermal model has been validated by temperature measurements of the build surface during EBAM using a near infrared (NIR) thermal imager. Moreover, the thermal model developed was also employed to examine and compare to the experimental results.

Based on some studies (Kumar and Roy, 2009; Soylemez *et al.*, 2010; Zäh and Lutzmann, 2010; Jamshidinia *et al.*, 2013), process parameters may offer useful information of the melt pool evolution during the heating-cooling cycle. The process parameters may help better control the build part quality. The objective of this study was to investigate how critical process parameters such as the beam speed, current and diameter affect the thermal behavior and characteristics in EBAM. The experimental methods used in recent work were applied to extensively investigate the process parameter effects on the thermal characteristics such as the peak temperatures and the melt pool size in the EBAM process. The finite element thermal model developed for the EBAM process in Chapter 3 was applied for thermal simulations to study process parameters effect. Simulation results were compared against experimental temperature measurements.

4.2 Research Approach

The Arcam S12 EBAM machine at NASA's Marshall Space Flight Center was utilized

to fabricate the test parts. The default machine settings included 60 keV, 0.1 Pa vacuum, 70 μm layer thickness and 0.2 mm hatch spacing. The Ti-6Al-4V powder used in this study has a porosity of around 50%. The EBAM machine uses a parameter setting called the speed function (SF) index to control the translational speed of the electron beam during the fabrication of the part. For each speed function value, though, the actual translational speed as well as the beam current will change along the build height. The information of the speed function algorithm can be found in Mahale (Mahale, 2009) who noted that the beam speed dropped significantly during the fabrication of the first several millimeters of the part then gradually stabilized for the rest of the build. The beam current was also found to follow a similar trend. Mahale also observed that increases in the speed function index resulted in increases of the beam speed at equivalent build heights; however, the beam current was not affected by changes in the speed function index.

This study was conducted to gain better understanding of the SF algorithms and to learn the effects of the SF index on the process temperatures and the molten pool size. The parts were fabricated each with a different speed function index: 20, 36, 50, and 65. Each part had a 60 mm by 5.25 mm cross-section, length by width (in X and Y) and was about 25 mm tall. The parts were spaced 1 mm apart from each other in order to fit all of them into the field of view of the camera. A CAD model of the parts in their arrangement for fabrication is shown in Figure 4.1. The experiment was conducted with simultaneously monitoring the fabrication using the LumaSense MCS640 NIR thermal imager, the detailed experiment set up information can be found in (Price, 2014). The experiments were repeated 2 times for each SF tested.

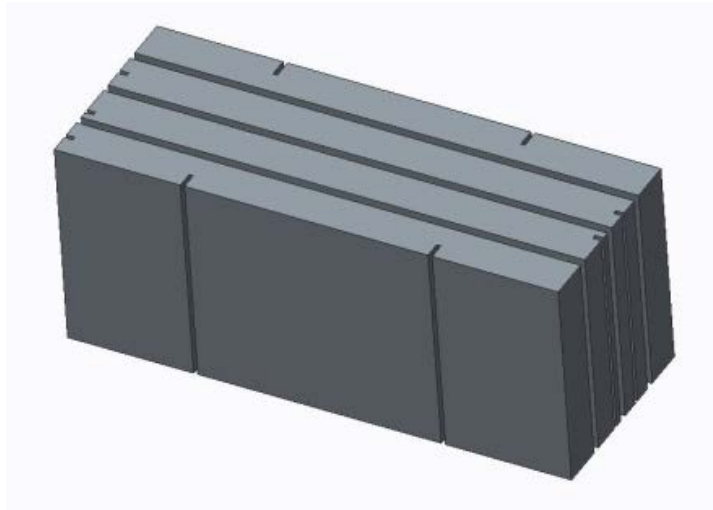


Figure 4.1. A CAD model used in EBAM experiments for temperature measurements.

It was expected that the process parameter setting, SF, will affect the build part surface quality and microstructures. Thus, a stereoscope was applied to capture the three dimensional surface features of different SF cases. In addition, a white light interferometer (Veeco NT1100) was then applied to obtain a quantitative analysis of the surface characteristics. An objective lens of 50X and a 0.5X field of view lens were used. The lateral resolutions are about 350 nm and the vertical resolution is 10 nm. A low scanning speed was employed. The built-in stitching method was applied to define an approximately $600\ \mu\text{m} \times 700\ \mu\text{m}$ scanning region, located around the center position of the top scanning surface of each part, with surface roughness analyzed.

Average two dimensional (2D) temperature profiles of the molten pool along the scanning direction were generated using the procedure outlined in study by Price (Price, 2014). These average temperature profiles were used to estimate the molten pool length by identifying the measured liquidus temperature on the temperature profile and measuring the distance between the location of this temperature on the heating and cooling sides of the temperature profile. The molten pool widths were determined by using a temperature profile

along the transverse direction of the molten pool (Price, 2014).

The FE simulation codes developed in chapter 3 using ABAQUS software was continuously utilized in this study. The model geometry and size, the material properties, solid and powder, the boundary conditions and element meshing were exactly the same. The attributes associated with the electron beam heat source, i.e., speed, power and diameter, were varied accordingly to the experimental setting and actual conditions. The information of actual beam speeds and the beam currents was then input to the developed thermal model for temperature result comparisons with experimental data; in particular, temperature profiles and melt pool sizes were analyzed and studied.

4.3 Results and Discussion

4.3.1 Beam Speed Effects.

4.3.1.1 Part Surface Morphology and Microstructures

Figure 4.2 displays the 4 EBAM parts fabricated with different SF indices. The appearance of the top surfaces is noticeably different. Parts built using a higher SF seem to show more fish-scale patterns with some visible pores. Figure 4.2 (a) shows surface features of 4 build parts from the stereoscope. SF20 case has a clear raster-pattern in the scanning area without any irregular structures, SF36 case also shows some raster-patterns with small line features in irregular directions noted. On the other hand, SF50 case exhibits large line features of irregular directions and raster-pattern can hardly be observed and finally the SF65 surface has several porous features. Moreover, Figure 4.2 (b) shows the surface morphology color maps for all SF cases; the regular or irregular line features can be clearly identified here with higher roughness compared to other regions. SF65 case does not show clear linear

patterns. It can also be noted that the surface roughness (of the scanning surface of build samples) increases with the increase of SF index (also the scanning speed), 1.65 μm from SF20 vs. 17.34 μm from SF65, shown in Figure 4.2 (c). The results demonstrate that the energy density, calculated as the absorbed electron beam power divided by the product of the beam speed and the hatch spacing (Song and Koenig, 1997), affects the surface roughness; a decrease in the energy density, through the increase of the scanning speed, results in an increase of build part surface roughness.

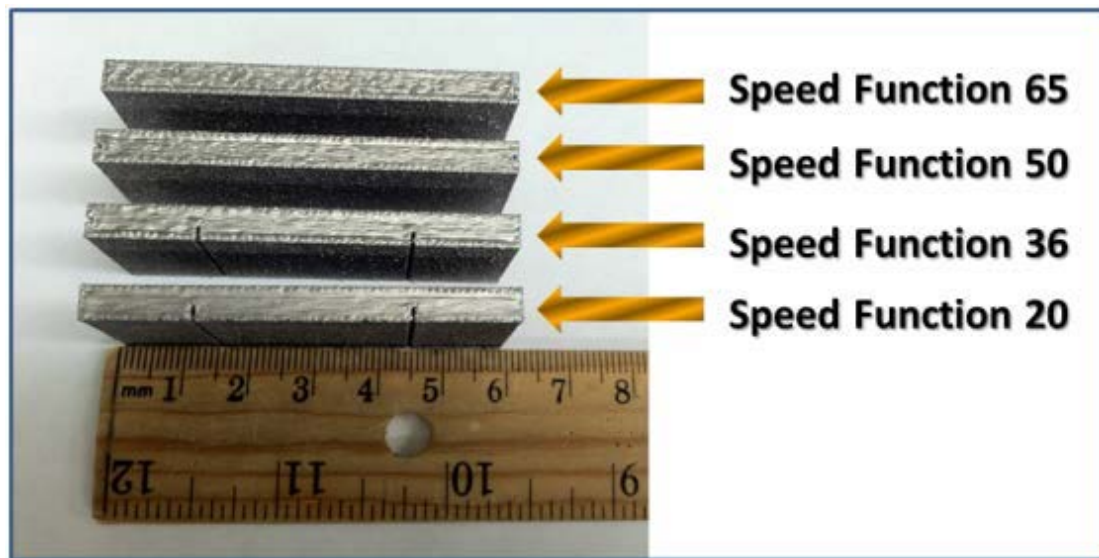
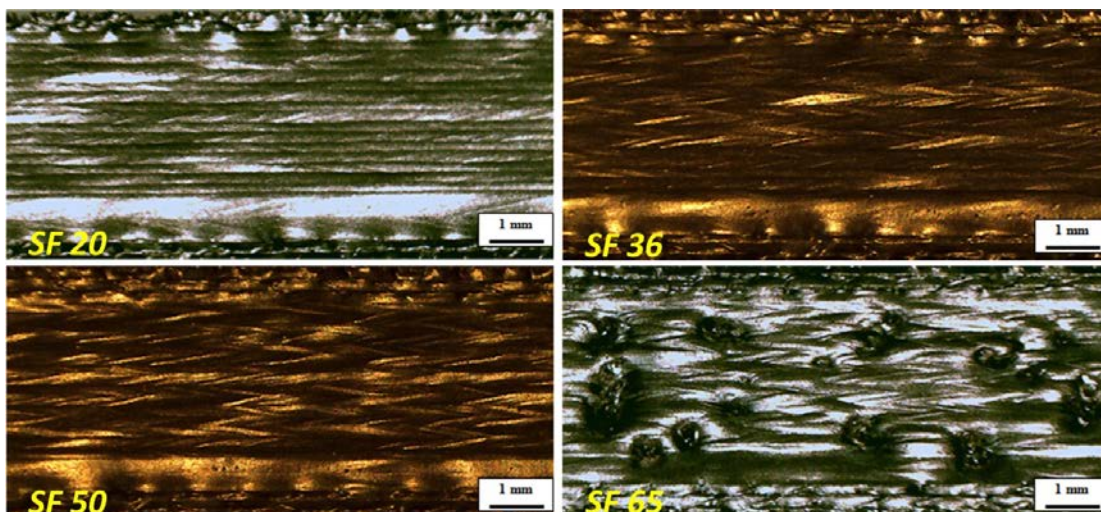
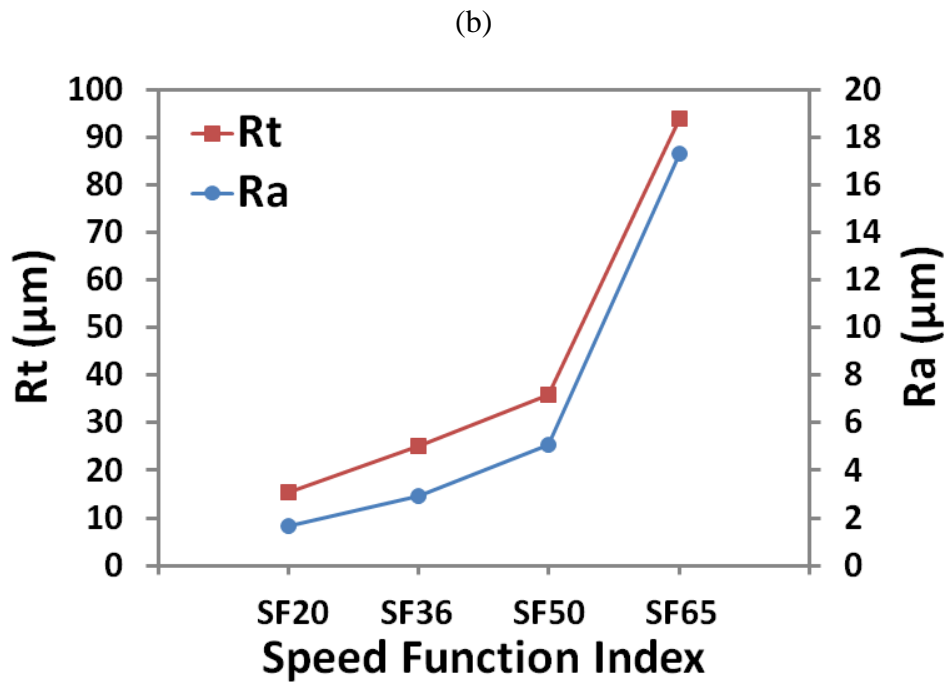
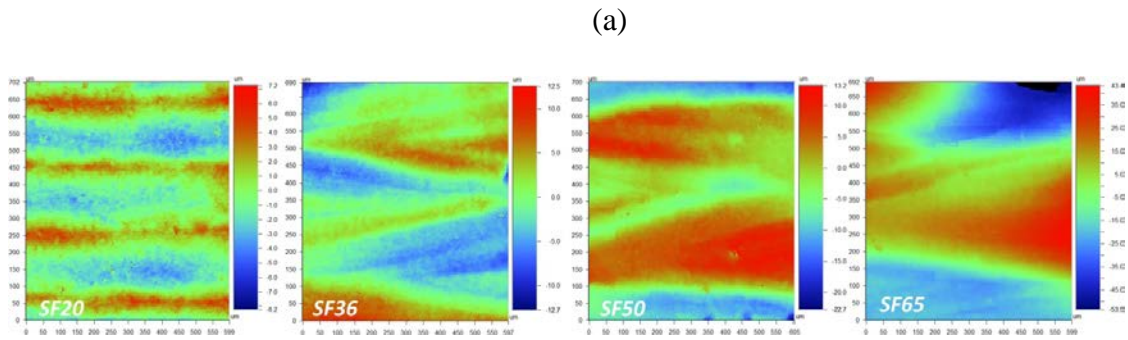


Figure 4.2. Fabricated parts from EBAM experiments with different speed function (SF) values.





(c)

Figure 4.3. EBAM build part surface morphology vs. SF: (a) stereoscopic images, (b) white-light interferometric images, and (c) surface roughness.

The average cooling rate for each beam speed was estimated, from the temperature profile, over the interval from the maximum temperature to the solidus temperature. Shown in Figure 4.4, with a given beam power, increasing the scanning speed would increase the cooling rate, which will form smaller columnar β grains (Bontha *et al.*, 2009).

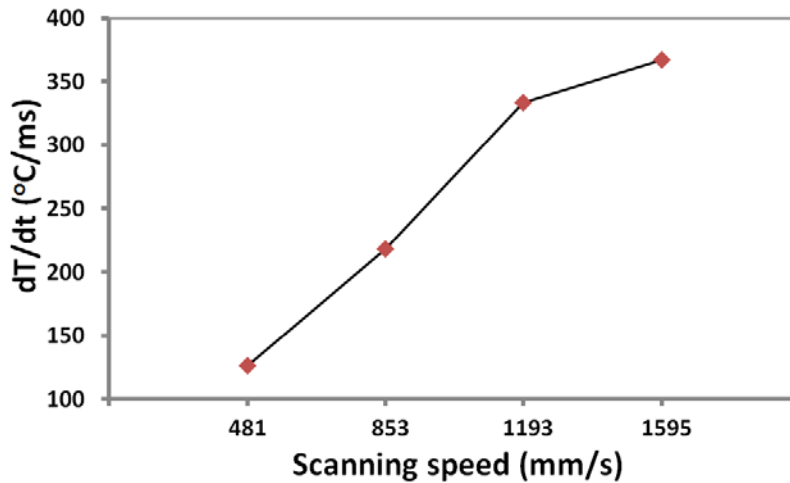
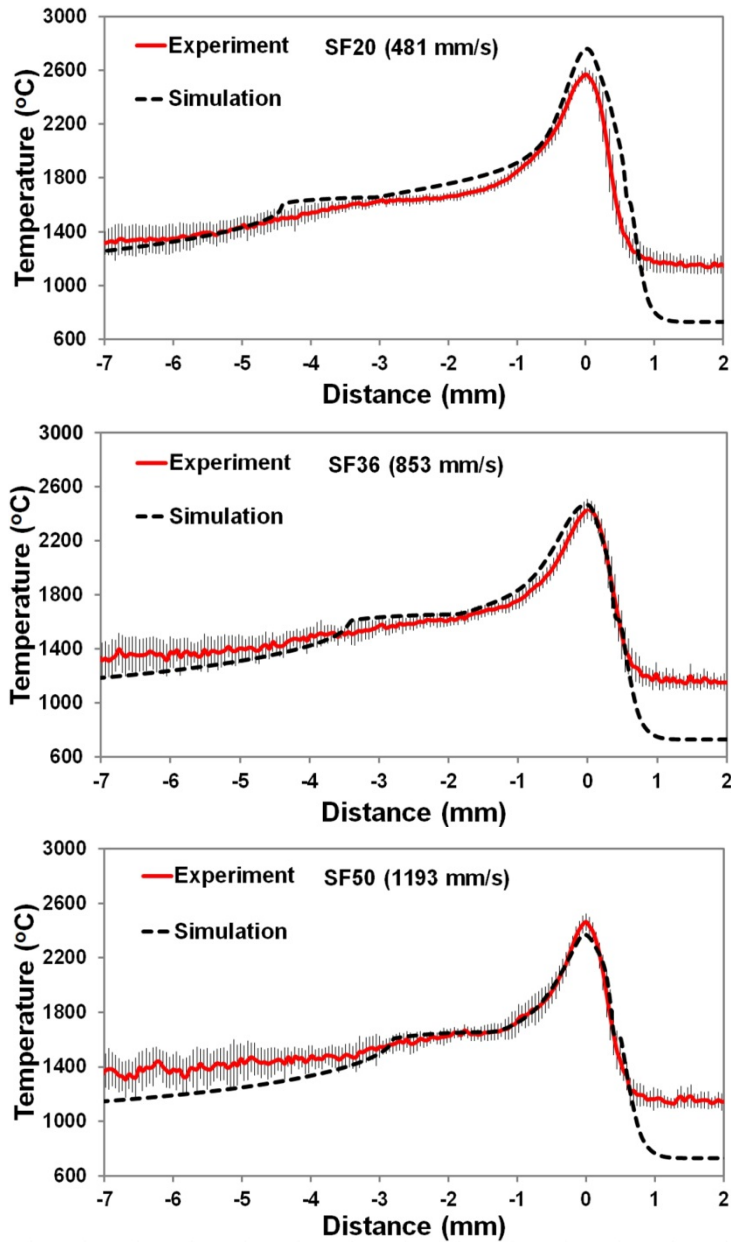


Figure 4.4. Cooling rates associated with different beam speeds.

4.3.1.2 Simulation Result Comparisons

Single straight scan simulations have then been conducted incorporating experimental process parameters (beam speed and current) for four different SF cases at 6.65 mm build height, the beam current is 7.7 mA and beam diameter is approximately 0.65 mm. The simulated temperatures were then compared with experimental temperatures and melt pool sizes. The measured profiles have been converted to true temperature using the aforementioned method (Price, 2014). Figure 4.5 compares temperature profiles, simulation vs. experiment, from 4 SF cases; the results show close match between experimental and simulated profiles. Figure 4.6 compares the melt pool sizes; the simulation and experimental results are in reasonably agreement, except the SF20 case. Compared to the experimental results, the average error of the simulated melt pool length and width have are 28.6% and 17.6%, respectively, excluding the SF20. Figure 4.7 illustrates the simulated melt pool size and shape, also clearly showing the trend of the melt pool size; increasing the beam speed will reduce the melt pool length and width, due to reduced energy density input from a higher travelling speed.

The differences between the simulations and experiments, mostly at a low temperature range (below 1300 °C), may be attributed to: (1) detectable limit at low temperatures (~1400 °C), (2) liquidus temperature identification, and (3) residual heat from hatch scanning in the experiment.



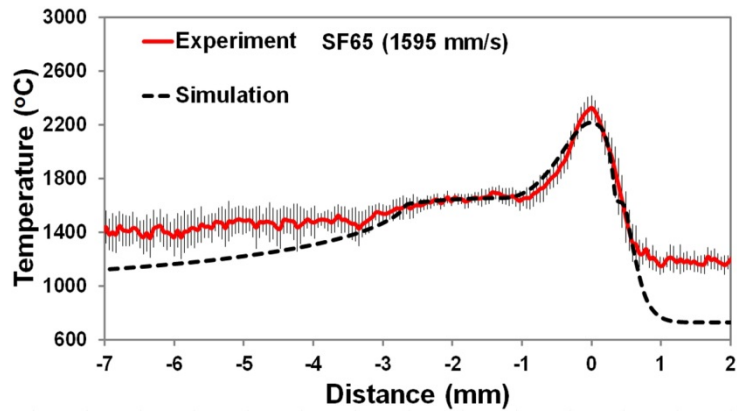


Figure 4.5. Temperature profile comparisons, simulation vs. experiment, for 4 beam speeds

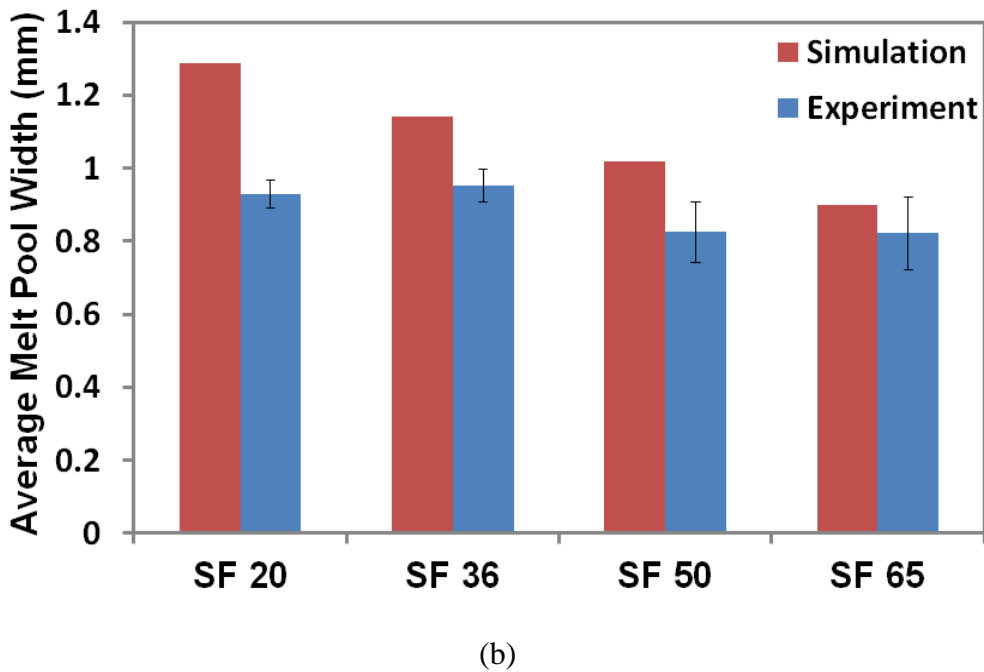
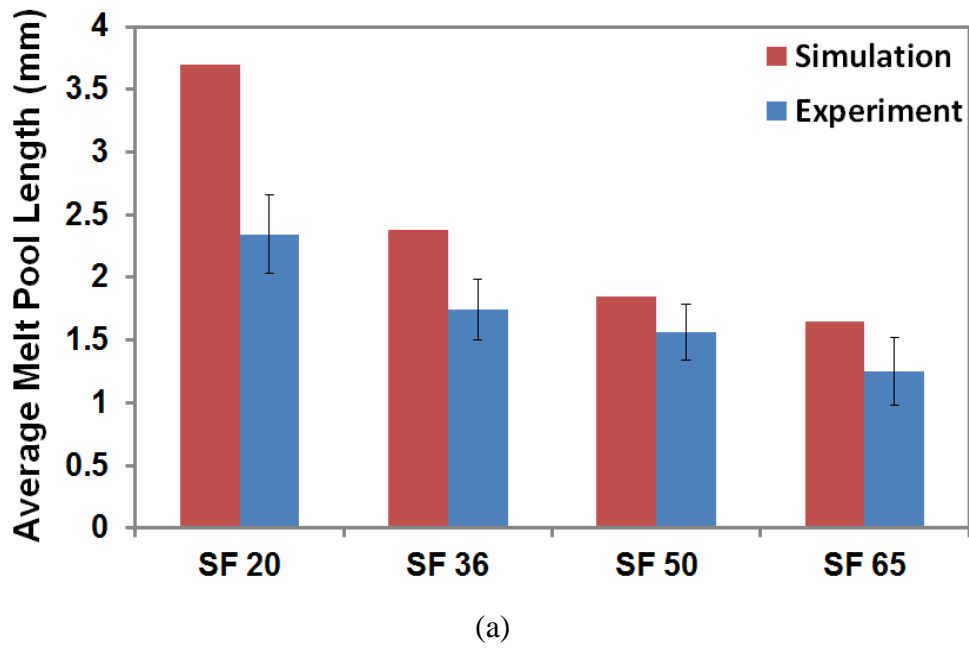


Figure 4.6. Melt pool size comparisons, simulation vs. experiment, for 4 SF values: (a) length, and (b) width.

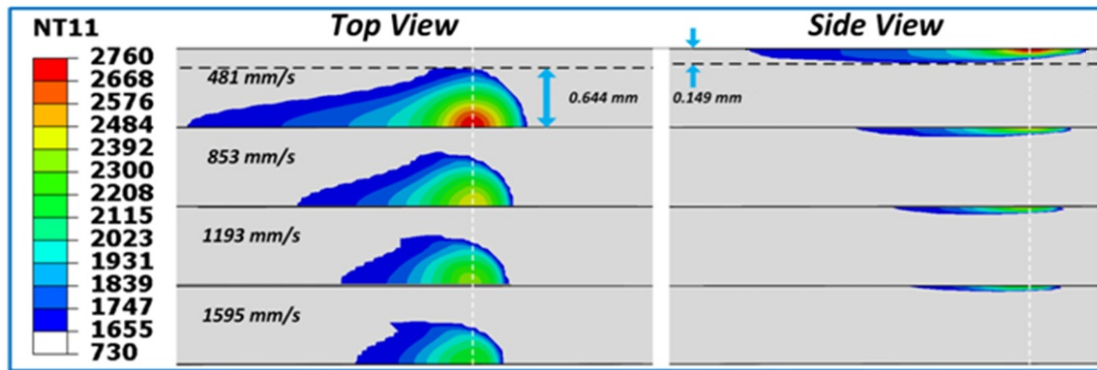


Figure 4.7. Melt pool size and shape illustration (simulations) at 4 different beam speeds.

4.3.2 Beam Current and Beam Diameter Effects

Since the beam current cannot be explicitly adjusted from the process setting, while it varies along the build height, different cases from the experiments were examined to identify combined conditions of similar beam speeds, but distinct beam currents. For SF50 case at 24.43 mm build height, the beam speed and the beam current were 529.4 mm/s and 4.8 mA (Condition 1), respectively. While for SF20 case at 6.65 mm build height, the beam speed and the beam current were 481 mm/s and 7.7 mA (Condition 2), respectively. These two cases, with less than 10% beam speed difference, offer an opportunity to analyze the beam current effect. The beam diameter was the same, 0.65 mm. The melt pool lengths from the experimental results are 1.48 mm for Condition 1 vs. 2.35 mm for Condition 2 (Figure 4.8), indicating considerable effects from the beam current. The thermal model was further employed to explore the beam current effect. The actual process parameter sets used in the experiments for the two cases were implemented in the FE model, 4.8 mA and 7.7 mA of beam currents and an estimated 0.65 mm beam diameter. The scanning speed used was the average of the actual beam speed from the two cases (Condition 1 and Condition 2), 505.5

mm/sec. Another simulation of the same beam speed and diameter but different beam current, 2.5 mA, was also conducted to better illustrate the beam current effect from the simulation viewpoint.

Figure 4.8 shows the simulation results; the temperature profiles are in good agreement with the experimental temperature profiles. The simulated melt pool sizes also show the same trend as obtained from the experiments, a noticeable decrease in the melt pool length, but a less reduction in the width when the beam current is decreased. In addition, the max temperature is higher for a higher beam current, 1896 °C for 2.5 mA vs. 2733 °C for 7.7 mA.

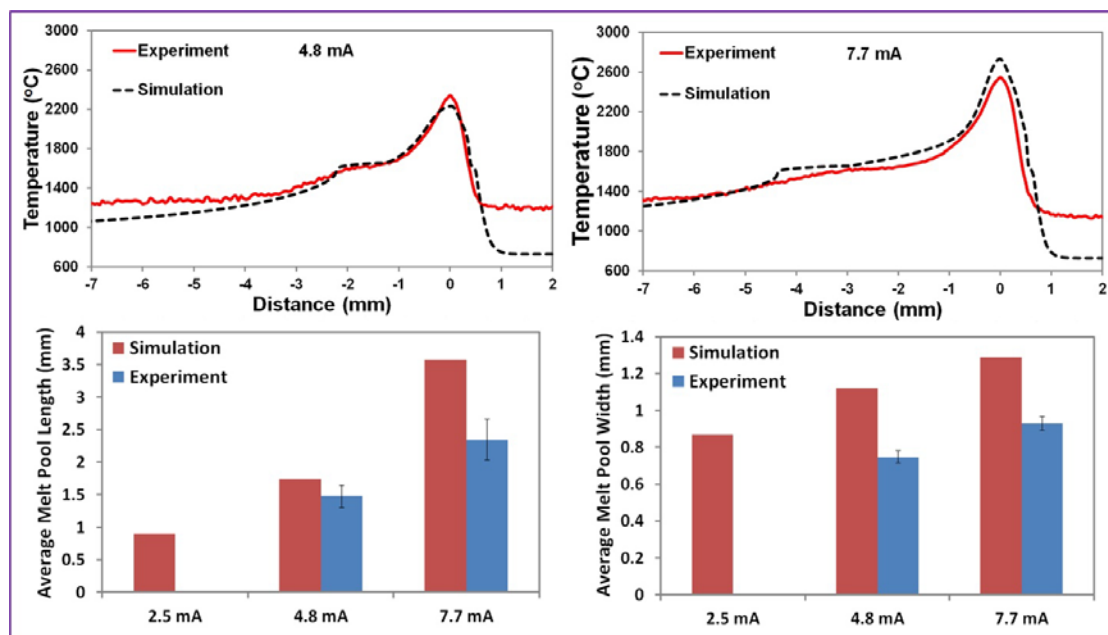


Figure 4.8. Beam current effects on EBAM process temperatures, simulation vs. experiment: (a) profile, and (b) melt pool size ($v = 506$ mm/s, $d = 0.65$ mm).

Similarly, from the experiments, 2 conditions with a close beam speed and a close beam current were investigated for the beam diameter effect. One condition (Condition 3) was from the SF36 case at 10.71 mm build height from this experiment, while the other (Condition 4) was from the SF36 case at 26.53 mm build height. The speed difference

between the two conditions was around 10%, the beam current was the same, 6.7 mA, while the beam diameters were approximately 0.65 mm and 0.55 mm, respectively. The experimental measurements show melt pool lengths as 1.89 mm for Condition 3 vs. 2.61 mm for Condition 4, showing also the importance of the beam diameter. The thermal model was utilized to quantify the beam diameter effect as well. The beam speed used was the average from the two conditions, 671 mm/sec, the beam current was 6.7 mA, and the beam diameters were 0.55 mm, 0.65 mm and 0.75 mm.

The simulated results are also shown in Figure 4.9, also compared with the experiment, also reasonably matched between the two. The results indicate that increasing the beam diameter will decrease the melt pool length, while slightly increasing the melt pool width, implying that the beam diameter effect is more dominant in the scanning direction. The increase of the melt pool width is due to the increase of the heat affected zone expanded from the beam size. Moreover, since powder materials are on both sides and ahead of the scan path, the heat resistance is much lower in the opposite direction of the scan path because of already solidified materials. Therefore, a slower cooling rate is expected along the melt pool width direction than the length direction, and thus, the melt pool width could increase while the length decreases under a given beam power and beam speed.

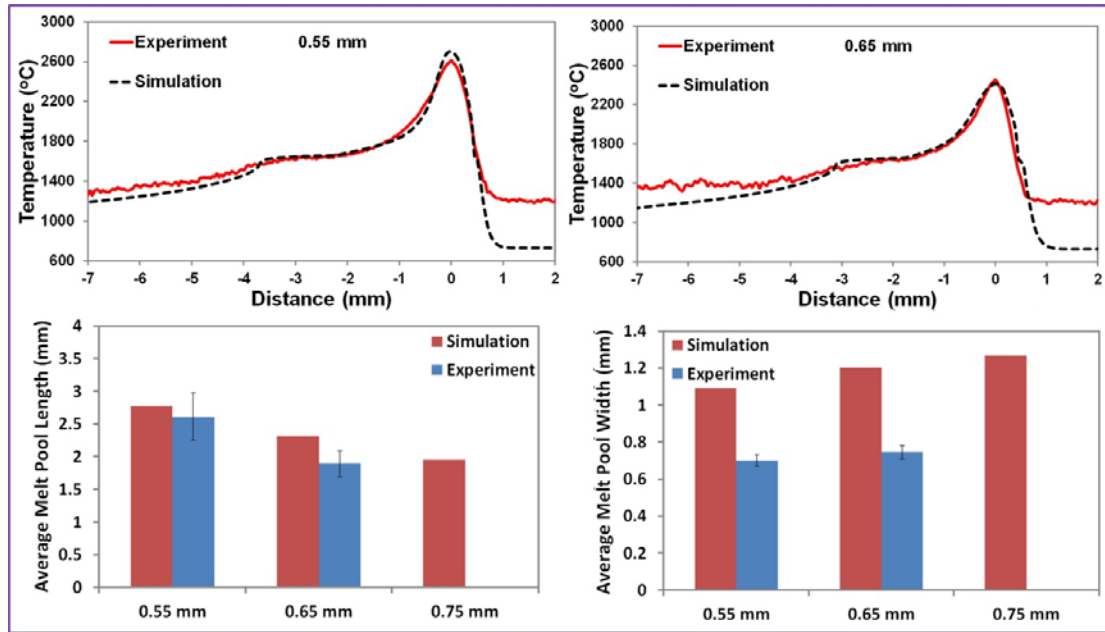


Figure 4.9. Beam diameter effects on EBAM process temperatures, simulation vs. experiment: (a) profile, and (b) melt pool size ($v=671$ mm/s, $i=6.7$ mA).

4.4 Conclusion

EBAM build part quality is very sensitive to the process thermal characteristics such as the melt pool size, correlated with the process parameters. In this study, the EBAM process was investigated with various levels of a process setting, speed function (SF) index that controls the beam speed and the beam current, which also change along the build height during the process. Process temperatures were measured and analyzed using the methodology developed by Price (Price, 2014), with the temperature profiles and the melt pool sizes evaluated. In addition, the EBAM parts built with different SF indices were examined in surface conditions and microstructures. The thermal model developed was further applied to predict the process temperatures using the parameters from the experiments. Moreover, the effects of the beam current as well as the beam diameter were investigated by both experiments and simulations. The major conclusions are summarized below.

1. SF setting strongly affects the EBAM part quality including surface morphology

and roughness. In general, a higher SF tends to produce parts of rougher surfaces with more pore features due to possibly insufficient melting/bonding, and higher cooling rate.

2. Increasing the beam speed will reduce the peak temperatures, also reduce the melt pool sizes. At a lower beam speed of 482 mm/s, the peak temperature and the melt pool length and width are 2572 °C, 2.35 mm and 0.93 mm, respectively. On the other hand, at a higher beam speed of 1595 mm/s, the peak temperature and the melt pool length and width are 2326 °C, 1.25 mm and 0.82 mm, respectively.

3. Simulations conducted to evaluate the beam speed effects are in reasonable agreement compared to the experimental measurements in temperatures and melt pools sizes. However, the results of a lower SF case, SF20, show larger differences between the simulations and the experiments, about 58% for the melt pool size.

4. The higher the beam current, the higher the peak process temperatures, also a larger melt pool: 1896 °C T_{\max} and 0.90 mm melt pool length for 2.5 mA vs. 2733 °C T_{\max} and 3.58 mm melt pool length for 7.7 mA. On the other hand, increasing the beam diameter monotonically decreases T_{\max} and the melt pool length: 2699 °C T_{\max} and 2.78 mm melt pool length for 0.55 mm diameter vs. 2250 °C T_{\max} and 1.95 mm melt pool length for 0.75 mm.

Acknowledgements

This research is supported by NSF (No. 1335481) and NASA (No. NNX11AM11A), and is in collaboration with Marshall Space Flight Center (Huntsville, AL), Advanced Manufacturing Team in Nonmetallic Branch.

References

Bontha, S., Klingbeil, N. W., Kobryn, P. A., & Fraser, H. L. (2009). Effects of process variables and size-scale on solidification microstructure in beam-based fabrication of

bulky 3D structures. *Materials Science and Engineering: A*, 513, 311-318.

Jamshidinia, M., Kong, F., & Kovacevic, R. (2013). Numerical modeling of heat distribution in the electron beam melting® of Ti-6Al-4V. *Journal of Manufacturing Science and Engineering*, 135(6), 061010.

Jurren, K.(ed)., *Workshop of Measurement Science Roadmap for Metal-Base Additive Manufacturing*, NIST, Gaithersburg, MD, December 2012.

Kumar, A., & Roy, S. (2009). Effect of three-dimensional melt pool convection on process characteristics during laser cladding. *Computational Materials Science*, 46(2), 495-506.

Mahale, T. R. (2009). *Electron beam melting of advanced materials and structures*. Ph.D. thesis, North Carolina State University, Raleigh, NC.

Price, S. (2014). *On temperature measurements and analysis in electron beam additive manufacturing using near infrared thermography*. Master thesis, The University of Alabama, Tuscaloosa, AL.

Song, Y.-A., & Koenig, W. (1997). Experimental study of the basic process mechanism for direct selective laser sintering of low-melting metallic powder. *CIRP Annals-Manufacturing Technology*, 46(1), 127-130.

Soylemez, E., Beuth, J. L., & Taminger, K. (2010). Controlling melt pool dimensions over a wide range of material deposition rates in electron beam additive manufacturing. *21st Annual International Solid Freeform Fabrication Symposium - An Additive Manufacturing Conference*, , Austin, TX, August 9-11, 2010, pp. 571-582.

Zäh, M. F., & Lutzmann, S. (2010). Modelling and simulation of electron beam melting. *Production Engineering. Research and Development*, 4, 15-23.

CHAPTER 5

MELT POOL EVOLUTION STUDY IN SELECTIVE LASER MELTING

Abstract

In selective laser melting (SLM) additive manufacturing, the completion of the entire scanning cross-sectional area of each layer build is consisted of many smaller scanning patches. Hence, the scanning length in each path may be too short to reach the melt pool quasi-steady state, thus, affecting the melt pool geometry, which is also effected by the process parameters. It is also known that the melt pool size correlates with the build part microstructures and properties. In this study, temperature simulations, finite-element based, of SLM for In718 is developed and validated against literature data. Then it was applied to track the thermal response during raster scanning of an individual patch. The results show that the process parameters determine the melt pool evolution, which affects the actual molten pool size in the regions defined by the raster scanning length. Manipulating the scanning path length and process parameters, based on the melt pool evolution information, may help to achieve a desired melt pool size for part quality controls.

5.1 Introduction

Powder-bed selective laser melting (SLM) is one of the additive manufacturing processes where metal parts are made directly from 3D CAD data without any special tooling in a layer by layer fashion. During the SLM process, a desired part is fabricated by selectively melting successive layers of powder materials using a high energy laser beam on a support

platform. The top powder layer is melted and forms moving liquid pool. Then, the melted material solidifies quickly and starts to form the desired shape. After the completion of the designed cross-section scan of a layer, the platform is lowered down by one layer thickness for new powder layer deposition. This deposition-scanning process is repeated until the whole part is finished building. The unused powder can be retrieved and reused in next build after the fabricating process. The whole building process is usually conducted in a chamber filled with inert gas (Thijs *et al.*, 2010). SLM technology has many advantages in comparison with other methods for manufacturing parts with complex geometry and inner structure. SLM is also capable of producing objects with mechanical properties comparable to those of bulk materials and to offer significant time savings by considerably reducing post-processing steps (Bourell *et al.*, 2002; Kruth *et al.*, 2007; Yadroitsev *et al.*, 2009).

SLM has been widely applied with commercial materials such as stainless steel (Wang and Felicelli, 2007) and iron (Kruth *et al.*, 2004). Among all the materials, Inconel718 is a niobium-modified nickel-base super-alloy which has been widely used in aeronautic, astronautic and nuclear industries for its good strength, excellent resistance to oxidation at high temperatures, and favorable weldability (Zhao *et al.*, 2008). It is widely used to fabricate parts used in critical environments because it has high strength up to 923 K, as well as good corrosion resistance and creep resistance (Liu *et al.*, 2002). While complex structures, such as internal channel, are difficult to make by traditional methods such as casting and machining, SLM is a promising alternative method.

Despite many potential advantages over conventional manufacturing technologies, SLM still encounters several part and process defects due to high energy input such as rough

surface finish and severe deformation. In the building process, some of the SLM systems utilize a patch scanning strategy, which may be able to reduce local stress. The completion of the entire scanning cross-sectional area of each layer consists of many smaller scanning patches, as shown in Figure 5.1. The system randomly picked the patches to do hatch scanning and the scanning direction is different for adjacent patches, e.g., rotated by 90 degree between neighboring patches. The melt pool will reach quasi-steady state after beam travels certain distance that its geometry will keep unchanged in the following scanning. Hence, the scanning length in each path may be too short to reach the quasi-steady state, thus, affecting the melt pool geometry, which is also effected by the process parameters. It is also known that the melt pool size correlates with the build part microstructures and properties. In addition, the solidified material remelting phenomenon caused by melt pool geometry may also be quite influential to part quality such as porosity reduction (Gong *et al.*, 2014) and minimization of macro-segregation defect (Van Den Avyle *et al.*, 1998). However, excessive remelting may deteriorate part surface quality (Guo *et al.*, 2014).

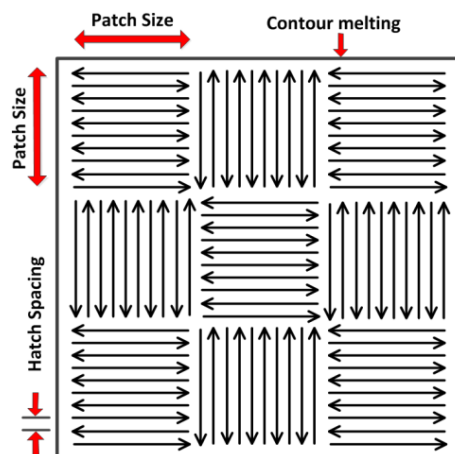


Figure 5.1. Patch scanning strategy.

Therefore, physics-based modeling of SLM process phenomena is required to investigate process characteristics such as melt pool sizes and temperature fields. Thermal

models have been widely investigated in powder bed metal additive manufacturing studies. Song et al (Song *et al.*, 2012) has reported a 3D SLM model to simulate the temperature distribution with a surface Gaussian heat source. Dong et al (Dong *et al.*, 2009) developed a finite element model of polycarbonate material to study the phase transformation during the selective laser sintering (SLS) process. The process parameters effects on temperature have been investigated. Xing et al (Xing *et al.*, 2013) developed a SLS 3D model for Al₂O₃ coated ceramic powder to simulate the transient temperature. Experiment with high-speed CCD temperature collection was used for model validation. Yuan and Gu (Yuan and Gu, 2015) established a 3D finite volume method (FVM) model to investigate the temperature evolution behaviour and fluid flow effect in melt pool during SLM process of TiC/AlSi10Mg material. Zeng et al (Zeng *et al.*, 2012) have presented a comprehensive literature review of SLM/SLS thermal analysis. Information about SLM analytical solution, numerical modeling works, temperature measurements and examples of simulation results has been detailed. However, the modeling studies of the SLM process for In718 material have been relatively rare. Schilp et al (Schilp *et al.*, 2014) presented both microscale and macroscale models to study the temperature distribution in a laser beam melting of In718. The temperature distribution and its temporal evolution can be investigated by the developed model. Romano et al (Romano *et al.*, 2016) developed and validated a finite element thermal model for In718 in a selective laser beam scanning and melting process.

In this study, a finite element model incorporating Gaussian heat flux distribution and raster scan strategy was developed to study the melt pool evolution phenomenon in one scanning patch. The model can be utilized to track the thermal characteristics under given

process parameters and raster length. The objective of this task is to have fundamental understanding of the In718 SLM thermal characteristics such as temperature distributions and melt pool sizes for its widespread applications.

5.2 Selective Laser Melting Model Construction

5.2.1 Governing Equation

In the SLM process, a laser beam travels along raster pattern on the surface of the powder layer at a constant speed. The instantaneous temperature distribution satisfies the following 3D heat transport conduction equation:

$$\nabla \left(\frac{k}{\rho c} \nabla T \right) + \frac{\dot{Q}}{\rho c} = \frac{\partial T}{\partial t} + v \frac{\partial T}{\partial x}, \quad (5)$$

where T is temperature, \dot{Q} is the absorbed heat flux, c is specific heat capacity, ρ is density, k is thermal conductivity, v is the constant scanning speed.

In order to improve the numerical modeling accuracy, the latent heat of fusion, L_f , was also considered in this study. It was implemented as an additional term of the internal thermal energy per unit mass, when the temperature is between the solidus and liquidus temperature. The enthalpy, $H(T)$, can be defined as follows:

$$H(T) = \int c dT + L_f f, \quad (6)$$

where f is the volumetric fraction of the liquid:

$$f = \begin{cases} 0 & T < T_s, \\ \frac{T - T_s}{T_L - T_s} & T_s \leq T \leq T_L, \\ 1 & T > T_L \end{cases} \quad (7)$$

5.2.2 Heat Input Equation

A thermal mathematical model with high accuracy is critical to simulate the input laser heat source in SLM scanning process. In this study, the laser beam heat input

distribution is modeled as a 2D conical moving heat source with a Gaussian distribution and linearly decaying along the beam penetrating direction, which is modified from the heat source equation in Chapter 3:

$$\dot{Q}_{(x,y,z)} = \eta \times \frac{H_s \times I_z}{S} \quad (8)$$

with

$$I_z = \frac{1}{0.75} \left(-2.25 \left(\frac{z}{S} \right)^2 + 1.5 \left(\frac{z}{S} \right) + 0.75 \right),$$

$$H_s = \frac{2P}{\pi \Phi_E^2} \exp \left\{ -\frac{2[(x-x_s)^2 + (y-y_s)^2]}{\Phi_E^2} \right\}.$$

Where the parameters include Gaussian heat source: H_s , the linearly decaying function: I_z , laser beam efficiency coefficient: η , laser power: P , penetration depth: S , beam diameter: Φ_E , and the instantaneous horizontal position of the heat source center: x_s and y_s . User subroutine, DFLUX, is programmed to incorporate incident heat flux in the simulation process.

5.2.3 Material Property Modeling

Temperature dependent material properties were incorporated in the numerical study since a wide range of temperature should be expected during high energy laser melting process. Temperature dependent properties such as density, specific heat and conductivity of solid In718 alloy have been reported in literature (Dye *et al.*, 2001), and summarized in Figure 5.2. The increase of thermal conductivity after melting point is used to simulate the heat convection of melt pool (Liu *et al.*, 2010).

Since the incident laser beam heat source is directly applied in the top powder layer of scanned region, it is critical to take into account of the powder property in the calculation

process due to significant difference of thermal properties between powder and solid bulk material. The latent heat of fusion and specific heat of powder may be considered the same as those of the solid material (Lin *et al.*, 1985; Tolochko *et al.*, 2003; Kolossov *et al.*, 2004; Sih and Barlow, 2004; Patil and Yadava, 2007; Roberts *et al.*, 2009; Zäh and Lutzmann, 2010). Moreover, the powder material may have the same properties of solid bulk material after being melted. The density of the powder material can be calculated through a function of the local powder density and the solid material density (Sun *et al.*, 2015):

$$\Phi = \frac{\rho_{bulk} - \rho_{powder}}{\rho_{bulk}} \quad (9)$$

where Φ is the powder porosity; ρ_{bulk} and ρ_{powder} are the solid and powder densities, respectively.

There are studies of the thermal conductivity of powder in recent years, including both theoretical and experimental methods. Tolochko et al. (Tolochko *et al.*, 2003) developed a thermal conductivity model for Ti powder in a study of SLS process. The effective powder thermal conductivities due to radiation and powder particle necks have been considered in the model. In this study, the powder thermal conductivity is considered according to the ratio of Ti-6Al-4V solid and powder conductivity value from Chapter 3, as shown in Figure 5.2. Material state change, e.g., powder to solid, is also considered and programmed in user subroutine UMATHT. The state change criterion is that powder material is melted and under cooling.

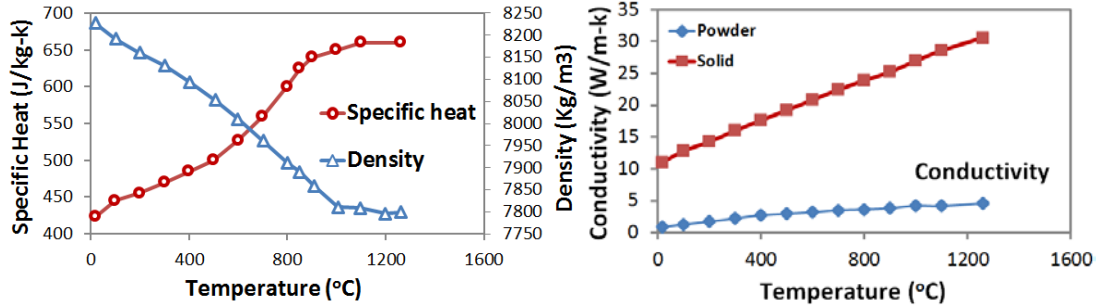


Figure 5.2. In718 solid (Dye *et al.*, 2001) and powder thermal properties.

5.2.4 Model Configuration

A 3D finite element method (FEM) thermal model was developed to investigate the thermal process of SLM by commercial software ABAQUS. Raster scan path was simulated in this model, thus the previous deposited material was modeled as solid. The newly deposited powder layer on the top surface of deposited material was considered and has the powder thermal properties. The beam heating starts at the top powder surface and travels along the designed raster path with a constant speed. The initial condition for the whole computational domain has been set to be a uniform temperature of $T_{initial}$. The thermal boundary conditions for heat losses due to surface convection and radiation on the top surface have also been considered in the model. The 3D simulation model is presented in Figure 5.3. The solid substrate for the model was a block of In718 bulk material with dimensions of 6 mm × 6 mm × 10.7 mm in (x, y, z) direction. Considering the calculation efficiency and computational precision, heat transfer elements (DC3D8) elements with a fine mesh of 0.025 mm × 0.02625 mm × 0.01 mm ($x \times y \times z$), were used to represent the raster scanning region, while a relatively coarse mesh was adopted for the substrate. The highlighted region in Figure 5.3 is the designed scanning region. The specific raster scan type is programmed in user subroutine “DFLUX” by defining the heat source center location moving along the raster

path as a function of time. Detailed process modeling and simulation parameters are listed in

Table 5.1

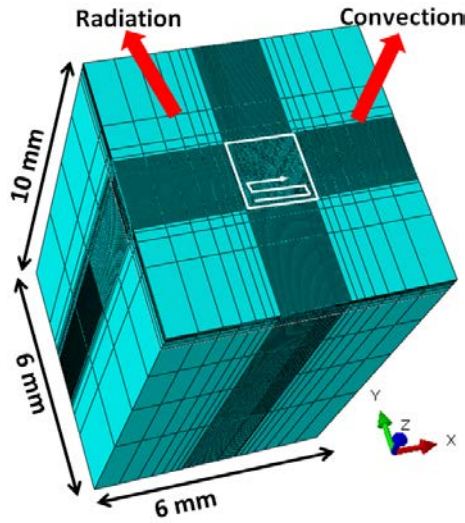


Figure 5.3. An example of 3D FEM model for multi-path scanning with fine mesh.

Table 5.1. Parameter list used in simulations for In718.

Parameters	Values
Solidus temperature, T_S (°C)	1260 (Arafin et al., 2007)
Liquidus temperature, T_L (°C)	1336 (Arafin et al., 2007)
Latent heat of fusion, L_f (kJ/Kg)	227 (Kamnis et al., 2008)
Electron beam diameter, Φ (mm)	0.15
Absorption efficiency, η	0.64 (Tolochko <i>et al.</i> , 2000)
Scan speed, v (mm/sec)	1000
Beam power, P (W)	450
Powder layer thickness, t_{layer} (mm)	0.03
Porosity, ϕ	0.5
Beam penetration depth, d_p (mm)	0.02 (Fischer <i>et al.</i> , 2002)
Thermal initial condition, T_{initial} (°C)	20
Emissivity, ϵ	0.3 (Lundbäck et al.)

5.3 Results and Discussion

5.3.1 Model Validation

Due to lack of available experimental data for In718 in this study, the studies of SLM process for In718 material by Lee and Zhang (Lee and Zhang, 2016) were used for model validation and calibration purposes. The process conditions in their actual experimental study have been incorporated in the developed SLM model. The results have been concluded in Figure 5.4 and Table 5.2. The comparison showed a max error of 5.55% for melt pool depth; while the max error for width is 11.11 %. To test the robustness of the model, SLM experimental results with Ti64 material and different process parameters from Verhaeghe et al (Verhaeghe *et al.*, 2009) have been checked. The SLM building process has been duplicated in the model with necessary simulation parameters. The simulation results and literature experiment results have been concluded in Figure 5.5. The simulated values have reasonable agreement with experimental data. The max error for melt pool depth is 18.6% and the average error is 10.4%; while the max error for melt pool width is 32% and the average error is 17.5%. The reasonable agreement with experiments showed the model could be utilized to do thermal analysis of laser hatch melting process under different process parameters.

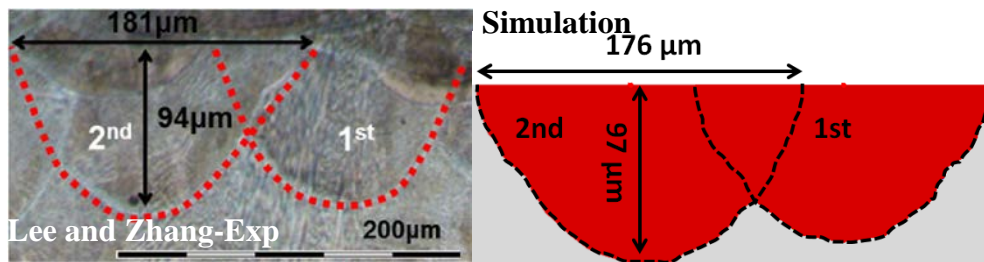


Figure 5.4. Comparison between SLM simulation and literature data for In718.

Table 5.2. Simulation and experiment comparison.

Track no.	Melt pool	Exp (μm) (Lee and Zhang, 2016)	Simulation	Error (%)
1	Width	144	160	11.11
	Depth	90	85	5.55
2	Width	181	176	2.76
	Depth	94	97	3.19
1–2	Overlap	63	56.8	9.84

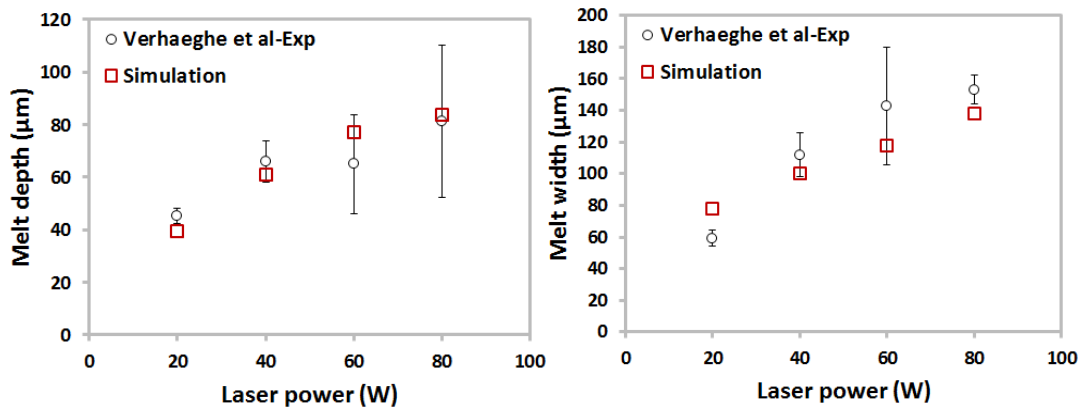


Figure 5.5. Comparison between SLM simulation and literature data for Ti64.

5.3.2 Typical Example of Simulated Results

Simulations have been conducted by moving the laser beam along raster pattern. The single patch raster scan may contribute to understand temperature distribution of a single layer. The raster patch consisted of 10 straight paths with length=1 mm, they have been connected by raster turning arms with length=105 μm (hatch spacing). An initial calculation was run with 0.15 mm beam diameter, 1000 mm/s scanning speed and 450 W laser power. The temperature distribution, at different scanning time, on the top powder layer is shown in Figure 5.6, where the geometry of the melt pool is plotted with the threshold value of the liquidus point of In718 with white color. The temperature evolution clearly shows the moving melt pool is followed by the just solidified material with decreasing temperature, as shown in Figure 5.6 (a). Melt pool temperature starts to increase again when the laser beam reaches the turning point of the raster path and travels along the short raster connection arm. It is noted the melt pool max temperature has increased from 2712 to 2905 $^{\circ}\text{C}$ in Figure 5.6 (b). Then,

the laser beam travels along the second straight raster path. At this point, partial solidified material in the first scanning path may start to be remelted because the input laser power is affected by previous residual heat that has not fully dissipated to substrate solid material. The melt pool max temperature is still higher than that of the first scanning path. In addition, the melt pool size is increased by residual heat effect, as shown in Figure 5.6 (c). Moreover, Figure 5.6 (d) indicates that when the laser beam continues to travel, the melt pool size and max temperature may decrease due to the fact that residual heat effect of first scanning path reduces with time increases.

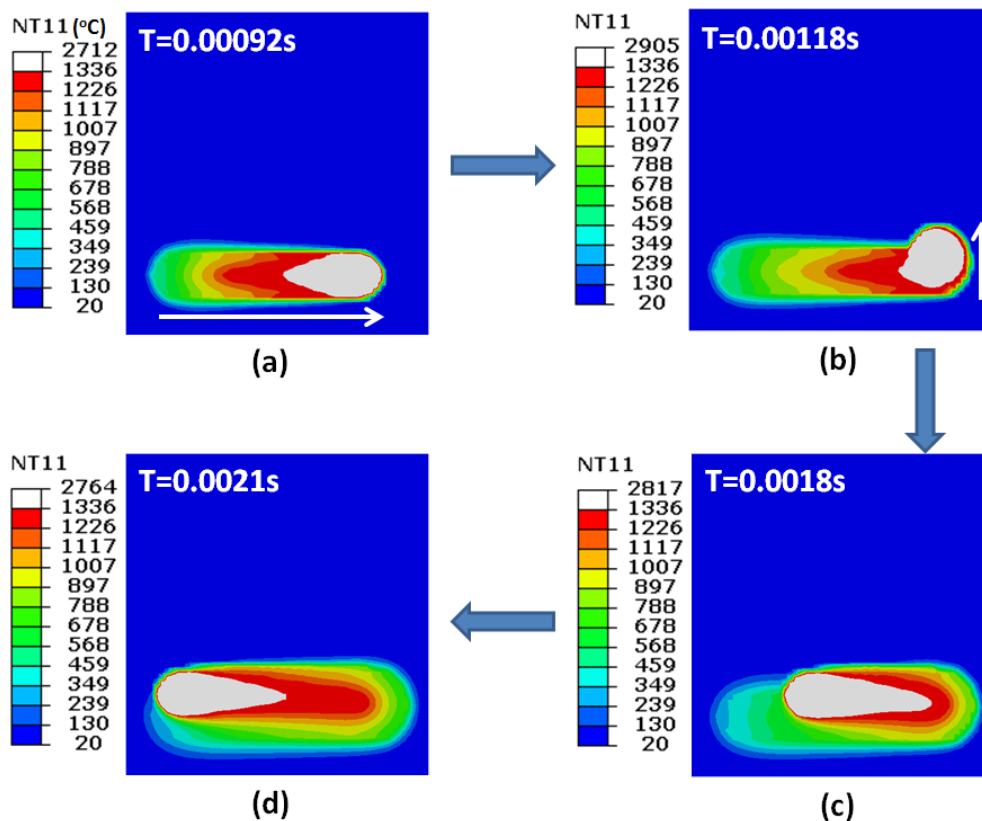


Figure 5.6. Example of temperature and melt pool evolution in raster scan.

Further observations have indicated that the residual heat would further increase the melt pool size when laser beam travels on the subsequent scanning paths. For example, it has been noticed that the main heat penetrated depth (melt pool depth) varies from ~ 0.085 mm to

~0.11 mm. When the laser beam passes certain raster path, e.g., path-7, the residual heat effect may come to a balance and the max melt pool size will not further increase, as shown in Figure 5.7 (a). Figure 5.7 (b) illustrates the melt pool shape when the laser beam travels along different raster paths. It can be noted when the beam is travelling along path-1 the melt pool is symmetric to the path centerline. However, when the laser beam travels along path-5, the melt pool is not symmetric; a larger half of melt pool area is shown on the residual heat effect region.

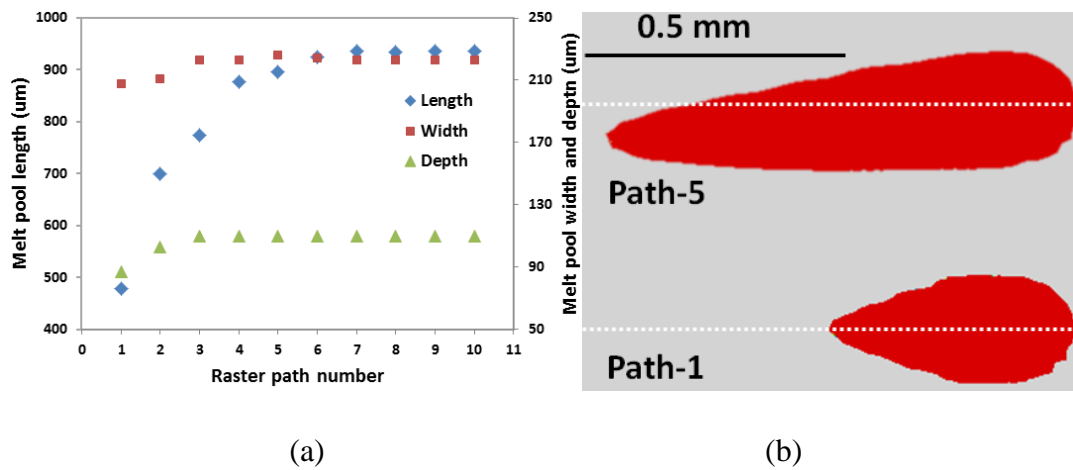


Figure 5.7. (a) Max melt pool size in different raster path, (b) melt pool shape.

5.3.3 Raster Length Effect on Melt Pool Evolution

The melt pool evolution process information in single track scanning has been collected and summarized in Figure 5.8. It is observed that melt pool will start to form after beam energy has been initialized. Melt pool sizes will continue to increase until reach steady state. It is also noted that the melt pool depth and width will reach steady state ahead of length. The melt pool length will get fully developed at around 0.6 mm under current given process parameters. If laser beam travels in a smaller path region, the scanning length in each path may be too short to reach the quasi-steady state, thus, affecting the melt pool geometry.

Therefore, A smaller raster length case, length=0.5 mm has been conducted to evaluate the raster length effect on melt pool geometry. The raster region consisted of 5 straight paths due to the reduction of scanning length. The residual heat effect is expected to be more serious since a smaller region reduces the heat dissipating time. The incident heat input region will overlap with the residual heat region thus increase the possibility of forming larger remelting zone. Figure 5.9 shows the melt pool shapes at raster path 1, 3, 5 for different raster length cases. The melt pool length of the L=0.5 mm case is smaller than that of L=1 mm due to the restriction of shorter scanning track. However, the width of lower half of the melt pool increases significant due to residual heat effect after laser beam scanned several paths, e.g., melt pool in path 5, as shown in Figure 5.9 for L=0.5 mm case.

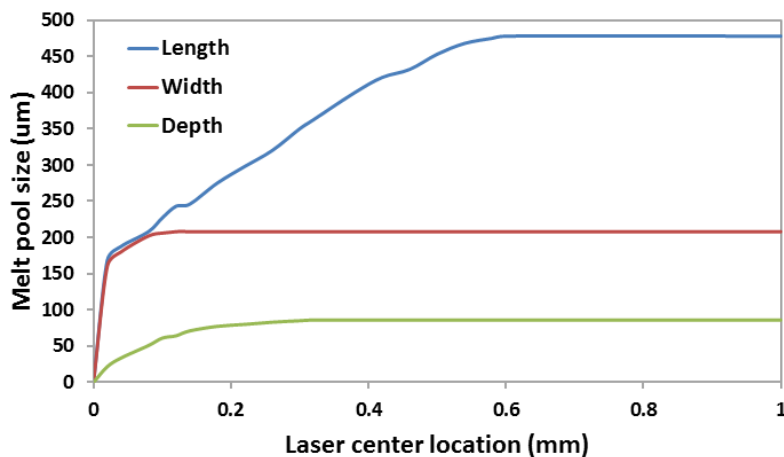


Figure 5.8. Melt pool evolution in a single track.

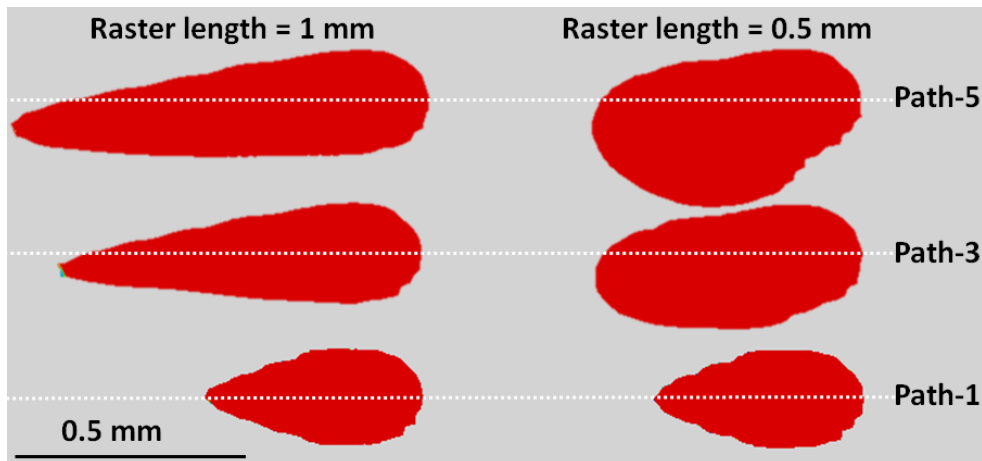


Figure 5.9. Melt pool size in different scanning path.

5.3.4 Process Parameters Effect

It is well known that different parameters may affect melt pool geometry, cooling rate, grain growths, residual stresses and deformation, and may also play a critical role in part microstructure as well as hardness and elastic properties. Therefore, it is necessary to investigate their effects on raster scan. Figure 5.10 shows the melt pool length evolution process for different process parameters simulation results. The results have displayed interesting characteristics for tested process parameter sets: (a) higher beam power as well as slower beam speed cases may need longer scanning length to reach melt pool steady state, e.g., case (3), (4) vs. case (1); (b) a smaller beam diameter may reduce the scanning length needed for melt pool fully development, e.g., case (2) vs. case (1). Thus, the interesting phenomenon may also greatly affect the melt pool evolution in raster scanning. It is observed that, for case (1) and (2) in Figure 5.11 (a) and (b), the raster length may have minor effect on melt pool geometry since the melt pool needs a distance close to or shorter than 0.5 mm to get steady state. Thus the residual heat may have small effect on succeeding melt pool evolution. For case (3) and (4) in Figure 5.11 (c) and (d), the necessary length for melt pool fully development is larger than 0.5 mm. Therefore the residual heat effect on melt pool geometry can not be ignored, it is noted that the accumulated residual heat has noticeably expanded the melt pool width. The observed melt pool shape changes from comet-like to more ellipse-like, especially for the lower half of the melt pool.

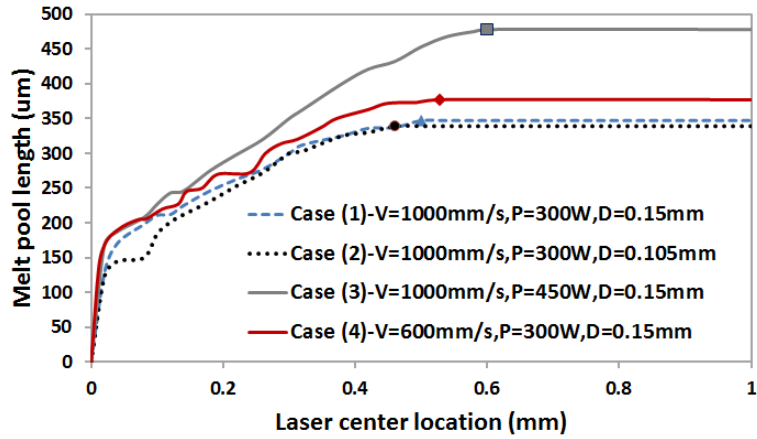


Figure 5.10. Melt pool length evolution vs. different process parameters.

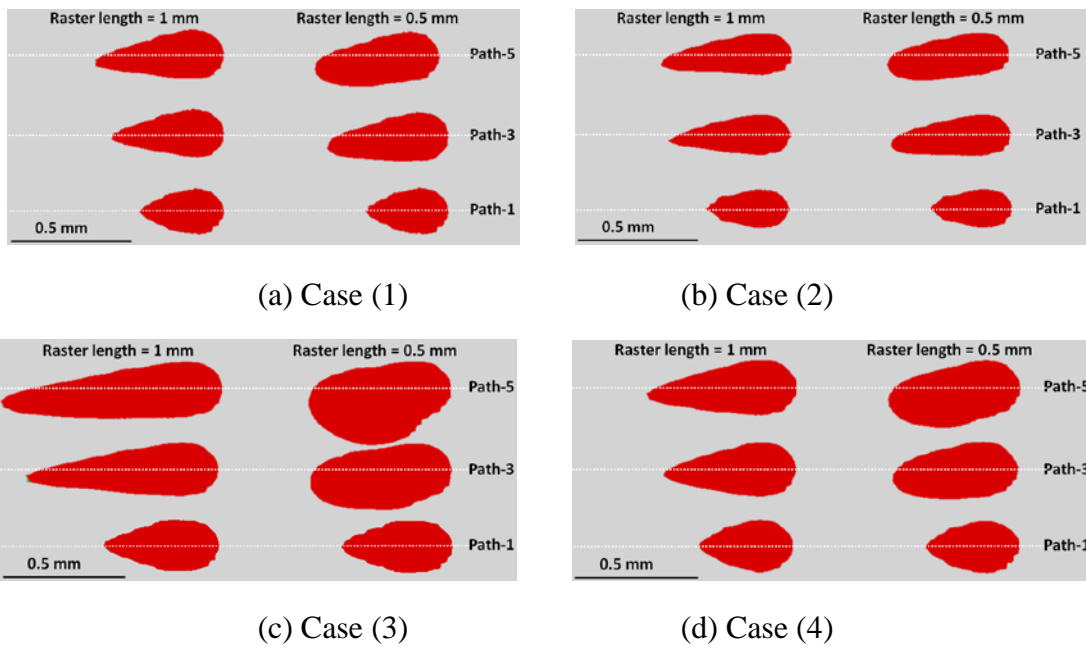


Figure 5.11. Raster length effect on different process parameters cases.

5.4 Conclusion

This study focuses on the development of a numerical thermal model for In718 SLM process. A 3D thermal model, using finite element method, was developed for SLM process thermal behavior simulations under different patch scanning conditions. The model incorporated a moving heat source with a Gaussian volumetric intensity, In718 powder as well as solid material temperature-dependent properties and raster scan strategy, etc. The major findings can be summarized as follows.

1. The residual heat will significantly affect the melt pool size during raster scan; the melt pool will continue to increase during the raster scanning process, e.g, melt pool depth changes from ~0.085 mm to ~0.115 mm under given parameters. However, the residual heat effect may reach a steady state and the max melt pool size keeps the same after beam passes certain raster path, e.g., path 7 in this study for V=1000 mm/s, P=450 W, D=0.15 mm case.

2. Process parameters will significantly affect melt pool development, a larger beam power and slower beam speed could increase the traveling distance for a full evolution while a smaller beam diameter may reduce this distance for tested process parameters.

3. In the regions defined by the raster scanning length, a longer melt pool evolution distance may have a more significant residual heat effect on the melt pool geometry on the subsequent raster scanning path.

Acknowledgements

This research is supported by NASA, No. NNX11AM11A. The first author acknowledges the scholarship support from the Alabama EPSCoR Graduate Research Scholars Program.

References

- Arafin, M., Medraj, M., Turner, D., & Bocher, P. (2007). Transient liquid phase bonding of Inconel 718 and Inconel 625 with BNi-2: Modeling and experimental investigations. *Materials Science and Engineering: A*, 447(1), 125-133.
- Bourell, D., Wohlert, M., Harlan, N., Das, S., & Beaman, J. (2002). Powder densification maps in selective laser sintering. *Advanced Engineering Materials*, 4(9), 663-669.
- Dong, L., Makradi, A., Ahzi, S., & Remond, Y. (2009). Three-dimensional transient finite element analysis of the selective laser sintering process. *Journal of materials processing technology*, 209(2), 700-706.
- Dye, D., Hunziker, O., Roberts, S., & Reed, R. (2001). Modeling of the mechanical effects

- induced by the tungsten inert-gas welding of the IN718 superalloy. *Metallurgical and Materials Transactions A*, 32(7), 1713-1725.
- Fischer, P., Karapatis, N., Romano, V., Glardon, R., & Weber, H. (2002). A model for the interaction of near-infrared laser pulses with metal powders in selective laser sintering. *Applied physics A*, 74(4), 467-474.
- Gong, H., Rafi, K., Gu, H., Starr, T., & Stucker, B. (2014). Analysis of defect generation in Ti-6Al-4V parts made using powder bed fusion additive manufacturing processes. *Additive Manufacturing*, 1, 87-98.
- Guo, C., Ge, W., & Lin, F. (2014). Material Molten Time and its Effect on Material Deposition during Electron Beam Selective Melting. 25th Annual International Solid Freeform Fabrication Symposium - An Additive Manufacturing Conference, Austin, TX, USA, August 4-6, 2014.
- Hussein, A., Hao, L., Yan, C., & Everson, R. (2013). Finite element simulation of the temperature and stress fields in single layers built without-support in selective laser melting. *Materials & Design*, 52, 638-647.
- Kamnis, S., Gu, S., & Zeoli, N. (2008). Mathematical modelling of Inconel 718 particles in HVOF thermal spraying. *Surface and Coatings Technology*, 202(12), 2715-2724.
- Kolossov, S., Boillat, E., Glardon, R., Fischer, P., & Locher, M. (2004). 3D FE simulation for temperature evolution in the selective laser sintering process. *International Journal of Machine Tools and Manufacture*, 44(2-3), 117-123. doi:10.1016/j.ijmachtools.2003.10.019
- Kruth, J.-P., Froyen, L., Van Vaerenbergh, J., Mercelis, P., Rombouts, M., & Lauwers, B. (2004). Selective laser melting of iron-based powder. *Journal of Materials Processing Technology*, 149(1), 616-622.
- Kruth, J.-P., Levy, G., Klocke, F., & Childs, T. (2007). Consolidation phenomena in laser and powder-bed based layered manufacturing. *CIRP Annals-Manufacturing Technology*, 56(2), 730-759.
- Lee, Y., & Zhang, W. (2016). Modeling of heat transfer, fluid flow and solidification microstructure of nickel-base superalloy fabricated by laser powder bed fusion. *Additive Manufacturing*. In Press
- Lin, T. H., Watson, J. S., & Fisher, P. W. (1985). Thermal conductivity of iron-titanium powders. *Journal of Chemical & Engineering Data*, 30(4), 369-372.
- Liu, C., Wu, B., & Zhang, J. (2010). Numerical Investigation of Residual Stress in Thick

- Titanium Alloy Plate Joined with Electron Beam Welding. *Metallurgical and Materials Transactions B*, 41(5), 1129-1138.
- Liu, L., Hirose, A., & Kobayashi, K. F. (2002). A numerical approach for predicting laser surface annealing process of Inconel 718. *Acta materialia*, 50(6), 1331-1347.
- Lundbäck, A., Alberg, H., & Henrikson, P. Simulation and validation of TIG welding and post weld heat treatment of an Inconel 718 plate. *Mathematical Modelling of Weld Phenomena 7*, 683-696.
- Patil, R. B., & Yadava, V. (2007). Finite element analysis of temperature distribution in single metallic powder layer during metal laser sintering. *International Journal of Machine Tools and Manufacture*, 47(7-8), 1069-1080.
- Roberts, I. A., Wang, C. J., Esterlein, R., Stanford, M., & Mynors, D. J. (2009). A three-dimensional finite element analysis of the temperature field during laser melting of metal powders in additive layer manufacturing. *International Journal of Machine Tools and Manufacture*, 49(12-13), 916-923.
- Romano, J., Ladani, L., & Sadowski, M. (2016). Laser Additive Melting and Solidification of Inconel 718: Finite Element Simulation and Experiment. *JOM*, 1-11.
- Schilp, J., Seidel, C., Krauss, H., & Weirather, J. (2014). Investigations on Temperature Fields during Laser Beam Melting by Means of Process Monitoring and Multiscale Process Modelling. *Advances in Mechanical Engineering*, 2014, 7.
- Sih, S. S., & Barlow, J. W. (2004). The prediction of the emissivity and thermal conductivity of powder beds. *Particulate Science and Technology*, 22, 291-304.
- Song, B., Dong, S., Liao, H., & Coddet, C. (2012). Process parameter selection for selective laser melting of Ti6Al4V based on temperature distribution simulation and experimental sintering. *The International Journal of Advanced Manufacturing Technology*, 61(9-12), 967-974.
- Sun, S., Zheng, L., Liu, Y., Liu, J., & Zhang, H. (2015). Selective laser melting of Al-Fe-V-Si heat-resistant aluminum alloy powder: modeling and experiments. *The International Journal of Advanced Manufacturing Technology*, 1-11.
- Thijs, L., Verhaeghe, F., Craeghs, T., Van Humbeeck, J., & Kruth, J.-P. (2010). A study of the microstructural evolution during selective laser melting of Ti-6Al-4V. *Acta Materialia*, 58(9), 3303-3312.
- Tolochko, N. K., Arshinov, M. K., Gusarov, A. V., Titov, V. I., Laoui, T., & Froyen, L. (2003). Mechanisms of selective laser sintering and heat transfer in Ti powder. *Rapid Prototyping Journal*, 9, 314-326.

- Tolochko, N. K., Khlopkov, Y. V., Mozzharov, S. E., Ignatiev, M. B., Laoui, T., & Titov, V. I. (2000). Absorptance of powder materials suitable for laser sintering. *Rapid Prototyping Journal*, 6(3), 155-161.
- Van Den Avyle, J. A., Brooks, J. A., & Powell, A. C. (1998). Reducing defects in remelting processes for high-performance alloys. *JOM*, 50(3), 22-25.
- Verhaeghe, F., Craeghs, T., Heulens, J., & Pandelaers, L. (2009). A pragmatic model for selective laser melting with evaporation. *Acta Materialia*, 57(20), 6006-6012.
- Wang, L., & Felicelli, S. (2007). Process modeling in laser deposition of multilayer SS410 steel. *Journal of Manufacturing Science and Engineering*, 129(6), 1028-1034.
- Xing, J., Sun, W., Rana, R., & IEEE, S. M. (2013). 3D modeling and testing of transient temperature in selective laser sintering (SLS) process. *Optik-International Journal for Light and Electron Optics*, 124(4), 301-304.
- Yadroitsev, I., Shishkovsky, I., Bertrand, P., & Smurov, I. (2009). Manufacturing of fine-structured 3D porous filter elements by selective laser melting. *Applied Surface Science*, 255(10), 5523-5527.
- Yuan, P., & Gu, D. (2015). Molten pool behaviour and its physical mechanism during selective laser melting of TiC/AlSi10Mg nanocomposites: simulation and experiments. *Journal of Physics D: Applied Physics*, 48(3), 035303.
- Zeng, K., Pal, D., & Stucker, B. (2012). A review of thermal analysis methods in Laser Sintering and Selective Laser Melting. Paper presented at the 23rd Annual International Solid Freeform Fabrication Symposium - An Additive Manufacturing Conference,, Austin, TX, USA, August 6-8, 2012.
- Zhao, X., Chen, J., Lin, X., & Huang, W. (2008). Study on microstructure and mechanical properties of laser rapid forming Inconel 718. *Materials Science and Engineering: A*, 478(1), 119-124.
- Zäh, M. F., & Lutzmann, S. (2010). Modelling and simulation of electron beam melting. *Production Engineering. Research and Development*, 4, 15-23.

CHAPTER 6

THERMOMECHANICAL INVESTIGATION OF POWDER SINTERING EFFECT FOR OVERHANG FABRICATIONS IN ELECTRON BEAM ADDITIVE MANUFACTURING

Abstract

Electron beam additive manufacturing (EBAM) is one of powder-bed-fusion additive manufacturing processes that are capable of making full density metallic components. EBAM has a great potential in various high-value, small-batch productions in biomedical and aerospace industries. In EBAM, because a build part is immersed in the powder bed, ideally the process would not require support structures for overhang geometry. However, in practice, support structures are indeed needed for an overhang; without it, the overhang area will have defects such as warping, which is due to the complex thermomechanical process in EBAM. In this study, a thermomechanical finite element model has been developed to simulate temperature and stress fields when building a simple overhang in order to examine the root cause of overhang warping. Two cases with different sintering conditions (preheating and powder porosity) have been studied. It is found that the poor thermal conductivity of Ti-6Al-4V powder results in higher temperatures, also slower heat dissipation, in an overhang area, in EBAM builds. The retained high temperatures in the area above the powder substrate result in large final deflection in an overhang area. Lower powder porosity, created by higher preheating temperature, could contribute higher conductivity, which may reduce the process temperature and deformation associated with building an overhang.

6.1 Introduction

Additive manufacturing (AM) is a group of technologies that physical parts are built directly from model geometric digital information in a layer-by-layer fabrication method. Powder-based electron beam additive manufacturing (EBAM) utilizes high-energy sources to fabricate metallic parts by iteratively sintering and/or melting metal powders in computer defined layered cross-sectional region. EBAM received increasing applications in many industrial areas such as aerospace, aeronautics and medical fields due to process flexibility, full-density and complex internal features. The use of high energy heat source enables EBAM process to deal with a wide range of metals including copper (Ramirez *et al.*, 2011), tool steels (Cormier *et al.*, 2004), Ti-6Al-4V and nickel alloys (Murr *et al.*, 2011).

Despite extensive advantages over conventional technologies, EBAM has emerged as a cost-effective alternative innovative technology for high-value, small-batch, and custom-designed metal components. The inevitable overhang geometries in part design may cause serious part distortion in EBAM process. Due to the fact that the cantilever portion of overhang structure is built upon powder bed, which has a much smaller conductivity compared to solid, thus the inefficient heat dissipation ability could happen around overhang region. The accumulated deformation of build layers in overhang region caused by heat dissipation deficiency and repeated thermal cycles in layered process would lead to final part failure. Thus extra constraint to prevent part warping is needed such as lattice and honeycomb support beneath overhang layers. However, post-processing of support removal can be a high-cost, labor-intense and time-consuming job. Moreover, damage to the support contact surface could be introduced during the removal process. A traditional support has

been shown in Figure 6.1 (Mumtaz *et al.*, 2011) for overhang part; mechanical tools may be required to remove these supports.

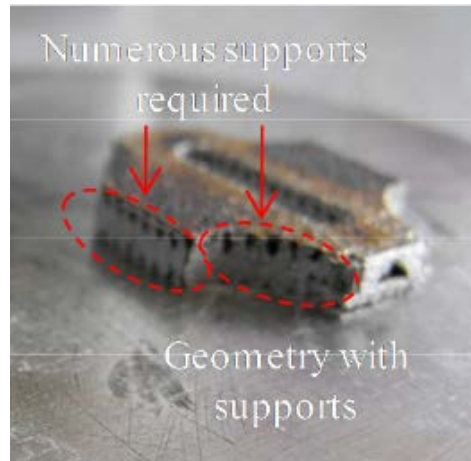


Figure 6.1. Required support structures in SLM process (Mumtaz *et al.*, 2011).

Mumtaz *et al.* (Mumtaz *et al.*, 2011) developed anchorless SLM method which was a novel technique aimed at reducing residual stress in powder bed additive manufacturing process. Vora *et al.* (Vora *et al.*, 2013) utilized this method both in SLM and EBAM process and successfully reduced the overhang deformation. Generally speaking, this method would keep the materials remained in liquid-solid mushy state until the part was built completely and allowed to cool down. Minimum residual stress and deformation may be induced by using this method, as shown in Figure 6.2 (Mumtaz *et al.*, 2011; Vora *et al.*, 2013). Their method has actually proposed a way for support structure free design which may help to reduce both part warping and post process material removal labor works. However, one of the existing problems in their method is that the powder particles needed are mixed with other materials. The mix of other materials may cause variations in build part mechanical properties and microstructures which may cause potential problems under specific

requirements for industrial usage, especially for those applications which may require “pure” materials.

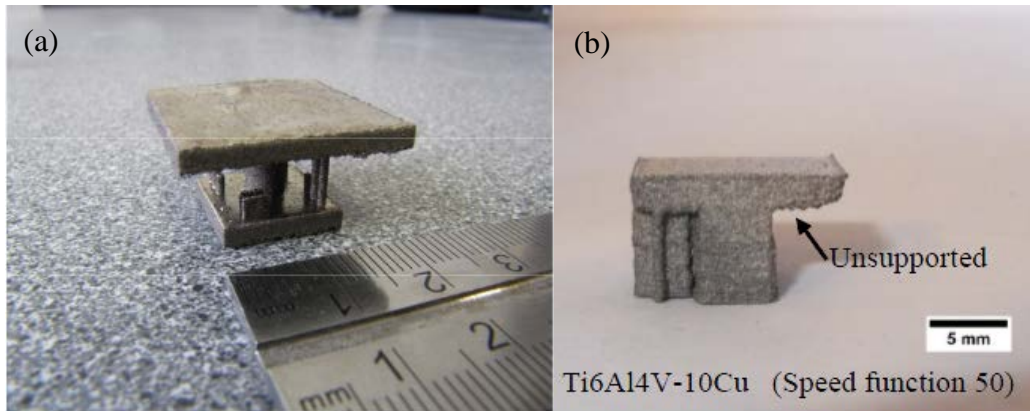


Figure 6.2. (a) Anchorless Bi₃Zn SLM part (Mumtaz *et al.*, 2011); (b) Ti6Al4V-10Cu EBAM part (Vora *et al.*, 2013).

Based on the assumption that the inefficient heat dissipation ability of powder bed contributed to the overhang deformation, a practical method that may improve the powder conductivity could help to reduce overhang deformation without support structure implement and mixture of materials is necessary. In EBAM process, a preheating step is conducted before hatch melting for a newly deposited powder layer. The preheating is achieved by using multi-pass electron beam scan at a high speed to reach a high temperature for the deposited powder-bed surface. The preheated powder particles will be slightly sintered, thus the particle expelling phenomenon can be prevented when incorporated with high energy electrons. It is observed that the preheating could cause powder sintering effect (Gong and Chou, 2013), which may be decided by the preheating temperature. Thus, through the manipulation of preheating temperature it may be able to obtain different powder porosity with various powder bed conductivities. The change of powder bed heat dissipation ability may also contribute to the final deformation of overhang region.

To understand how overhang deformation can be affected by thermal response, a fundamental study of EBAM for thermal and mechanical evaluations is needed. Numerical simulation is a powerful method that can present thermomechanical response of the overhang building process, which is hard to observe from actual build process. Limited literatures about the process physics modeling of EBAM can be found. Zäh and Lutzmann (Zäh and Lutzmann, 2010) studied the melt pool geometry of EBAM process by a finite element method (FEM). Mahale (Mahale, 2009) developed a 3D numerical model in COMSOL to simulate the EBAM process temperature distribution of Al 7075 material. Jamshidinia et al. (Jamshidinia *et al.*, 2013a) utilized a thermal-fluid flow model to study powder porosity, process parameters and melt pool flow convection effect in EBAM process. For EBAM thermal stress simulation, a coupled Computational Fluid Dynamic (CFD) - Finite Element Method (FEM) model has been developed by Jamshidinia et al. (Jamshidinia *et al.*, 2013b) to investigate the temperature and stress evolution process. However, the powder sintering effect on EBAM overhang part stress and deformation has not been found in literature, it has not been fully discussed.

The objective of this research is to understand the thermal and mechanical characteristics in fabricating overhang layers under different powder porosities caused by various preheating conditions during the EBAM process. A three-dimensional (3D) finite element (FE) model was developed to simulate the thermal and mechanical phenomena in EBAM in a raster-scanning pattern across an overhang area. This study will establish relationship between preheating caused powder porosity and part overhang deformation so as to develop a porosity-controlled support free method for warping reduction. This method

could have broad usage in industrial applications since no support structure or mixture of different powder materials is needed.

6.2 Finite Element Modeling Approach

A 3D FE thermomechanical model was developed by using ABAQUS to simulate the process temperature history, residual stress distributions and deformation in a multi-layer raster scanning and deposition on an overhang model based on the developed thermal model in Chapter 3. Figure 6.3 (a) shows the geometry of the overhang model, which has an overall dimension of $13.6 \times 8.8 \times 10$ mm (length, width, and height). The overhang structure, which is placed in powder bed, has a dimension of $9.6 \times 4.8 \times 10$ mm (length, width, and height). A smaller model was used in order to keep a reasonable computational time. The thickness of the substrate is small comparing to the actual size of common parts; therefore, only the top section of the actual substrate was modeled. During simulations, powder layers were added to the substrate sequentially. The model volume was composed of a powder substrate on one side and a solid substrate on the other side (half and half) to represent an overhang fabrication (on top of the powder substrate), and the powder layers added were Ti-6Al-4V particles with a given levels of porosity.

The FE simulations consisted of a preheat phase, a melting phase, and a cooling phase. The preheating phase (also called initial phase) was simplified and considered as the initial thermal conditions. During the multi-layer deposition process, the layers to be deposited were not activated until the melting phase on that particular layer started. There was 10s cooling period between two consecutive layers which was considered as the new powder layer

deposition and preheating time. The whole model would drop to room temperature in the final cooling step.

Sequentially coupled thermomechanical simulation method was used to model the electron beam melting process. Transient thermal simulation were conducted first, heat transfer element (C3D8) was applied for the whole model. The element size is $0.2 \times 0.2 \times 0.035$ mm (x, y, z) in main scanning domain which has a dimension of 9.6×4.8 mm in length and width direction. Then, the obtained nodal temperature history was imported into the mechanical analysis model which obtained the mechanical element type of C3D8R. During the melting and cooling phase, the bottom surface of the solid substrate was fully constrained as the boundary condition. For the multi-layer raster scan, three layers of powder were simulated; the raster scan pattern is shown in Figure 6.3 (b). The stress and temperature characteristics along these scanning paths were analyzed from the simulation results. Since each scan (or layer) was considered as an intermediate scan (or layer) in a continuous multi-layer part building, the previous layer was considered to be transformed into solid bulk materials, meaning solidified from the powder in the previous melting scan.

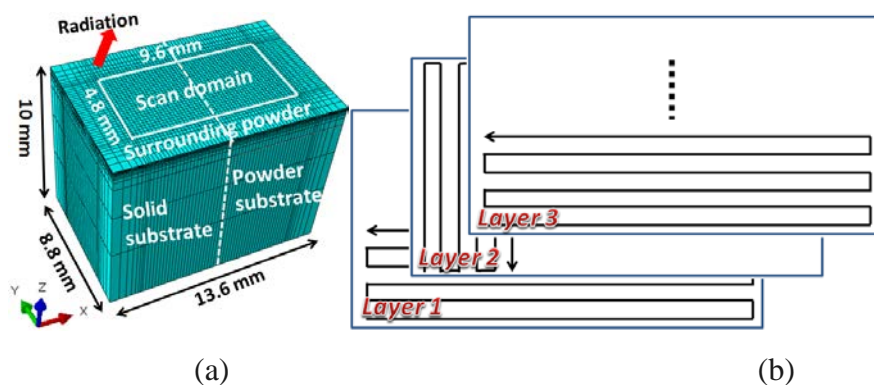


Figure 6.3. (a) Part mesh and geometry, and (b) scan pattern.

The material considered in this study was Ti-6Al-4V, its material properties, including both thermal and mechanical, temperature dependent, were from literature and

experimental studies. Temperature dependent thermal properties of powder and solid Ti-6Al-4V alloy have been summarized in Chapter 3. Material temperature dependent mechanical properties are obtained from Huang et al (Huang *et al.*, 2008). All the mechanical material properties are summarized in Figure 6.4, and were utilized in the thermomechanical model.

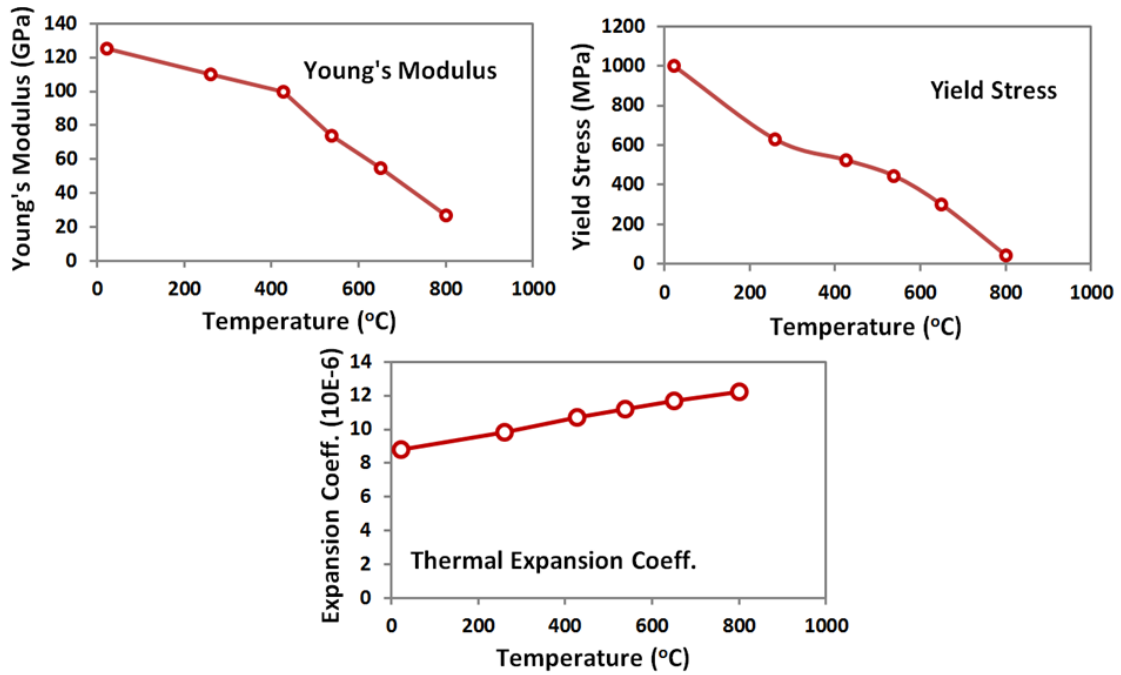


Figure 6.4. Temperature dependent material mechanical properties of Ti-6Al-4V (Huang *et al.*, 2008).

Two different porosity cases have been studied to investigate the preheating and powder porosity effect on overhang part temperature response, residual stress and deformation. The first case is 50% powder porosity case with a preheating temperature of 730 °C; this case is usually used in actual building process. The second case is considered to have a higher preheating temperature, e.g., 830 °C, which may decrease the powder porosity due to sintering effect. The powder porosity is assumed to be 35%. The process parameters used in the simulation are fixed values: 1000 mm/s scanning speed, 0.4 mm beam diameter and 4.5

mA beam current. A typical simulation still took around 100 hours using two Inter(R) Xeon(R) E5 CPUs.

6.3 Results and Discussion

6.3.1 Typical Example of Simulation Results

FE analysis was first performed for the overhang model with a powder porosity of 50%. Figure 6.5 shows the temperature distribution at the top surface in the model at the end of a three-layer deposition. It can be seen that the maximum temperature occurs at the end of the scanning with the magnitude around 2954 °C. In addition, the longer lasting of high temperatures in the scanned area of the right part (powder substrate) is significantly higher than the left side of the part (solid substrate), which is due to the low thermal conductivity and packing density of the powder substrate.

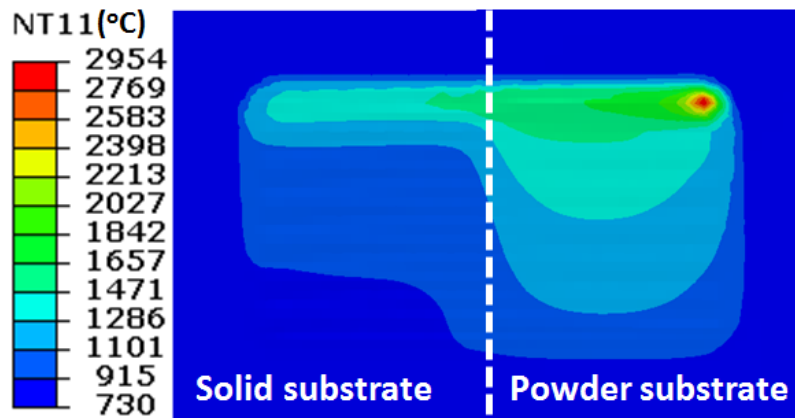


Figure 6.5. Temperature contour (top view) at the end of three-layer deposition.

Figure 6.6 displays temperature history of 2 nodes (A and B in Figure 6.6) above the powder and solid substrates on the first layer. Nodes A and B are on the center scanning path of the domain, with the same distance to the center of the EBAM part model (also the interface between the powder and solid substrates). Node A is above the powder substrate, while B above the solid substrate. The result shows that the peak temperature of Node A is

about 170 °C higher than Node B, also the cooling rate of Node A is noticeably slower than that of Node B.

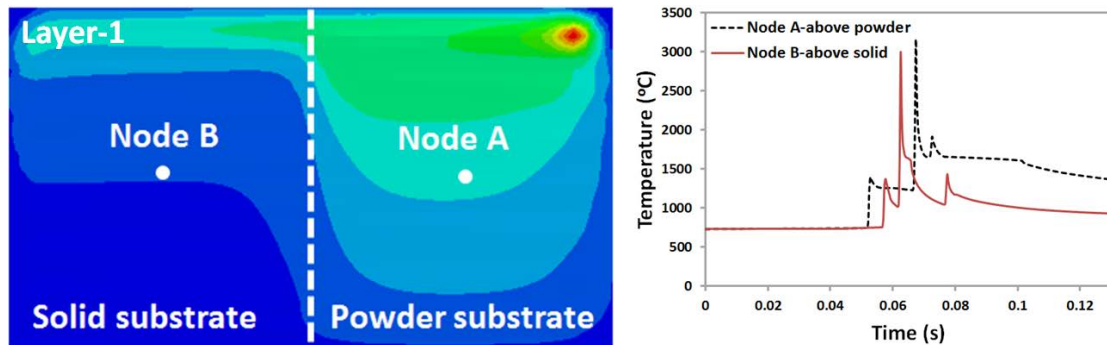
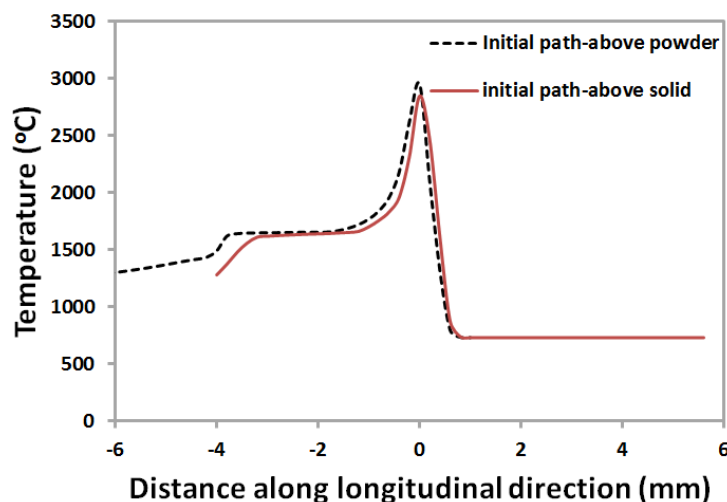
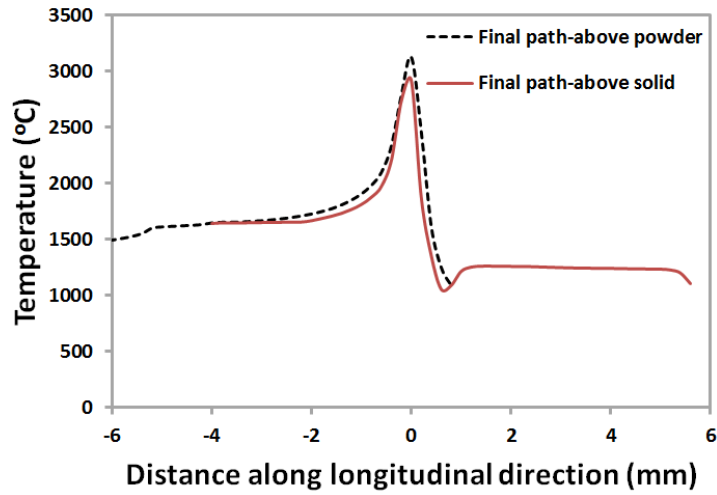


Figure 6.6. (a) Nodes location at first layer (scanning region), and (b) Temperature history information of the 2 nodes above powder and solid substrates.

Figure 6.7 shows the temperature profile around the electron beam center location (approximately at 0 mm in the distance axis) when the beam traveled above the powder and solid substrates during the initial and final scanning path of the first layer. Both Figure 6.7 (a) and Figure 6.7 (b) show that a higher maximum temperature occurred when the beam traveled above the powder substrate; this is again attributed to the significant lower thermal conductivity of the powder substrate and 50% packing density.



(a)



(b)

Figure 6.7. Temperature profiles around electron beam center (0 mm) above solid and powder substrates for initial and final path of layer-1.

Figure 6.8 illustrates the melt pool size shape when the electron beam traveled above the powder and solid substrates at the initial and final scanning paths of layer-1. The jagged melt-pool shape was due to element meshing, not fine enough. Table 6.1 further lists the dimensions of the melt pools. It can be noted when the beam traveled from the powder substrate to the solid substrate area, the melt pool sizes became smaller due to a higher thermal conductivity and full density of the solid substrate.

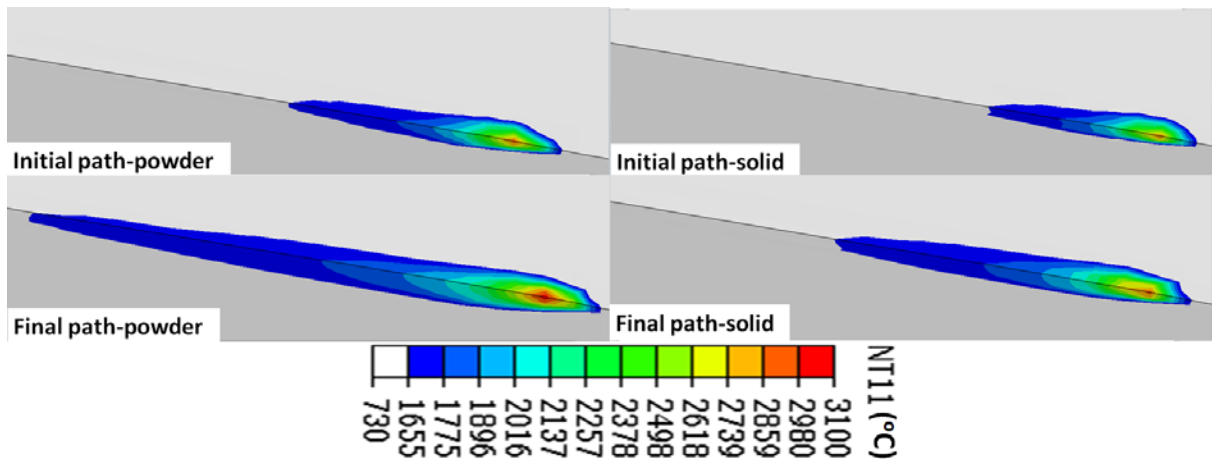


Figure 6.8. Melt pool size and shape of layer-1 in the powder and solid substrates at initial and final scanning paths.

Table 6.1. Melt pool size dimension of layer-1(unit: μm).

Melt pool	Initial Path	Final Path
-----------	--------------	------------

	Powder	Solid	Powder	Solid
Length	2190	1680	4171	2480
Width	650	600	725	690
Depth	110	97	152	105

Figure 6.9 illustrates the von Mises stress distribution in the overhang EBAM model after the final cooling stage. It can be found that noticeable deformation occurs around the overhang region when the whole model has been cooled down to the room temperature of 20 °C, which is the result of thermomechanical response during the repeated rapid heating-cooling process in EBAM layered manufacturing. It can be observed that the stress on the left part (solid substrate) is greater than that on the right part (powder substrate).

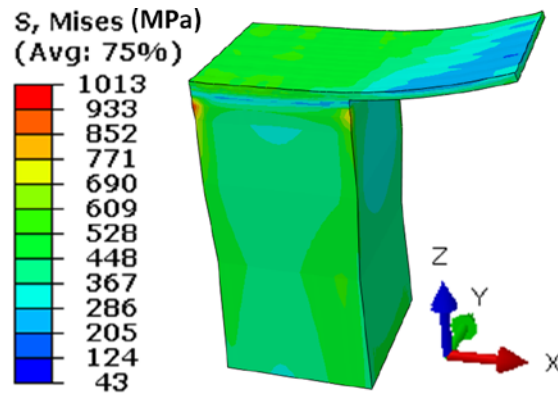


Figure 6.9. von Mises stress contour after final cooling (powder hidden).

Figure 6.10 displays the von Mises stress evolution of the nodes (Node A and B, same nodes as in Figure 6.6) above the solid and powder substrates. It has been noticed that each time when electron beam passed the nodes, a very small stress could be generated during the three layer deposition process. The final stress is mainly generated during the final cooling process. Due to difference in mechanical boundary condition, the stress results are also different, e.g., the maximum von Mises stress of node B (above solid substrate, fix boundary) is around 70 MPa higher than that of Node A (above powder substrate, free boundary) after the final cooling process.

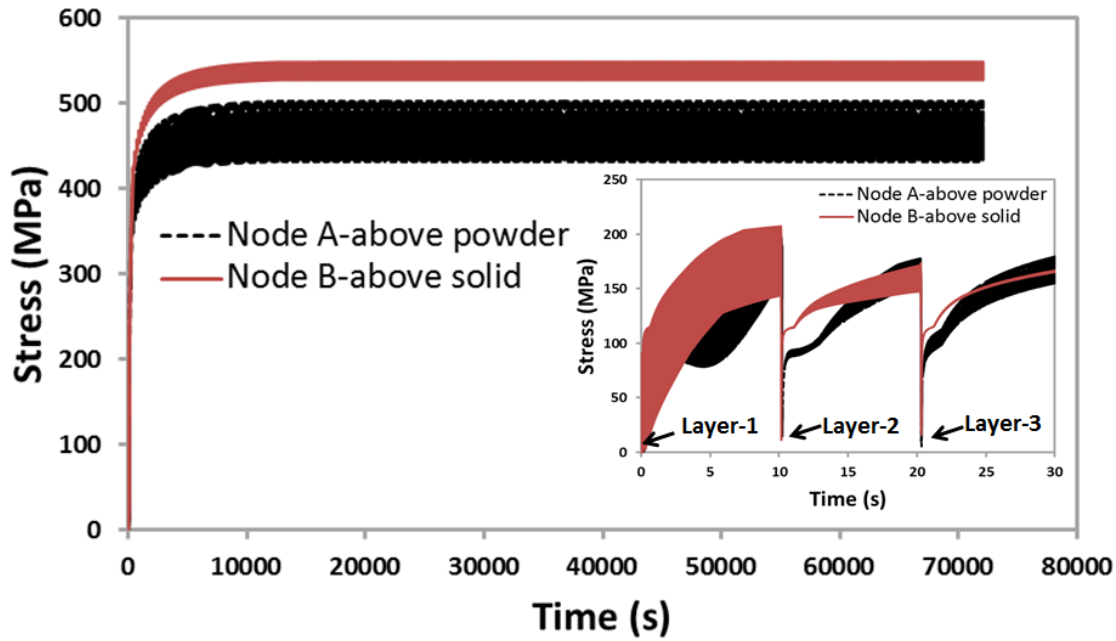


Figure 6.10. von Mises stress evolution of 2 nodes above solid and powder substrates.

6.3.2 Powder Sintering Effect Analysis

Simulations of cases with different porosity levels and preheating temperatures, 50% (730 °C) vs. 35% (830 °C), were conducted to examine the sintering effects. Figure 6.11 shows the temperature profiles on the paths for the EBAM model with different porosity levels at the end of three-layer deposition process. It can be noted that the average stress temperature on the scanning path increases slightly with the scanning paths due to residual heat effect, e.g., initial path and center path. It is also clearly evident that for the powder with a larger porosity, the temperatures above the overhang area are higher due to lower powder conductivity and packing density. However, the temperature above the solid substrate for porosity=35% case is higher than that of porosity=50% case, which may be caused by a higher preheating temperature of porosity=35% case.

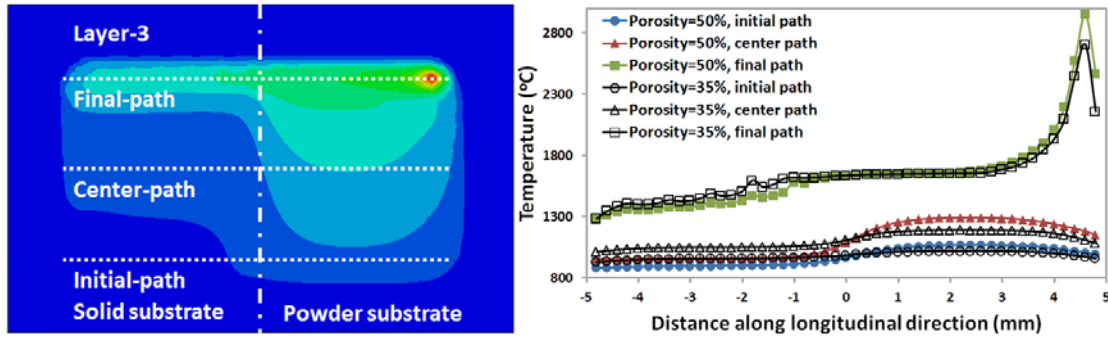
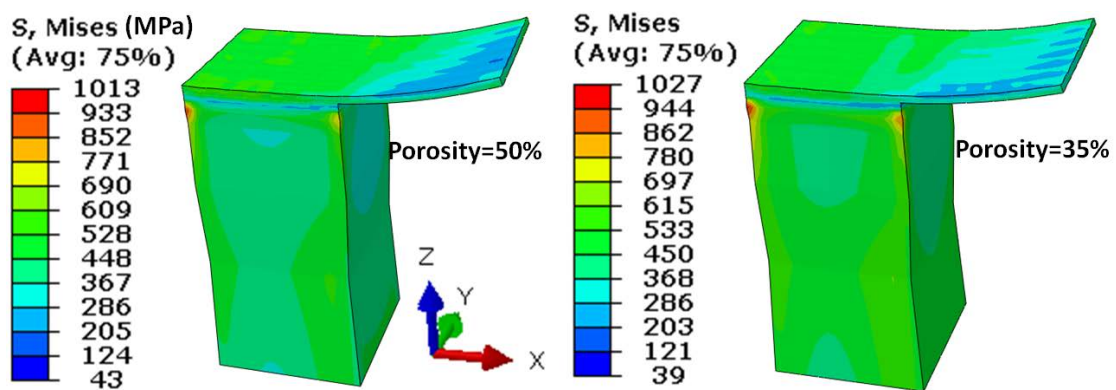
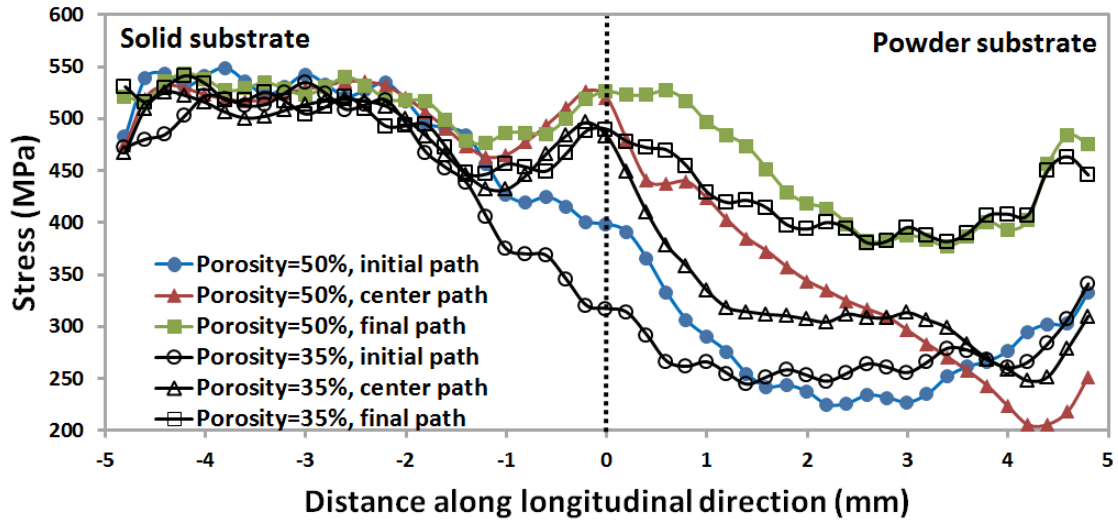


Figure 6.11. Temperature profiles on the scanning paths for two different powder porosity levels.

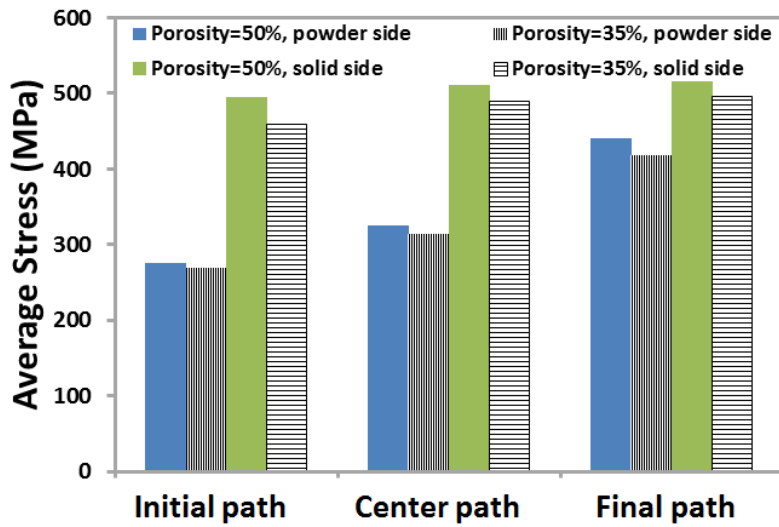
The von Mises stress information for the EBAM model with porosity of 35% and 50% has been collected. Figure 6.12 displays the von Mises stress on the three paths (initial, center, and final) of the third layer after the final cooling process for the EBAM model with different sintering effect (powder porosity levels). It can be noted that the average residual stress on the scanning path (powder side) increases with the scanning path number. In addition, the average von Mises stress in the overhang area increases, on all scanning path, when the powder porosity is larger; for example, the average von Mises stress on the final scanning path (powder substrate side) increases from about 418 MPa to about 440 MPa when the powder porosity increases from 35% to 50%.



(a)



(b)

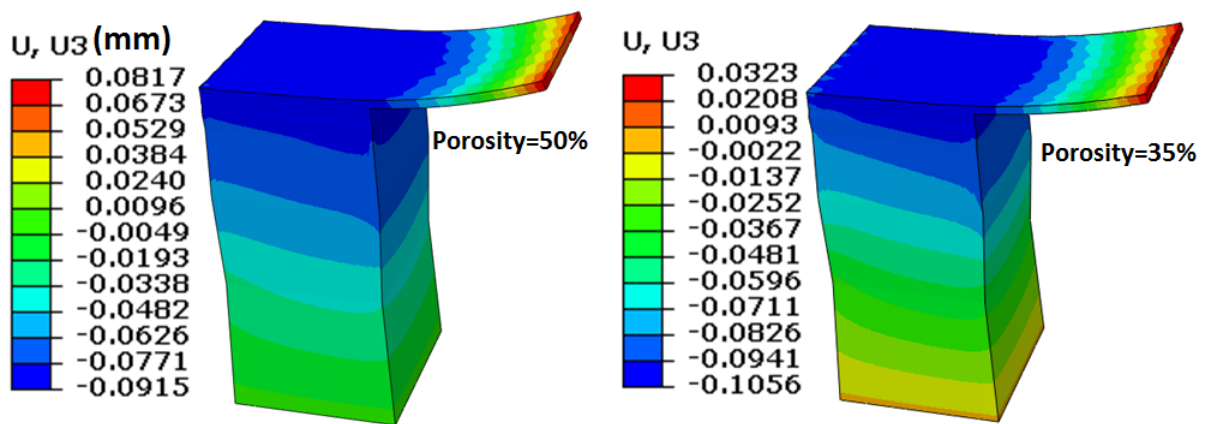


(c)

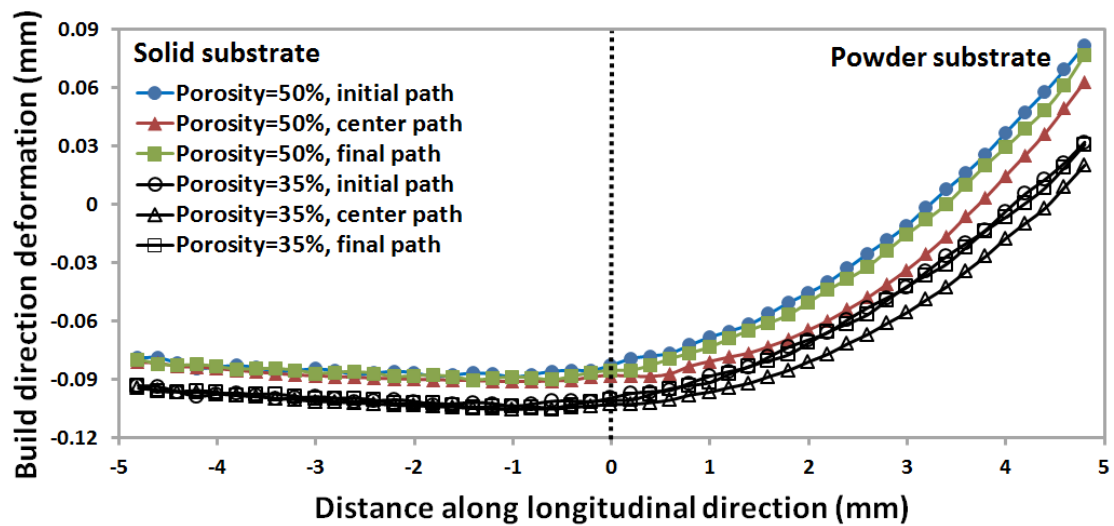
Figure 6.12. von Mises stress comparison after final cooling for different powder porosity levels

Typical examples of part warping for the two sintering effect (porosity level) cases after final cooling of 3 layers deposition are shown in Figure 6.13 (a) and (b). For both cases, it is noted that no deformation is shown around the bottom region due to fully constraint mechanical boundary condition of the solid substrate bottom region. The deformation magnitude continues to increase along building direction (Z direction). In addition, the largest deformation is observed to be around the tip region of overhang. The 50% porosity case

showed a larger max deformation in overhang region, which may be resulted by higher process temperatures and residual stresses observed earlier. Figure 6.13 (b) displays the final build direction deflection results on the three paths (initial, center, and final) of the third layer. Noticeable deformation reduction for all scanning paths has been observed for 35% porosity case. The results demonstrated that a high preheating temperature caused powder sintering effect could successfully bring down overhang deflection.



(a)



(b)

Figure 6.13. von Mises stress on different scanning paths of the third layer after final cooling for the models with different porosity levels.

6.4 Conclusion

In this study, a 3D FE thermomechanical model was developed for temperature and stress simulations in EBAM, particularly, applied to investigate temperatures and stresses when fabricating an overhang feature, which by nature is above a powder substrate. Ti-6Al-4V powder materials with two different porosity levels, resulted from different preheating conditions, were studied. The major findings can be summarized as follows.

1. The poor thermal conductivity of Ti-6Al-4V powder results in higher temperatures, also slower heat dissipations, in overhang areas during an EBAM build;
2. The retained higher temperatures in the area above the powder substrate, when building an overhang feature in EBAM, result in noticeable overhang deformation after final cooling;
3. A smaller porosity (e.g., 35% vs. 50%) may reduce the process temperatures, residual stresses and final deformation, associated with building an overhang.

Acknowledgements

The materials presented in this paper are supported by NSF (Award No. 1335481) and NASA (Award No. NNX11AM11A). This research is in collaboration with Marshall Space Flight Center (MSFC), Advanced Manufacturing Team. Helpful discussions with K. Cooper, J. Lydon and M. Babai at MSFC are acknowledged.

References

- Cormier, D., Harrysson, O., & West, H. (2004). Characterization of H13 steel produced via electron beam melting. 14th Annual Solid Freeform Fabrication Symposium, University of Texas, Austin, Texas, 4-6 August 2003.
- Gong, X., & Chou, K. (2013). Characterization of Sintered Ti-6Al-4V Powders in Electron Beam Additive Manufacturing. ASME 2013 International Manufacturing Science and

Engineering Conference, Madison, WI, June 10-14, 2013, MSEC2013-1131.

- Huang, B., Yang, Y., Luo, H., Yuan, M., & Chen, Y. (2008). Effect of the interfacial reaction layer thickness on the thermal residual stresses in SiCf/Ti-6Al-4V composites. *Materials Science and Engineering: A*, 489(1), 178-186.
- Jamshidinia, M., Kong, F., & Kovacevic, R. (2013a). Numerical Modeling of Heat Distribution in the Electron Beam Melting® of Ti-6Al-4V. *Journal of Manufacturing Science and Engineering*, 135(6), 061010.
- Jamshidinia, M., Kong, F., & Kovacevic, R. (2013b). The Coupled CFD-FEM Model of Electron Beam Melting® (EBM). *Mechanical Engineering Research*, Paper 4.
- Mahale, T. R. (2009). Electron beam melting of advanced materials and structures. Paper presented at the Ph.D. thesis, North Carolina State University, Raleigh, NC.
- Mumtaz, K., Vora, P., & Hopkinson, N. (2011). A Method to Eliminate Anchors/Supports from Directly Laser Melted Metal Powder Bed Processes. 22nd Annual International Solid Freeform Fabrication Symposium - An Additive Manufacturing Conference, Austin, TX, USA, August 8-10, 2011.
- Murr, L., Martinez, E., Gaytan, S., Ramirez, D., Machado, B., Shindo, P., Ciscel, D. (2011). Microstructural architecture, microstructures, and mechanical properties for a nickel-base superalloy fabricated by electron beam melting. *Metallurgical and Materials Transactions A*, 42(11), 3491-3508.
- Ramirez, D. A., Murr, L. E., Martinez, E., Hernandez, D. H., Martinez, J. L., Machado, B. I., Wicker, R. B. (2011). Novel precipitate-microstructural architecture developed in the fabrication of solid copper components by additive manufacturing using electron beam melting. *Acta Materialia*, 59(10), 4088-4099.
- Vora, P., Derguti, F., Mumtaz, K., Todd, I., & Hopkinson, N. (2013). Investigating a Semi-Solid Processing Technique Using Metal Powder Bed Additive Manufacturing Processes. 24th Annual International Solid Freeform Fabrication Symposium - An Additive Manufacturing Conference, , Austin, TX, USA, August 12-14, 2013.
- Zäh, M. F., & Lutzmann, S. (2010). Modelling and simulation of electron beam melting. *Production Engineering. Research and Development*, 4, 15-23.

CHAPTER 7

GEOMETRIC CONSIDERATION OF SUPPORT STRUCTURES IN PART OVERHANG FABRICATIONS BY ELECTRON BEAM ADDITIVE MANUFACTURING

Abstract

Powder bed electron beam additive manufacturing (EBAM) has emerged as a potentially cost-effective process for high-value, small-batch productions for biomedical and aerospace applications. In EBAM, the process would not require support structures for overhang geometry because a build part is immersed in the powder bed. However, support structures are indeed needed in practice for an overhang; without it, the overhang area will have defects such as warping, which are due to the complex thermomechanical process in EBAM. In this study, a numerical approach is introduced to simulate the thermomechanical responses in the EBAM process of overhang structures. The objective of this study was to develop a 2D thermomechanical model, using a finite element method (FEM), to evaluate temperature induced deformation on different overhang support patterns in the EBAM process. The major results are summarized as follows. (1) The thermomechanical model is able to simulate the deformation of overhang parts in EBAM. The overhang length noticeably affects the overhang deformation. (2) As a traditional support structure, solid columns can reduce the overhang warping; further, the size of the column may be minimized to satisfy a deformation constraint, and meanwhile, reduce the amount of support materials. (3) Including a solid piece beneath the overhang, acting as a heat sink, may also reduce the overhang

deformation; however, an appropriate gap must be incorporated so not to fuse to the overhang area, while still effectively reducing the deformation.

7.1 Introduction

Additive manufacturing (AM) based on “layer-adding” fabrications is a group of technologies, by which a physical solid part is produced directly from digital data of the part geometric model. This group of technologies offers many design and manufacturing advantages such as short lead time, design freedom in geometry, and tooling-free productions. Powder-based electron beam additive manufacturing (EBAM) is a relatively new AM technology (Gong *et al.*, 2012); it utilizes a high-energy electron beam, as a moving heat source, to melt and fuse metal powder and produce a solid part in a layer-by-layer fashion. The process detail can be found in literature (Gaytan *et al.*, 2009). EBAM is one of a few AM technologies capable of making full-density metallic parts, which drastically broaden AM applications in a wide variety of industries (Biamino *et al.*, 2011; Gong *et al.*, 2012).

Because of the high energy density, EBAM has the potential to work with many material classes, e.g., aluminum alloys (Yu *et al.*, 2009), tool steel (Cormier *et al.*, 2004), cobalt-based superalloys (Gaytan *et al.*, 2010), Cu (Ramirez *et al.*, 2011), and Inconel alloys (Murr *et al.*, 2011), etc. One titanium alloy, Ti-6Al-4V, was the first material extensively researched (Murr *et al.*, 2009; Parthasarathy *et al.*, 2010), also widely used, in EBAM technologies for aircraft parts and medical implants. Moreover, Intermetallic groups such as titanium aluminide have also been studied for EBAM applications, but the process development was considered very time consuming (Sabbadini *et al.*, 2010). Another

intriguing EBAM capability is to fabricate complex geometries and structures (e.g., meshed, porous, cellular).

One of the advantages in AM technologies is freedom in part geometry designs. However, for some AM processes, e.g., the material extrusion type AM, also known as fused deposition modeling (FDM), part designs with overhang (or undercut) geometry are considered not favorable. In such an AM process, a part overhang will require the so-called “support structure” to carry the weight of the overhang portion. However, the support structure has to be removed during post-processing, which may be time consuming and add additional production cost. Hence, overhang geometry may be considered as undesired design geometries. Some approaches have been used to tackle support structure removals, e.g., designing break-away structures or using water solvable materials in FDM. On the other hand, powder-bed-fusion AM processes including EBAM are considered not requiring a support for an overhang because the powder bed itself is able to bear the weight of a built overhang. However, in common practices, still, the general rule is to arrange support structures underneath an overhang, or defects such as warping may occur. Defects such as warping associated with overhang geometry problems in EBAM have not been frequently studied in literature. Recently, Vora et al. (Vora *et al.*, 2012) attempted to benchmark the problems with overhangs and reported cases that overhang warping occurs.

For laser-based powder bed AM processes such as selective laser sintering or melting (SLS or SLM), there are a few studies related to support structures in literature. The focus was, however, on the design and fabrication of support structures. Jhabvala et al. (Jhabvala *et al.*, 2012) reported using pulse laser, instead of a continuous mode, to fabricate support

structures and claimed the fabricated supports are much easier to be removed. Yan et al. (Yan *et al.*, 2012) studied “cellular lattice” structures for support and investigated the effect of cellular geometry parameters. The evaluation criterion was the ease of removal and access. The authors also intended to use cellular-type support to minimize the material volume needed for support. In general, the above mentioned studies have not comprehensively addressed the aspect of the need of supports for an overhang and for suitable support types.

EBAM has a potential to be a cost-effective alternative to conventional discrete component manufacture for high-value, small-batch, and custom-designed metallic parts. However, one of the challenges in part designs is inevitable overhang geometries. The overhang area will require support structures, or there will be defects around the overhang area, shown in Figure 7.1, including size inaccuracy and, most noticeably, distortions. Furthermore, post-processing for support removal can be labor intense and time consuming. There are commercial software packages, e.g., Materialise (Materialise Software, 2012.), which can generate support structures with a variety of options (patterns/size); however, there is no clear guideline of support design, relying on trial and error and experiences. Moreover, it needs to be pointed out that those support designs were developed more for the weight-carrying purpose, to avoid overhang area deformation due to gravity. It does not address the powder bed conditions for the process like EBAM. Moreover, additional questions are: what is the root cause of overhang defects, and what type of “support” configurations will function to minimize warping defects, and yet, without burdening post-processing?

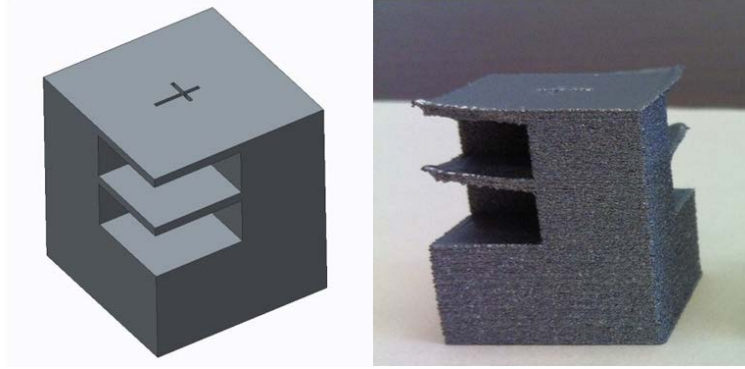


Figure 7.1. An example of overhang model and associated warping defect.

To effectively design necessary supports, it is essential to understand the source of defects associated with overhang geometries in EBAM. It is argued that for EBAM, heat load, instead of gravity load, is more the source of the problems. Because the powder bed (with sintered powder) has a far poor thermal conductivity compared to a solid, and thus, heat dissipation around the overhang area may be less efficient compared to an area with a solid substrate. The assumption of overhang defect causes, therefore, is that in the powder area beneath an overhang, the ineffective heat dissipation, repeated thermal gradient cycles and the shrinkage of deposited layers result in warping defects. Hence, the research needs would be a fundamental thermomechanical study of EBAM for distortion evaluations. The knowledge obtained may be applied to facilitate investigations of different overhang configurations, thermal and mechanical responses, and to enable effective designs for heat load supports and simultaneously for ease of support structure removals.

In this study, a 2D FEM model, incorporating Gaussian heat flux distribution, latent heat of fusion and temperature dependent material properties, was developed to study the thermomechanical response when subject to a moving heat source of high intensity. The model can be used to study the temperature induced deformation in fabricating overhang parts with different support structures in the EBAM process. By utilizing the

thermomechanical model, it is possible to improve the quality of EBAM parts through effective support structures.

7.2 Finite Element Modeling for Overhang Study

7.2.1 Thermal Analysis

The thermal analysis information such as moving heat source and latent heat of fusion can be found in Chapter 3. However, this study is focused on 2D model, only x-y plane is modeled and scanned by the heat source. The heat source is moving along the x-direction at a constant speed, and the z direction is replaced by y coordinate. Thus heat source equation becomes the following:

$$\dot{Q}_{(x,y)} = \eta \times \frac{H_s \times I_y}{s} \quad (10)$$

with

$$I_y = \frac{1}{0.75} \left(-2.25 \left(\frac{y}{S} \right)^2 + 1.5 \left(\frac{y}{S} \right) + 0.75 \right),$$

$$H_s = \frac{2UI_b}{\pi\Phi_E^2} \exp \left\{ -\frac{2[(x-x_s)^2]}{\Phi_E^2} \right\}$$

7.2.2 Structural Analysis

During the electron beam scanning process, the rapid heating and cooling process is localized and large temperature gradient is expected to occur over a small area. Due to resulted thermal gradients, thermal stresses and distortions may be generated in the build part. The governing equations, used to describe the relationship between temperature and the corresponding thermal strain as well as stress, is (Marimuthu *et al.*, 2013):

$$\{\varepsilon\} = [D]^{-1}\{\sigma\} + \{\varepsilon^{th}\} \quad (11)$$

$$\{\varepsilon^{th}\} = \alpha_e \times \Delta T = \alpha_e(T - T_{ref}) \quad (12)$$

$$\{\sigma\} = [D]\{\varepsilon\} \quad (13)$$

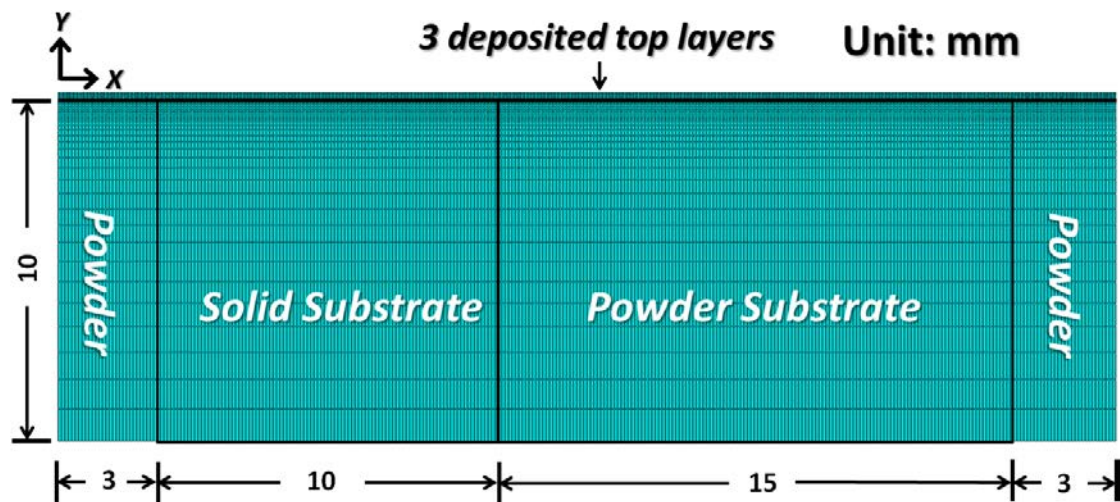
Where $\{\varepsilon\}$ is the total strain, $\{\varepsilon^{th}\}$ is the thermal strain, α_e is the coefficient of expansion, T is the incident temperature, T_{ref} is the reference temperature, $[D]$ is the stress-strain matrix, and $\{\sigma\}$ is the stress matrix.

7.2.3 Material Properties Modeling

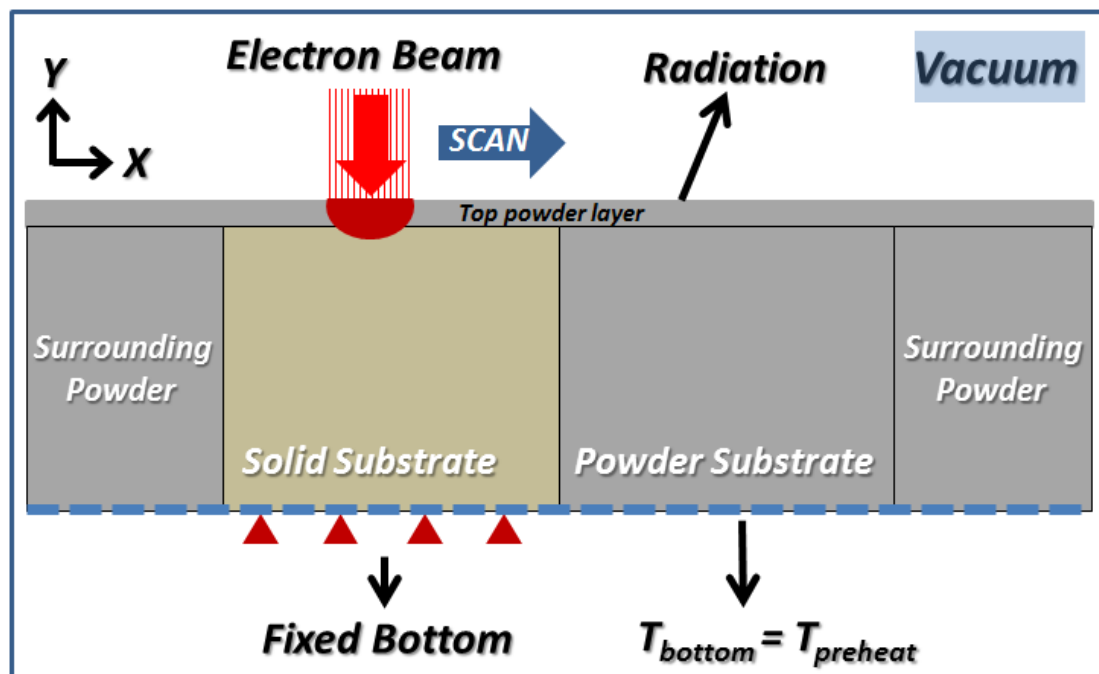
The material considered in this study was Ti-6Al-4V, its material properties, including both thermal and mechanical, temperature dependent, were from literature and experimental studies. Temperature dependent thermal and mechanical properties of powder and solid Ti-6Al-4V alloy have been summarized in Chapter 3 and Chapter 6. An isotropic kinematic hardening model is used without considering the modeling of complex viscoplastic behavior.

7.2.4 Numerical Model Configuration

A 2D finite element analysis thermomechanical model is developed by using ABAQUS to simulate the temperature induced deformation in a multi-layer deposition process of an overhang model. Figure 7.2 (a) shows the geometric details for a typical overhang model, which has a substrate placed in powder bed. The powder material is Ti-6Al-4V powder (sintered) with 50% porosity. A thin layer, on the top of the substrate, is assumed to be the latest added powder layer, which also has the powder properties. In this study, a total of 3 layers will be deposited sequentially above substrate. A conical body heat source with linearly decaying along y-direction (building direction), and scanning along x-direction, has been applied on the top powder layer, shown in Figure 7.2 (b).



(a)



(b)

Figure 7.2. Model geometric information.

The major analysis step is consisted of preheating cycle, electron beam scanning/melting cycle and cooling cycle. The beam preheating cycle is simplified as the thermal initial conditions for both substrate and powder layer, and then assigned with a uniform temperature distribution of $T_{preheat}$. Electron beam moving and heating will be initiated at the scanning/melting cycle. Due to vacuum working environment, convection

between the powder layer and surroundings is ignored, only the radiation is considered in the heat transfer between the part and environment. The temperature of substrate bottom is confined as a constant temperature of T_{preheat} as the thermal boundary condition. The electron beam scanning occurs at the top surface of a powder layer and traverses along the x-axis with a constant speed. In the center of the electron beam when temperature exceeds the evaporating point, the node is set to be remained in the mesh. All the mechanical Degrees of Freedom (DOFs) are confined at the bottom of the solid substrate since the bottom was constrained by steel plate. Figure 7.2 (b) shows all the applied thermal and mechanical boundary conditions in scanning cycle.

After the scanning/melting phase, the simulation of the cooling phase was followed. There are two cooling steps in the EBAM process. The first cooling step is in the melting phase which is actually the part temperature self-balancing corresponding to a few seconds interval before a new powder layer spreading. The time is assumed as 10 seconds, which is approximately the duration for the next powder layer spreading during the EBAM process. The second cooling step is the final cooling; all the materials are assumed to be simply under cooling process until the temperature drops to the room temperature of 20 °C. The displacement constraints at the bottom surface of solid substrate are kept due to the same aforementioned bonding issue. The thermal boundary condition is pure radiation on the top surface; the confined bottom temperature boundary condition is removed.

Model change element activation method is applied to simulate the powder layer addition process in this 3-layer deposition simulation. The second and third layer powders are modeled at the very first beginning, but deactivated in the melting phase of the first layer.

The second and third powder layer will be reactivated at the second and third melting phase respectively. During each reactivation process, the bottom temperature is still kept as the $T_{preheat}$ and the surface radiation boundary condition will be deactivated for the previous layer while activated for the newly deposited layer. Then, the beam scanning process starts again from the same starting point on the top powder layer. Detailed modeling parameters other than process parameters are the same with those used in Chapter 3. The process parameters used for all simulation cases are: 1000 mm/s scanning speed, 0.6 mm beam diameter and 9 mA beam current. Figure 7.3 (a) shows the flow chart of numerical procedure of the developed model; Figure 7.3 (b) presents the multi-layer deposition and simulation process.

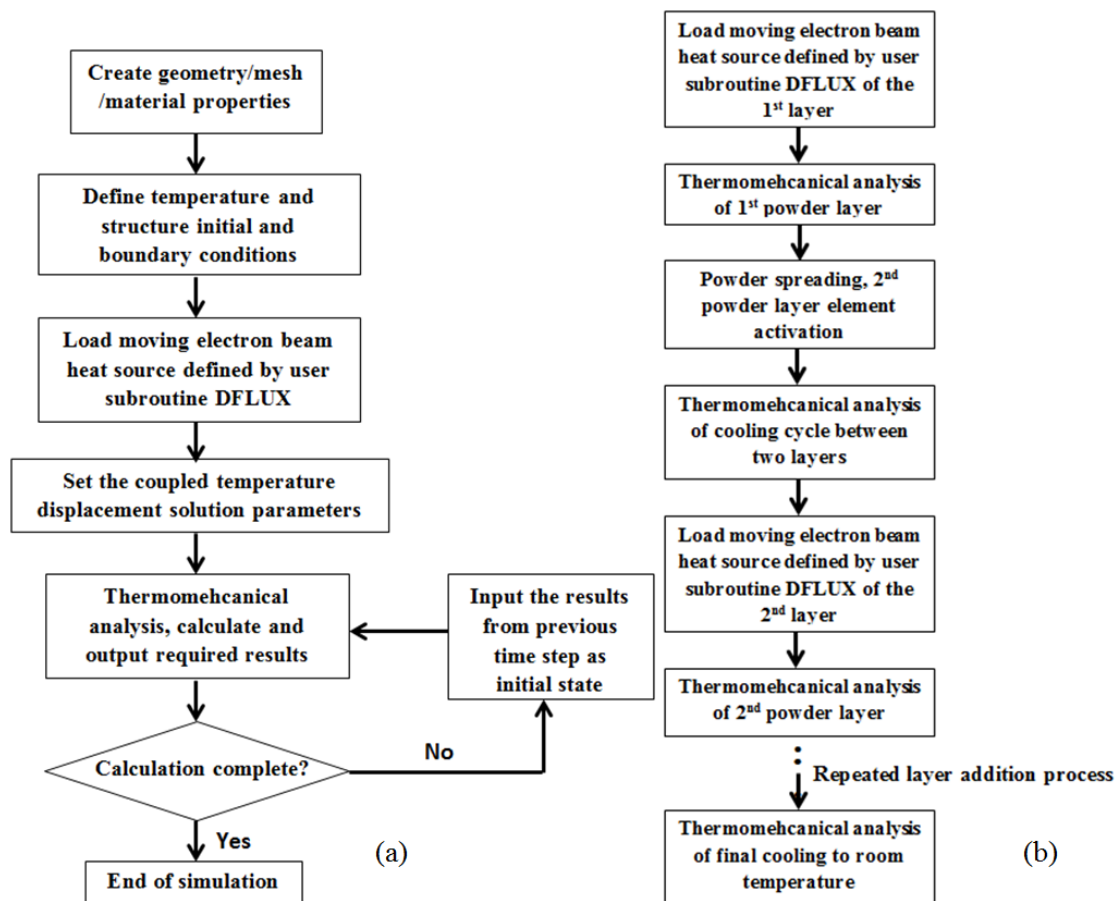


Figure 7.3. Flow chart of numerical simulation procedure used for the overhang model developed for EBAM.

Coupled thermal-displacement elements (CPE4T) were used for the whole model. In order to save computational time and keep good model accuracy, a finer mesh was applied in the beam scanning path to directly incorporate the incident Gaussian beam heat flux region while coarser mesh was used in regions away from high beam energy affected zone. The element size in the scanning area was $100\ \mu\text{m} \times 35\ \mu\text{m}$ (x×y) with the mesh size gradually increases with the distance away from the primary scanning area. The typical computational time for one simulation case is around 20 hours using two Inter(R) Xeon(R) E5 CPUs.

7.3 Overhang and Support Structure Simulation Study

The distortion phenomenon in the EBAM process can be explained by temperature induced deformation mechanism (Mercelis e Kruth, 2006). Due to the rapid heating of the upper surface by the fast moving electron beam and the comparatively slow heat conduction, a steep temperature gradient develops. Then the underlying material, which has a lower temperature, restricts the expansion of the heated deposited layers and counter compressive strains are induced. Therefore, without mechanical constraints on the top surface, a counter bending away from the electron beam can be expected. In the cooling period, the compressed deposited layers start shrinking and a bending angle towards the beam develops. Figure 7.4 shows the temperature induced deformation mechanism.

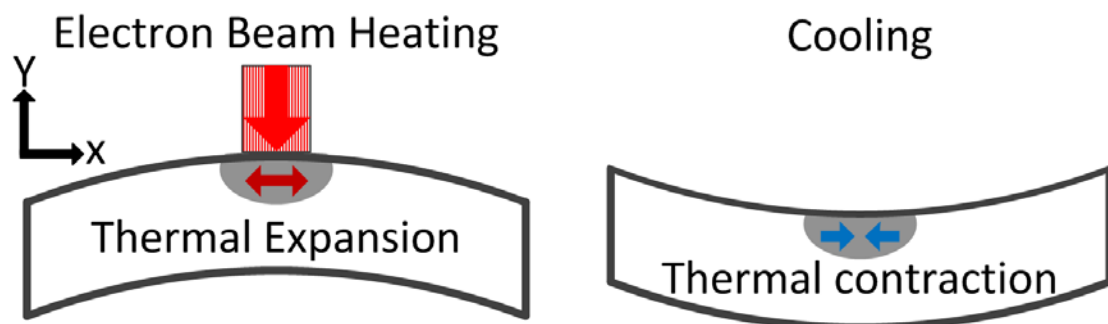


Figure 7.4. Temperature induced deformation.

During the powder deposition process, the newly deposited material is automatically placed above the powder bed. Therefore, the inefficient heat dissipation around the overhang area, caused by poor thermal conductivity, and the shrinkage of the deposited layers may lead to warping defects. An initial FEM study has been conducted to investigate the overhang warping. A model with a 2-layer deposition process, based on Figure 7.2, has been constructed for this thermomechanical simulation study. It has a substrate dimension of 16×10 mm (Length \times Height) consisting of half powder and half solid.

Two cases with different substrate types have been investigated in order to evaluate the overhang effect. One (Case A) is the solid substrate case; while the other (Case B) is the half solid and half powder substrate (overhang) case. For the overhang region above the powder bed, it can be expected that a larger warping would occur due to higher max temperature, e.g., ~ 2980 °C of Case B and ~ 2940 °C of Case A, as shown in Figure 7.5. Their stress contour plots along the scanning direction (x-direction) after the final part cooling (to room temperature of 20 °C) have been shown in Figure 7.6 (a) and (b). The surrounding powder has not been shown in both cases since the major area of focus is the scanning region. The deposited top layers have shrinkage stresses that lead to warping. In addition, due to the smaller solid substrate area for Case B, the warping above the solid substrate could be reduced. The top surface deflection profiles for both cases are shown in Figure 7.6 (c). The results clearly illustrate the warping trend as discussed: Case B has a larger warping defect above the powder substrate while a smaller deformation is shown above the solid substrate.

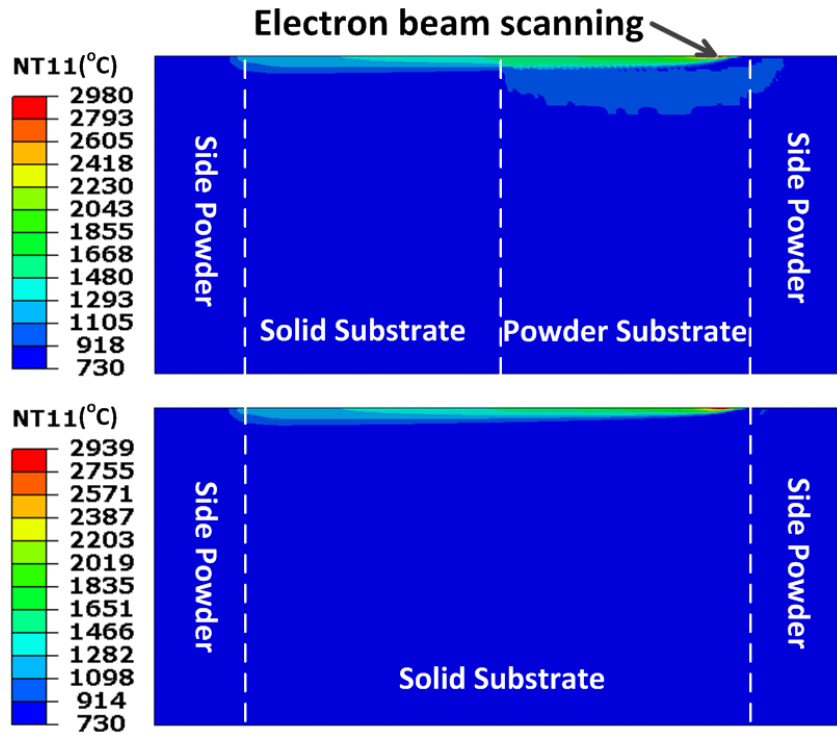
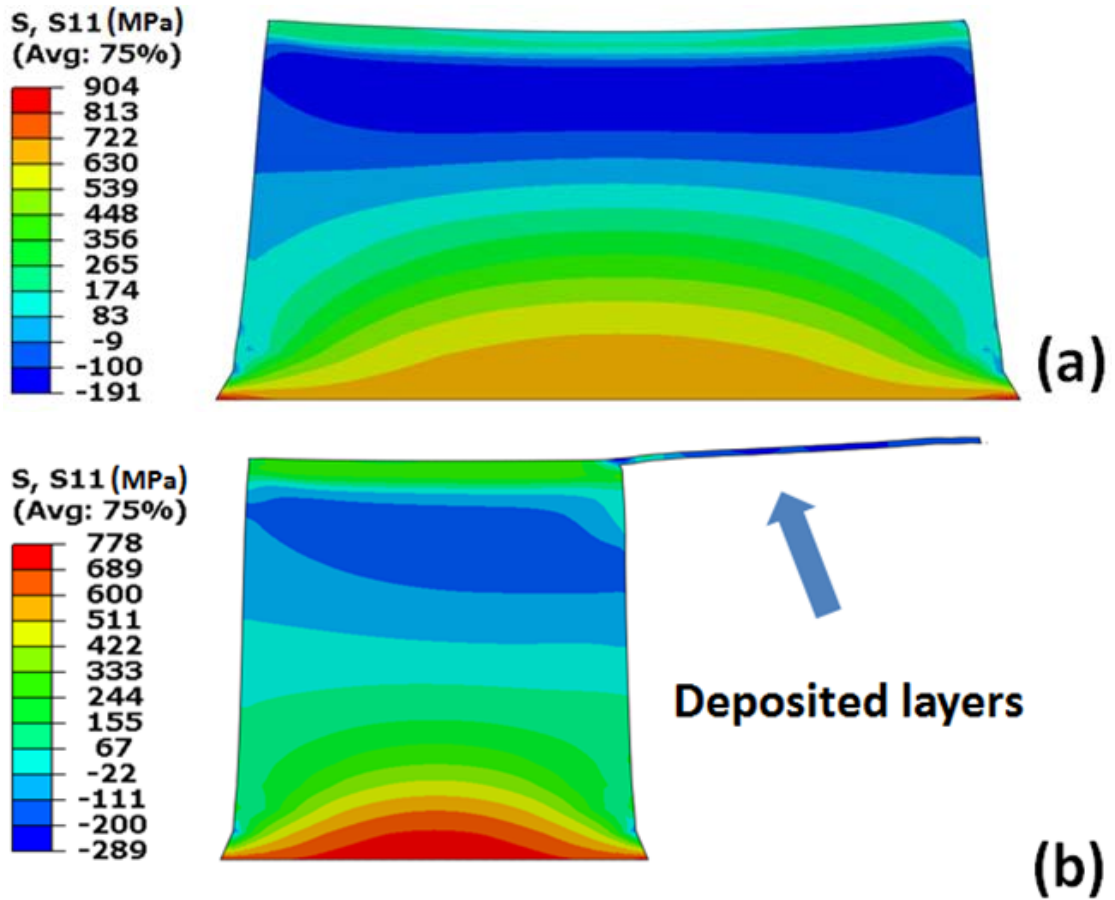


Figure 7.5. Temperature contours of electron beam scanning on layer-2 for overhang substrate vs. solid substrate cases.



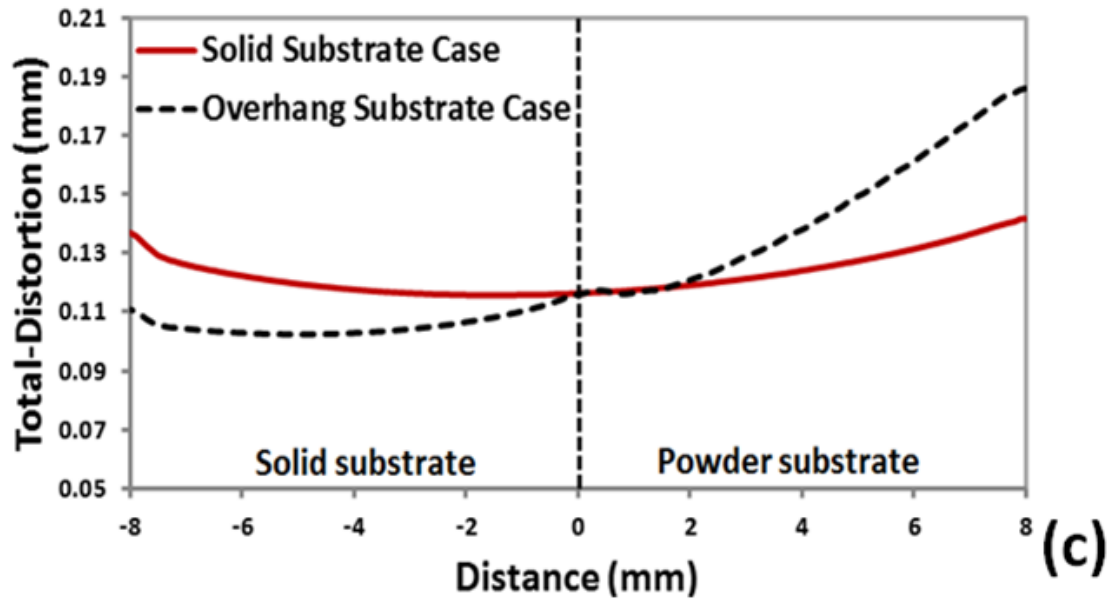
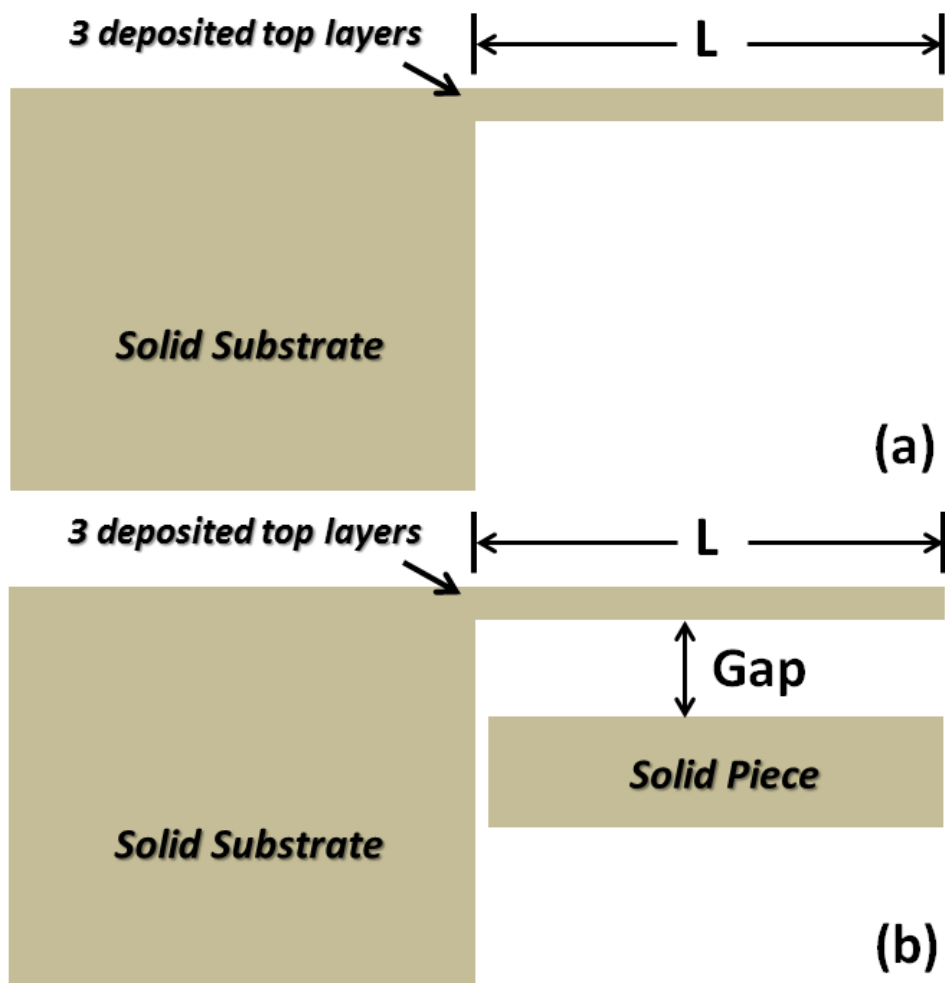


Figure 7.6. (a) and (b) Typical example of residual stress contours after final cooling (to room temperature); (c) typical example of top surface deformation plots after final cooling.

According to the above simulated results, the overhang structure can result in a serious part warping problem. Therefore, improved designs of overhang geometry (e.g., support features) may help to reduce the distortion of the overhang area. The numerical model can be a cost-effective way to study thermomechanical responses of different overhang support features when subject to a moving heat source. Three types of overhang structures, each with different control dimensions and support features, have been constructed based on Figure 7.2. Their structural configurations are shown in Figure 7.7; in which the parameters are: L is the overhang length; W_c is the width of the support column; Gap is the distance between bottom surface of the first deposited layer and the top surface of the solid piece (solid Ti-6Al-4V material). For all the cases, there are a total of three deposited top layers above the substrate. Figure 7.7 (a) shows the configuration of the overhang length effect model, L will be 5, 10, 15 and 25 mm. The solid column model ($L=15$ mm) is shown in Figure 7.7 (b). The bottom surface of the column will be fully constrained. The width, W_c ,

will have three values of 0.5, 1.0 and 1.5 mm. A solid piece under the deposited layers may improve the heat dissipation due to the increase of conductivity in the powder substrate. However, the gap between the solid piece and the deposited layers may present an issue since the gap distance will affect the heat transfer between the deposited layers and the solid piece. Figure 7.7 (c) describes the gap effect model configuration ($L=15$ mm), the gap distances will be 0, 0.63 and 6.3 mm.



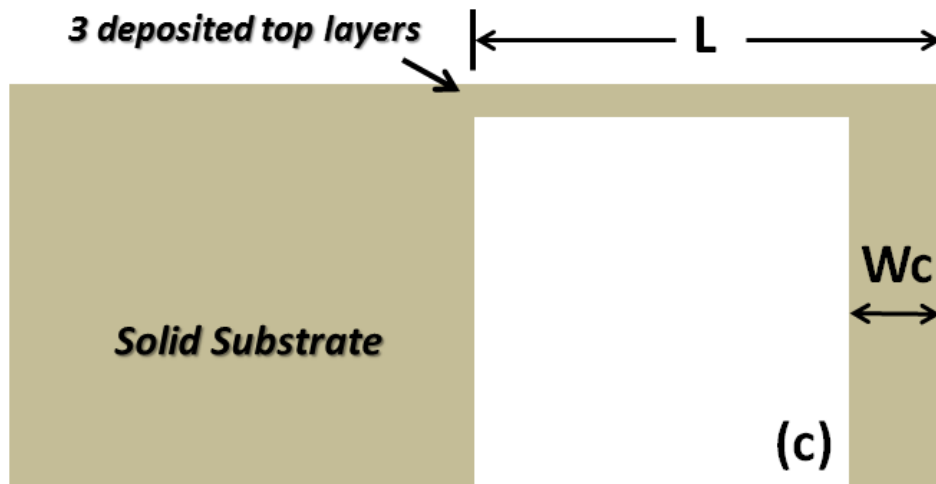


Figure 7.7. Geometric considerations of different support structure.

7.4 Results and Discussion

7.4.1 Overhang Length Effect

One typical example of part warping after final cooling of the 3-layer deposition for the 15 mm overhang length case is shown in Figure 7.8 (a). The surrounding powder has not been shown in order to improve the illustration of the overhang deformation. The aforementioned temperature induced deformation mechanism can also be applied here. Due to a full constraint of the bottom surface of the solid substrate, no deformation is shown around the bottom region; the deformation magnitude continues to increase along the building direction. The largest deformation appears around the right region of the overhang area.

To better understand the overhang length effect, a set of simulations with different overhang lengths ($L = 5$ mm, 10 mm, 15 mm and 25 mm, respectively) have been completed. The top surface deformations (along the scanning path) have been plotted in Figure 7.8 (b), which clearly indicates that a larger deformation will be caused by a longer overhang length.

Therefore, a short overhang length should be used in the building process to reduce part warping if no additional support structure is applied.

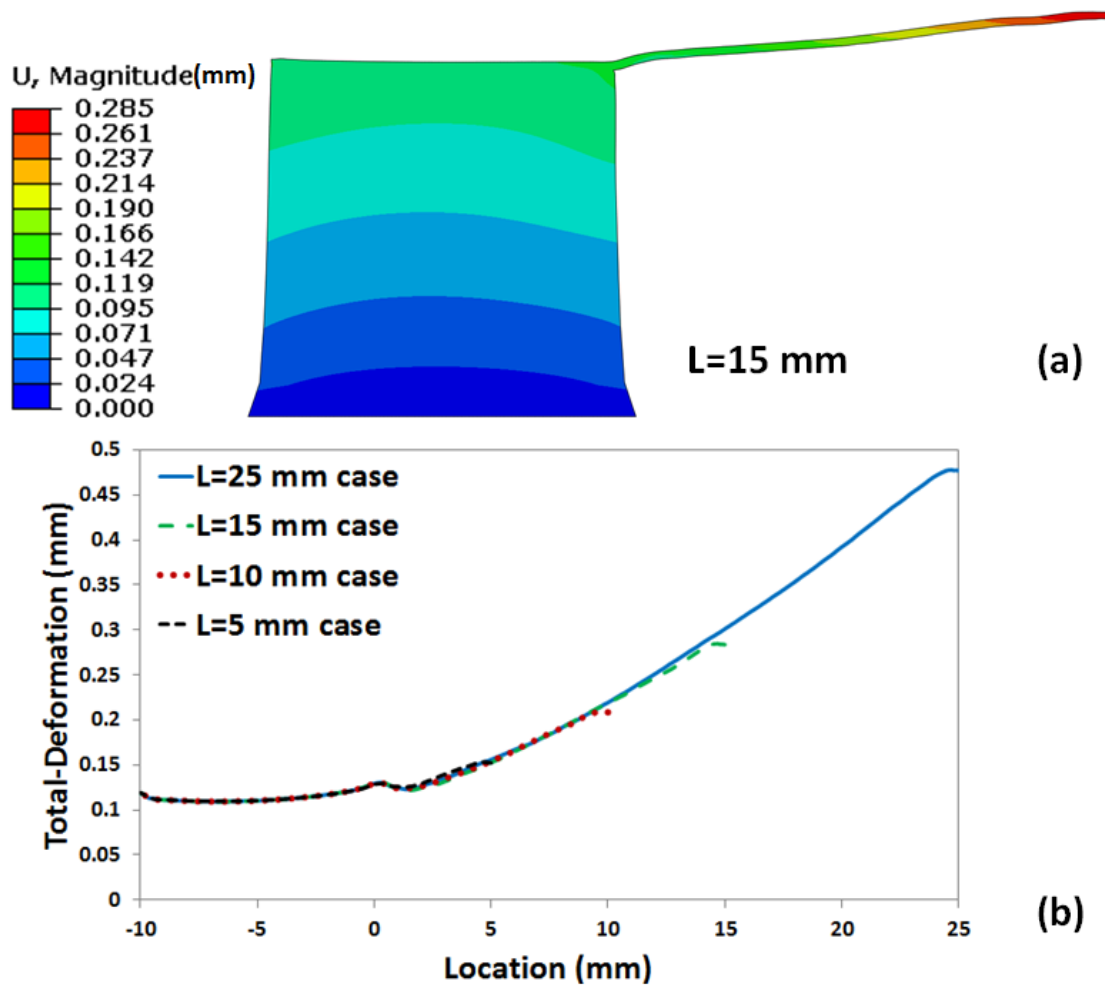


Figure 7.8. (a) Typical example of deformation contours after final cooling for overhang length case (L=15 mm); (b) different overhang lengths (top surface deformation plots).

7.4.2 Support Column Effect

Figure 7.9 (a) displays final deformation contours for a support column ($W_c=1.0$ mm) case. There is no deformation in the bottom region of the support column due to a fully constrained boundary condition. Top surface deformation plots from the $W_c=1.0$ mm case and the L=15 mm case have been compared. An expected deformation drop for the $W_c=1.0$ mm case can be noted as a result of the applied support column constraint, illustrated in Figure 7.9 (b).

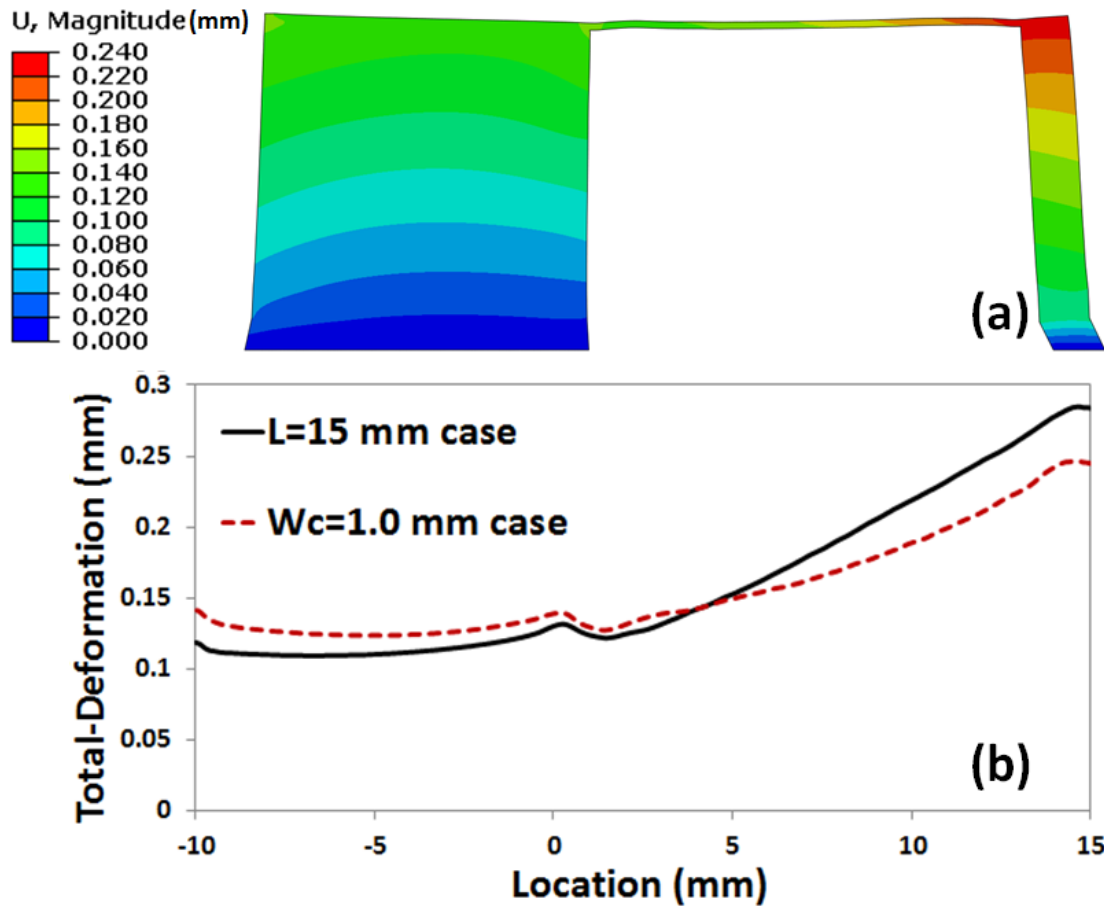


Figure 7.9. Typical example of deformation contours and top surface deformation plots after final cooling for $W_c=1.0$ mm case.

To reduce build cost, it is necessary to investigate the amount of material used in the support columns and the corresponding effect on warping reduction. In the 2D simulation, the amount of material used in support columns is proportional to the width of the column. The $W_c=0.5$ mm column width is considered the “base size” for future comparison, and the increment of support column material usage (column width) is set to be $1\times$ “base size” at a time in simulation. Top surface deformation plots, from simulated results of different amounts of support column material usage cases (W_c values), have been concluded in Figure 7.10. However, the deformation is barely changed even if a larger amount of materials have been used, e.g., $W_c=1.5$ mm case ($3\times$ “base size”) vs. $W_c=0.5$ mm case ($1\times$ “base size”). The results confirm that even a thin support column, which requires less material, could provide

mechanical constraint to prevent overhang curling. Thus, it is probably not necessary to spend a large amount of materials on building thick support columns.

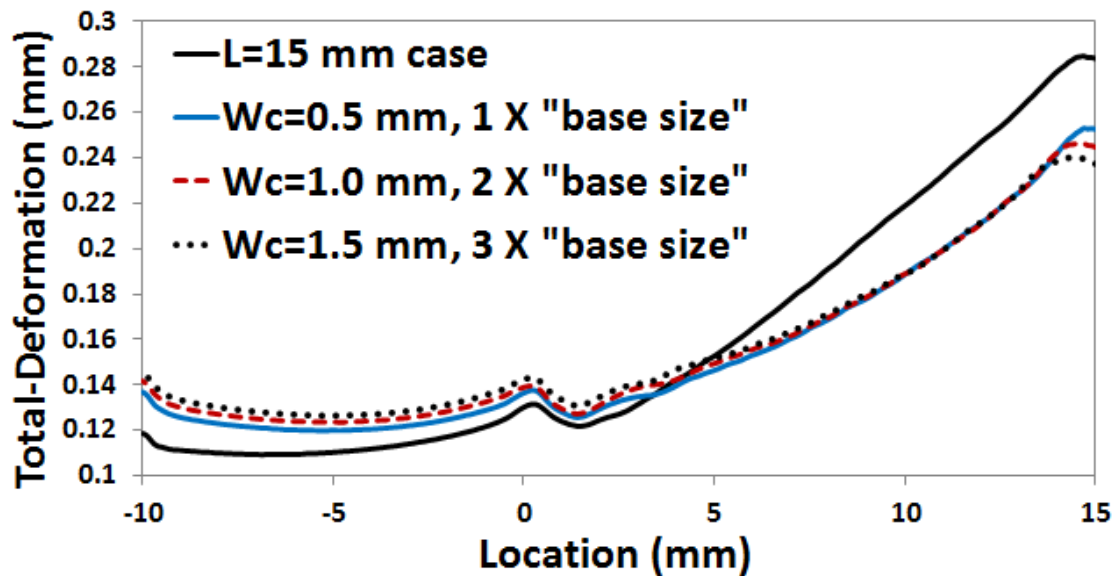
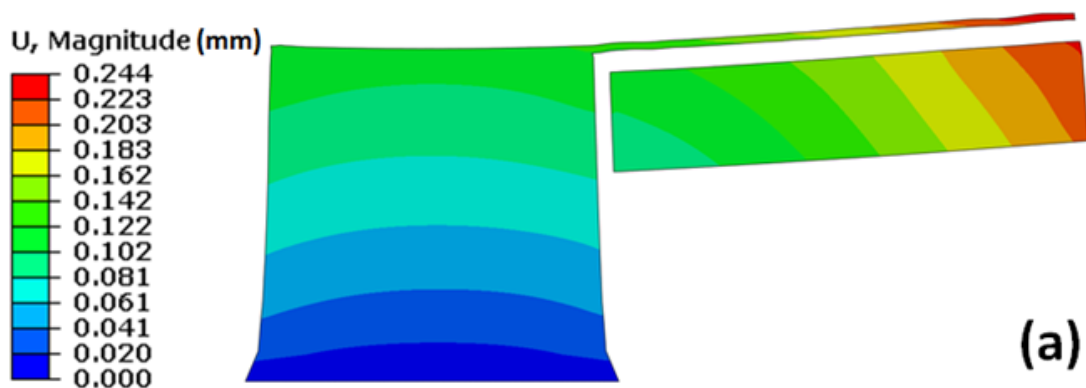


Figure 7.10. Simulation results comparison of different support column material usage cases (top surface deformation plots).

7.4.3 Solid Piece Gap Effect

Figure 7.11 presents a deformation contour after the final cooling for a solid piece (Gap = 0.63 mm) case. Although a solid piece has been inserted under the deposited top layers, the overhang area still has a larger deflection than the solid area, as shown in Figure 7.11 (a). However, a noticeable deformation drop, based on the top surface deformation information, can be observed in Figure 7.11 (b) when compared with the L=15 mm case. The inserted solid material in powder bed, with larger density and higher conductivity, can improve the effective thermal conductivity in the same heat affected region since the total energy input remains unchanged. Therefore, the solid piece would contribute to bring down the top surface temperature as well as the powder bed temperature. Temperature plots at different EBAM process steps have indicated that the solid piece can successfully reduce temperature, as shown in Figure 7.12. Figure 7.12 (a) shows temperature contours before the

start of layer-3 addition process, which is actually at the end of 10 seconds inter-layer cooling period between layer-2 and layer-3. The contours in the solid piece region shows a lower temperature than the corresponding region in the L=15 mm (no solid piece) case. The collected powder bed top surface temperature of the solid piece (Gap=0.63 mm) case is lower than that of the L=15 mm case as well. In the electron beam scanning/melting process (on layer-3), the powder bed temperature of the solid piece (Gap=0.63 mm) case is also lower than that of the L=15 mm case, as shown in Figure 7.12 (b). Figure 7.12 (c) indicates that the top layer surface temperature has been reduced by the solid piece in electron beam scanning process (on layer-3). Therefore, the minimization of deposited layers' max temperature and final cooling temperature (20 °C) by inserted solid piece can lead to final overhang deformation drop (i.e., $\alpha_e \times \Delta T$).



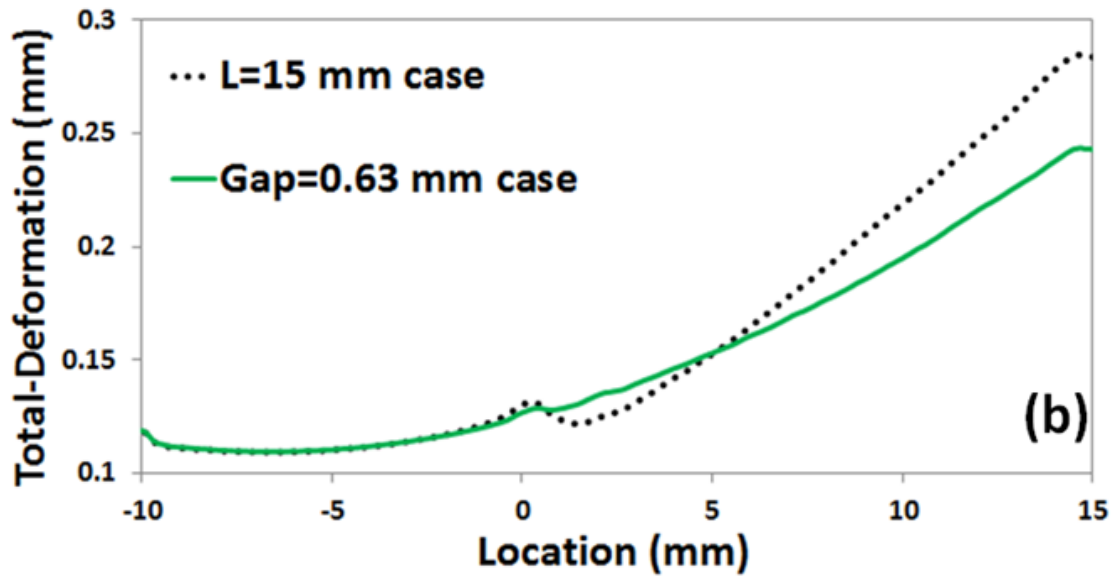
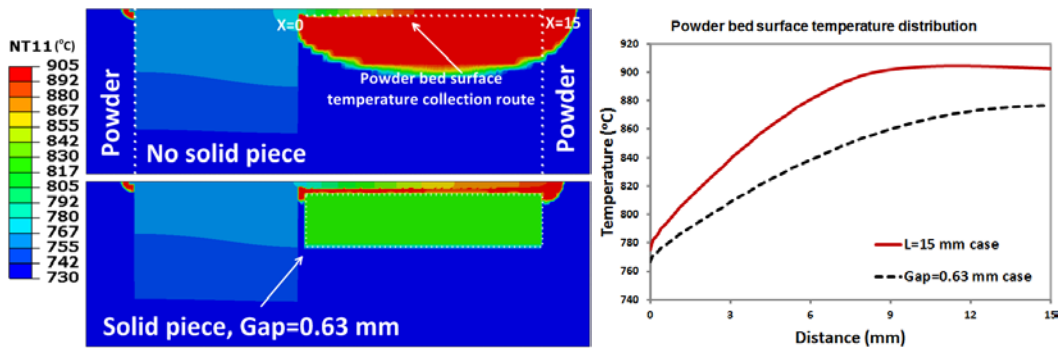
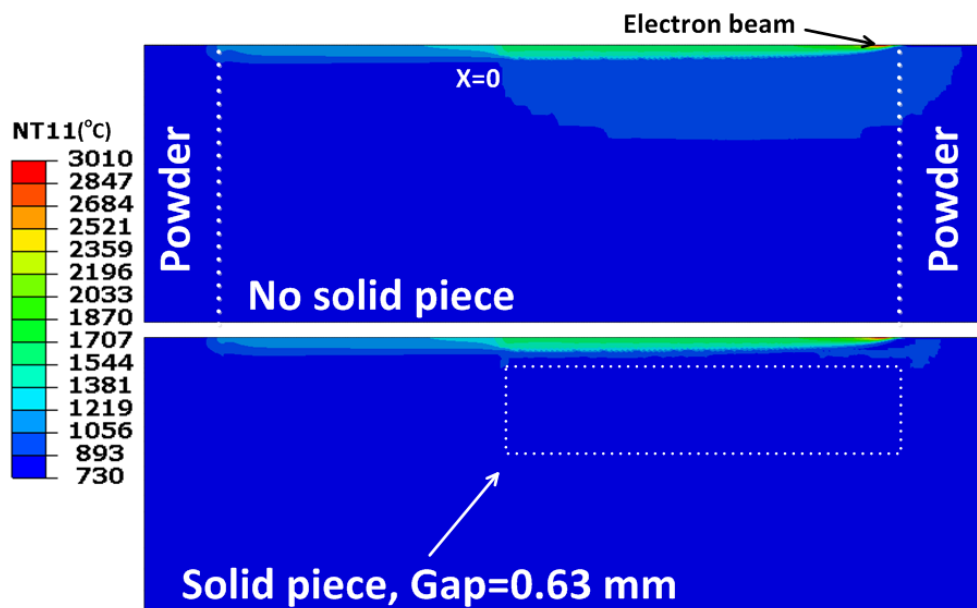


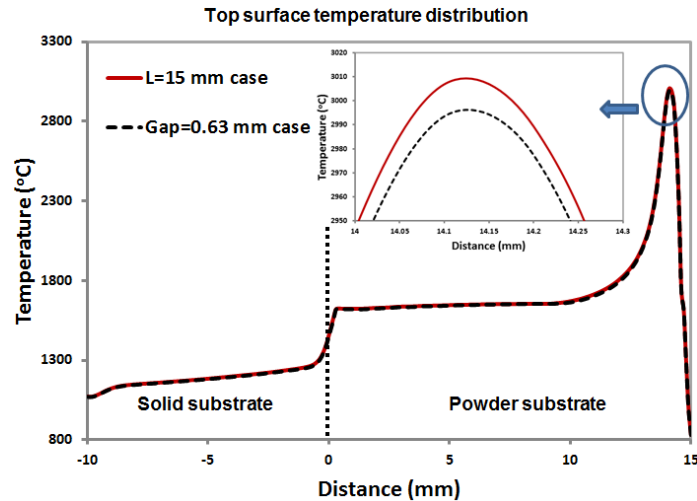
Figure 7.11. Typical example of deformation contours and top surface deformation plots after final cooling for Gap=0.63 mm case.



(a)



(b)



(c)

Figure 7.12. (a) Typical example of temperature plots (inter-cooling step between layer-2 and layer-3); (b) temperature contours (electron beam scanning on layer-3); (c) deposited layer top surface temperature profiles (electron beam scanning on layer-3).

It is also quite interesting to explore the effect of gap distance between the solid piece and deposited layers. The solid piece may have little effect on deformation reduction when a large gap distance is applied. The top surface deformation plot indicates that Gap = 6.3 mm case has a similar warping trend with no solid piece case (L = 15 mm case), noticed in Figure 7.13. On the other hand, the smallest warping is obtained when the solid piece is directly placed under deposited layers, which is the Gap = 0 mm case. The deformation plot of Gap = 0.63 mm case is between Gap = 0 and 6.3 mm cases. Therefore, it can be concluded that the gap effect on the overhang warping reduction will be effective when a small gap distance is applied, such as the Gap = 0.63 mm case based on the simulated results. However, the gap distance should be carefully decided since the solid piece can be melted and solidified together with top layers, when the depth of the melt pool is larger than the selected gap distance during the electron beam scanning process.

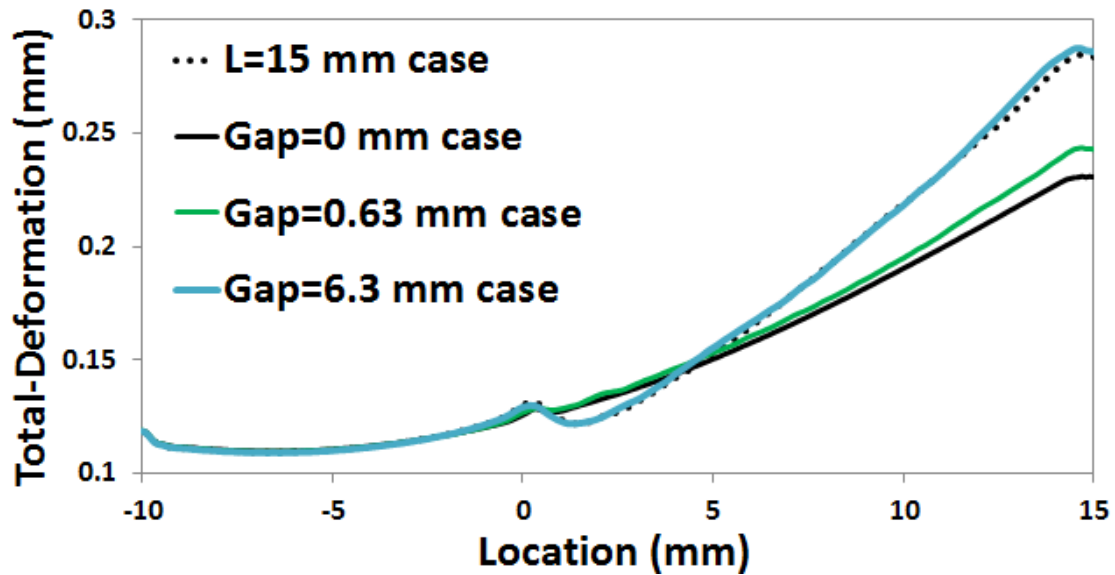


Figure 7.13. Simulation results comparison of different gap distance cases (top surface deformation plots).

7.5 Conclusion

In this study, a 2D thermomechanical model was developed for overhang and support structure studies in the EBAM process. The model incorporated a moving heat source with a Gaussian volumetric intensity, Ti-6Al-4V powder as well as solid material temperature dependent properties and latent heat of fusion, etc. The element activation method was used to simulate the layer addition process. A few geometric considerations of the overhang and support structures were investigated in fabricating overhang parts using EBAM. The major findings can be summarized as follows:

1. A thermomechanical code, FEM-based developed in this study, is able to simulate the deformation of overhang parts in EBAM. As expected, the overhang length affect the overhang deformation; the longer the overhang, the larger the deformation.

2. A solid column, as a traditional support structure means, can reduce and possibly eliminate the overhang warping; moreover, the size of the column may be minimized to reduce the amount of support materials, while meeting a deformation constraint.

3. In addition, using a solid piece beneath the overhang, a nontraditional approach, may also effectively reduce the overhang deformation. However, an appropriate gap distance needs to be analyzed in order to be effective for deformation reductions, while not fused to the overhang part.

The developed 2D model can only be used for the deformation trend prediction in the EBAM process due to a lack of experiment validation. Future study of this research will focus on the influence of powder material properties, e.g., size and porosity. In addition, the initial temperature for solid and powder substrate needs to be improved since a uniform temperature has been assigned for the two sections in this study. It is not clear whether the preheating temperature will be the same for solid/powder substrate when considering their different thermal properties, especially thermal conductivity.

Acknowledgements

This research is supported by NSF (CMMI 1335481), and is in collaboration with Marshall Space Flight Center (MSFC), Advanced Manufacturing Team. The first author also acknowledges the scholarship support from the Alabama EPSCoR Graduate Research Scholars Program.

References

- Biamino, S., Penna, A., Ackelid, U., Sabbadini, S., Tassa, O., Fino, P., Badini, C. (2011). Electron beam melting of Ti-48Al-2Cr-2Nb alloy: Microstructure and mechanical properties investigation. *Intermetallics*, 19(6), 776-781.
- Cormier, D., Harrysson, O., & West, H. (2004). Characterization of H13 steel produced via electron beam melting. 14th Annual Solid Freeform Fabrication Symposium, University of Texas, Austin, Texas, 4-6 August 2003.
- Gaytan, S. M., Murr, L. E., Martinez, E., Martinez, J. L., MacHado, B. I., Ramirez, D. A., Wicker, R. B. (2010). Comparison of microstructures and mechanical properties for

solid and mesh cobalt-base alloy prototypes fabricated by electron beam melting. *Metallurgical and Materials Transactions A: Physical Metallurgy and Materials Science*, 41(12), 3216-3227.

Gaytan, S. M., Murr, L. E., Medina, F., Martinez, E., Lopez, M. I., & Wicker, R. B. (2009). Advanced metal powder based manufacturing of complex components by electron beam melting. *Materials Technology*, 24, 180-190.

Gong, X., Anderson, T., & Chou, K. (2012). Review on Powder-Based Electron Beam Additive Manufacturing Technology. *ASME/ISCIE 2012 International Symposium on Flexible Automation*, St. Louis, MO, June 18-20, 2012, ISFA2012-7256.

Jhabvala, J., Boillat, E., André, C., & Glardon, R. (2012). An innovative method to build support structures with a pulsed laser in the selective laser melting process. *The International Journal of Advanced Manufacturing Technology*, 59(1-4), 137-142.

Marimuthu, S., Eghlio, R., Pinkerton, A., & Li, L. (2013). Coupled Computational Fluid Dynamic and Finite Element Multiphase Modeling of Laser Weld Bead Geometry Formation and Joint Strengths. *Journal of Manufacturing Science and Engineering*, 135(1), 011004.

Materialise software. Available from: <http://software.materialise.com/magics-0>. Software for Additive Manufacturing, Materialise. Accessed June, 2012.

Mercelis, P., & Kruth, J.-P. (2006). Residual stresses in selective laser sintering and selective laser melting. *Rapid Prototyping Journal*, 12(5), 254-265.

Murr, L., Esquivel, E., Quinones, S., Gaytan, S., Lopez, M., Martinez, E., Martinez, J. (2009). Microstructures and mechanical properties of electron beam-rapid manufactured Ti-6Al-4V biomedical prototypes compared to wrought Ti-6Al-4V. *Materials Characterization*, 60(2), 96-105.

Murr, L., Martinez, E., Gaytan, S., Ramirez, D., Machado, B., Shindo, P., Ciscel, D. (2011). Microstructural architecture, microstructures, and mechanical properties for a nickel-base superalloy fabricated by electron beam melting. *Metallurgical and Materials Transactions A*, 42(11), 3491-3508.

Parthasarathy, J., Starly, B., Raman, S., & Christensen, A. (2010). Mechanical evaluation of porous titanium (Ti6Al4V) structures with electron beam melting (EBM). *Journal of the mechanical behavior of biomedical materials*, 3(3), 249-259.

Ramirez, D. A., Murr, L. E., Martinez, E., Hernandez, D. H., Martinez, J. L., Machado, B. I., Wicker, R. B. (2011). Novel precipitate-microstructural architecture developed in the fabrication of solid copper components by additive manufacturing using electron

beam melting. *Acta Materialia*, 59(10), 4088-4099.

- Sabbadini, S., Tassa, O., Gennaro, P., & Ackelid, U. (2010). Additive manufacturing of gamma titanium aluminide parts by electron beam melting. TMS 2010 - 139th Annual Meeting and Exhibition, February 14, 2010 - February 18, 2010, Seattle, WA, United states.
- Vora, P., Stapleton, D., Kamran, M., Derguti, F., Todd, I., & Hopkinson, N. (2012). Benchmarking Metal Powder Bed Additive Manufacturing Processes (SLM and EBM) to Build Flat Overhanging Geometries Without Supports. 23rd Annual International Solid Freeform Fabrication Symposium - An Additive Manufacturing Conference, , Austin, TX, USA, August 6-8, 2012.
- Yan, C., Hao, L., Hussein, A., & Raymont, D. (2012). Evaluations of cellular lattice structures manufactured using selective laser melting. *International Journal of Machine Tools and Manufacture*, 62, 32-38.
- Yu, P., Qian, M., Tomus, D., Brice, C. A., Schaffer, G. B., & Muddle, B. C. (2009). Electron beam processing of aluminium alloys. *Materials Science Forum*. Trans Tech Publications.

CHAPTER 8

SUPPORT STRUCTURE DESIGN FOR OVERHANG FABRICATION IN ELECTRON BEAM ADDITIVE MANUFACTURING

Abstract

Overhang structures are commonly found in Powder-bed metal additive manufacturing (AM) such as electron beam additive manufacturing (EBAM) process. The EBAM is assumed to build overhang structure without support features since powder bed could provide support. However, heat dissipation difference by sintered powder and solid substrate for overhang feature actually causes severe part distortion and requires support structure. Current support generation methods usually used certain types of structure to cover the overhang space. They may overestimate the support volume or put a large amount of supports, which could not be necessary and increase the post process time. Thus, the object of this task is to enhance the performance and efficient usage of the EBAM technology through effective support structure designs. In this study, a combined heat support and support anchor design method has been proposed. Numerical model has been used to evaluate stress and deformation during the design process. The detailed design process has been presented for a typical overhang and the simulation results have indicated that overhang deformation can be greatly reduced using this new method.

8.1 Introduction

Powder-bed electron beam additive manufacturing (EBAM) is a relatively new Additive manufacturing (AM) technology that a physical part is produced directly from model geometric digital information. In such a process, high-energy electron beam heat sources was utilized to fabricate metallic parts, by sintering and/or melting metal powders in a layer-by-layer fashion. Thus EBAM can offer many manufacturing advantages and be capable of making full-density complex metallic parts. In recent years, EBAM enjoyed increased usage in many industrial fields such as aerospace and medical fields due to aforementioned advantages.

EBAM still exhibits several process/part deficiencies such as layer delamination and distortion, especially for overhang configurations. The nature of overhang configuration is that one portion of the structure is built upon powder substrate while another portion is built upon solid substrate. It is believed that significantly different heat transfer ability caused by thermal properties difference between powder and solid material may lead to distortion difference. Experimental method has been widely used to reduce the warping defect in overhang. Hussein et al (Hussein *et al.*, 2013) have tested volume fraction of lattice structure effect on overhang structure in SLM. Their experimental results have revealed that it was possible to manufacture gyroid lattice structures with overhang deformation prevention with 8% of relative volume, which means 92% of loose powders can be removed. Different support structure could be found in literature (Calignano, 2014). In these support structures, a point support is used for very small features, a web support can be used for circular areas and a line support is suitable for narrow down facing areas. Contour support is used to better

sustain the contours of the parts in metal sintering. Thomas (Thomas, 2009) experimentally demonstrated that overhang part would occur curling when the raster scan vector was perpendicular to the curling while deformation would be small when scan vector was along the curling. Cloots et al (Cloots *et al.*) developed and experimentally fabricated special lattice support that fixation points was used to connect lattice support with the part and grid structure was used for support rigidity. The horizontal and vertical forces can be absorbed by the crossbars.

It is well known that the support structures under overhang layers may provide mechanical constraint for preventing part warping. However, the support removal process can be a high-cost, labor-intensive and time-consuming job. Vora et al (Vora *et al.*, 2015) have utilized ASLM method (anchorless selective laser melting) to eliminate the usage of typical support. The detail of ASLM method is that ASLM locally melts two or more powdered materials that alloy under the action of the laser and can form into various combinations of eutectic/hypo/hyper eutectic alloys with a new lower solidification temperature. This new alloy is maintained in a semi-solid or stress reduced state throughout the build with the assistance of elevated powder bed preheating. In such a process they could build part free of distortion. However, it is not able to reduce overhang deformation using one material.

In most additive manufacturing techniques, support structures are needed for overhangs and they mainly have three advantages (Jhabvala *et al.*, 2012): (1) avoid the collapse or deformation of overhang due to gravity during building process; (2) avoid the destruction caused by the powder deposition system such as blade or hopper; (3) avoid local fusion and withstand residual stresses. However, there are also problems about support

structures (Jhabvala *et al.*, 2012): (1) extra time and material are needed to build, which would be costive for some expensive materials; (2) support structure generation requires more actions in CAD design. Commercial software may be capable of creating support structures, but they are not efficient for complex shapes; (3) post process is needed after part being built, which is often time-consuming and labor intense.

Thus, the question is how to generate support structure so as to reduce disadvantages while taking its advantages. Evaluating overhang thermal effects on the part thermomechanical behaviors in EBAM and correlate with warping severity is necessary. In addition, investigation of different designed support patterns to evaluate the effectiveness of a designed support is also needed. The thorough understanding of thermal as well as deformation phenomenon during overhang building process is a good way for the optimization of overhang part. Although experimental study could provide useful information about overhang deformation, it is not able to provide transient process temperature and related stress information which are main cause of part deformation. In addition, experiments are always costive and time consuming. Alternatively, numerical simulation provides a cost effective choice to study part overhang thermomechanical responses under different support considerations. There are limited literatures on the study of thermomechanical process of overhang structure in EBAM process. Cheng and Chou (Cheng and Chou, 2014) developed a novel coupled 2D thermomechanical finite element model to simulate the transient heat transfer, part distortion and residual stresses of overhang part during EBAM process. They have found that high energy density would cause larger overhang deformation.

The object of this task is to enhance the performance and efficient usage of the powder bed technology through effective support structure designs. Currently support generation mainly depends on user experience and simply fulfills overhang with support structures. The thermomechanical process during the overhang building process is not considered in the support generation process. The thermal stress field of overhang may be ignored in the design process, which is critical to final deformation or even part crack. Thus, traditional methods may overestimate the column thickness or put a large amount of columns, which could not be necessary and increase the post process time. In this task, it is going to solve some common questions: (1) On what basis the design rule is proposed? (2) Where the support is needed?

8.2 Support Structure Design Framework

The support structure design framework consists of two categories of algorithms: non-contact heat support design and support anchor design. An effective heat support design requires fundamental understanding of the warp generation in powder bed overhang fabrication process. It has been investigated in previous chapter that the heat dissipation capability difference between powder substrate and solid substrate could contribute to the overhang deformation, since powder material is less effective in heat transfer process when compared to solidified material. Thus, serious distortion defects could be caused under the repeated heating/cooling cycles and the cumulative warped deposited layers. This effect is quite obvious in the first few layers upon overhang region. Therefore, a contact free solid heat support, fabricated by the same material under the overhang region, can be applied to

increase powder bed heat dissipation ability. The reduced temperature in region upon powder bed could apparently reduce overhang deformation.

On the other hand, In order to prevent part deformation from mechanical point of view, the support structure is needed to constrain the warping defect in the first few layers. Current support designs usually based on uniform design approach, the method uses certain types of structure to duplicate or pattern in all directions to fill the overhang region. In this study, a flexible support anchor distribution method is used to generate support based on overhang stress distribution. Thermal stress is a critical factor which is directly correlated to part deformation; it may be used as a rule to determine where support structures are necessary. Thus, the basic idea is to apply dense supports on high stress region while sparse supports on low stress region, as shown in Figure 8.1.

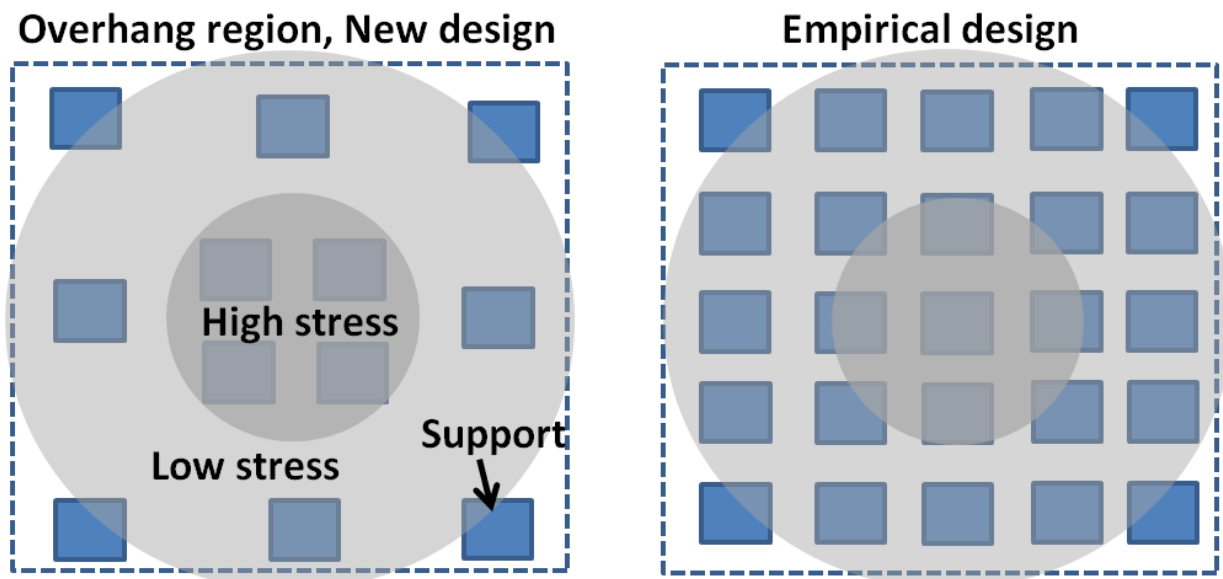


Figure 8.1. General idea of stress related support distribution.

An energy function $E(V)$ can be used for support determination and placement (Chen, 2007). Moreover, the continuous stress map $f(\sigma)$ of overhang area can be used as a guideline for support anchor arrangement in overhang region. When the support anchor v^j is planned to

be added around existing anchor v^i in the overhang region, the location of v^j should be mapped and calculated based on $f(\sigma)$ to a location which may match specific requirement. The function $f(\sigma)$ is defined as discrete values imported from finite element thermomechanical analysis result (Chen, 2007). The addition procedure of support anchors starts with inputting the vertices to new locations so that the distance $|\vec{v}^j - \vec{v}^i|$ between two grid vertices v^i and v^j is approximately inversely proportional to the $f(\sigma)$ distribution. Thus, the problem can be concluded as a minimum energy problem. The support anchors can be arranged by minimizing an adjusted energy function $E(V)$ which is defined as:

$$E_v^j = \min_{j \in \emptyset} [f(\sigma)]^i [f(bias)]^j |\vec{v}^j - \vec{v}^i|^2 \quad (14)$$

$$f(bias) = X_{\vec{v}^j} / L_{overhang}$$

where v^j is in the neighboring grids of v^i in space \emptyset (overhang region). $X_{\vec{v}^j}$ is the x-direction distance to overhang edge for v^j , $L_{overhang}$ is the overhang length.

Satisfy:

$$(1) \text{ Anchor stress criteria: } \sigma_{i,j,\dots} \leq \sigma_{allowable}$$

$$(2) \text{ Deformation convergence criteria: } |U_k - U_{k-1}| \leq \delta_{allowable}$$

8.3 Simulation Based Support Structure Design Procedure

Finite element model has been utilized to simulate EBAM overhang deposition since the design process requires stress and deformation information, while the experimental method is not able to capture the real time response. Figure 8.2 shows the flow chart of support structure design optimization process. The heat support will be applied first since the non-contact support structure requires no post-process. The gap between solid piece and solidified layers should be carefully selected to avoid fusion problem with deposited layers,

since the purpose of inserted solid piece heat support is to increase powder bed heat dissipation ability. The thermal simulation of the first layer above the region will be used to extract the melt pool depth information; the selected gap distance value will be larger than max melt depth value. If mechanical tool is needed in the post process, the gap value should also consider the minimum space requirement for the proper operation of mechanical tool. Iterative thermomechanical simulation will be conducted to determine an appropriate heat support thickness after the determination of gap distance to reduce material usage. The criterion of ending iteration is that (1) the deformation difference between overhang configuration and all solid substrate configuration cases is in acceptable tolerance, e.g., $\delta_{allowable}$; or (2) the overhang deformation difference between k-1 step and k step is in defined tolerance, e.g., δ_{range} . There are four conditions in this step: (A) if criteria (1) is matched while criteria (2) is not matched at step k, the procedure will be stopped and exited with the returning of step k-1 support design parameters (e.g., heat support thickness); (B) if criteria (1) is not matched while criteria (2) is matched at step k, the iteration will be continued; (C) if criteria (1) is not matched while criteria (2) is also not matched at step k, the support design parameters of step k-1 will be used for next stage support design simulation; (D) if both criteria (1) and (2) are matched, the iteration will be continued.

If the design process matches condition (C), the next stage of support anchor design based on designed heat support will be initiated. An empirical anchor width will be set and empirical support anchor arrangement will be applied to obtain initial stress and deformation results. Then design criterion examination will be conducted: (1) The obtained anchor stress will be checked with maximum allowable stress at specific temperature, e.g., $\sigma_{allowable}$; (2)

overhang deformation is in acceptable tolerance with that of solid substrate case, e.g., $\delta_{allowable}$. If the obtained anchor stress and deformation have been calculated to be in the tolerance range, the design information of this step will be recorded and next iteration will begin by reducing the anchor width. The total column volumes will be compared between different iterations and the design information of smallest anchor volume case will be recorded and returned. If the initially obtained stress and deformation have exceeded required tolerance, additional support anchors will be add to the overhang region based on minimum energy method. The iteration continues until the overhang warping and support anchor stress exceeds the deformation and stress criteria. Then the total anchor volume of current iteration will be compared with that of previous iteration. If the volume is smaller than that of previous iteration, the simulation will begin another round of iteration with reduced anchor width. The final goal is to obtain appropriate support with less material usage.

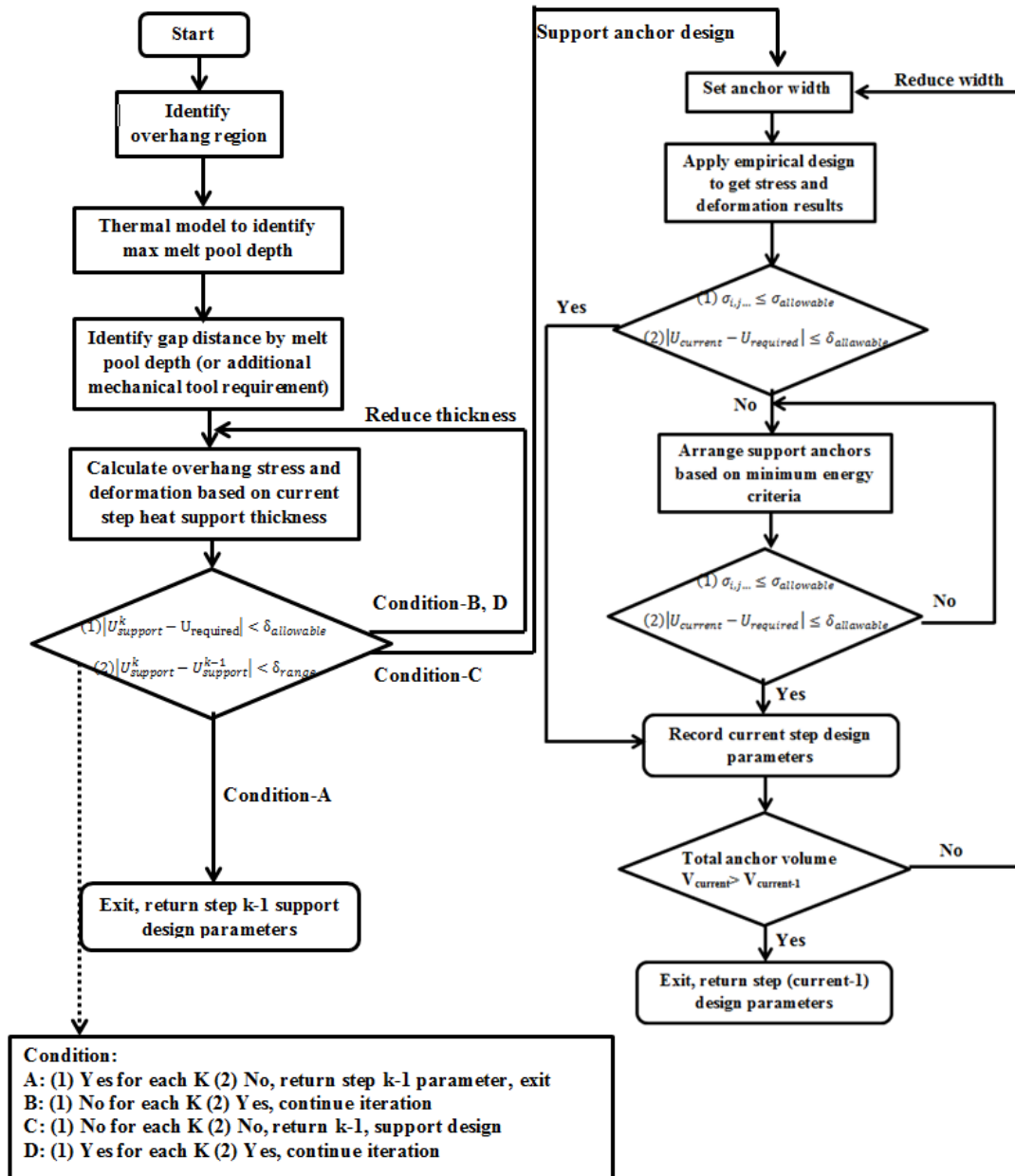


Figure 8.2. Overhang support design flow chart.

8.4 Finite Element Model Configuration

A sequentially coupled 3D FEM thermomechanical model, developed in Chapter 6, was utilized to simulate the overhang stress and deformation in EBAM. In this study, the beam scanning affected region had a length of 14 mm and a width of 6 mm on the top powder layer. The model was consisted of a solid substrate placed in powder bed with overall dimensions of 20 mm × 12 mm × 10 mm in (x, y, z). The solid substrate size is 2 mm × 6

mm × 10 mm in (x, y, z) surrounded by powders. Three powder layers will be deposited sequentially. A cross sectional scanning method will be applied on the top powder layers. Generally, the current beam scanning direction will be perpendicular to that of previous layer. The material used in the simulation was Ti-6Al-4V. The process parameters have been set to be 1000 mm/s beam speed, 0.4 mm beam diameter and 4.5 mA beam current. A triangular shaped region above powder substrate was defined in the model to represent general overhang structure. The 3D simulation model is presented in Figure 8.3. A typical thermal simulation took around 100 hours while mechanical analysis took about another 150 hours using two Inter(R) Xeon(R) E5 CPUs.

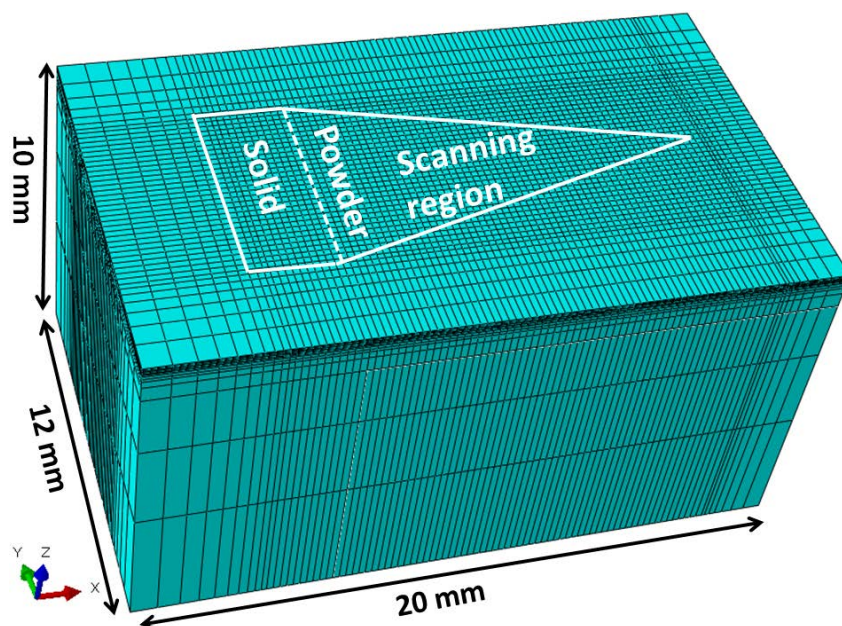


Figure 8.3. Model meshing and geometrical information.

8.5 Results and Discussion

8.5.1 Typical Process for Heat Support Design

It has been found that heat support (solid piece) in powder bed beneath overhang can improve the heat dissipation rate so as to bring down overhang deformation in Chapter 7. However, the amount of used heat support material should be carefully decided so as to

reduce material consumption and keep reasonable deformation tolerance. In this study, the material usage is controlled by heat support thickness. Three simulation cases have been conducted to illustrate heat support thickness decision process. Case (A) is a typical overhang case without any support structure; case (B) is 3 mm thick heat support case; case (C) is 0.8 mm thick heat support case. There is another all solid substrate (no overhang) case, label as case (D), used for comparison purpose. The gap distance has been decided to be 0.21 mm since the melt pool depth is about 0.15 mm when electron beam traveled upon the first layer for given process parameters. There is also a 0.6 mm distance between heat support and solid substrate to avoid rigid connection. Figure 8.4 shows the general configurations of the three overhang structures as well as the build direction deformation which has been collected after the whole model cooled down to room temperature.

It has been noticed that case (B) with 3 mm heat support thickness can successfully reduce deformation when compared with case (A) which has no support. However, case (C) with 0.8 mm heat support thickness can also achieve almost the same deformation reduction result. A comparison between 3 deformation profiles along center path of beam scanning area has shown that case (B) and case (C) has a quite close deformation profile while they are both smaller than case (A); they are all much larger than that of solid substrate case. The two cases, case (B) and case (C), have indicated that the material usage (volume) of the heat support could be reduced while having little (tolerable) impact to its effectiveness such as distortion reduction or heat dissipation efficiency. Therefore, a user defined tolerance value could be used to control the material usage of the heat support. If the deformation difference between (current-1) step and current step is in defined tolerance range, the heat support

thickness will continue to be reduced. It is obvious that if a tolerance value of 0.01 mm has been used for current simulated cases in Figure 8.4, further reduction process of heat support thickness maybe needed. For demonstration purpose, the tolerance value of 0.007 mm is used, thus the iteration process will end up with a thickness of 0.8 mm. If the overall deformation is in a reasonable tolerance range when compared with all solid substrate case (D), the support design process will stop. However, a noticeable deformation can still be observed for overhang region after the application of heat support, as shown in Figure 8.4, the next step for support design process will be initiated.

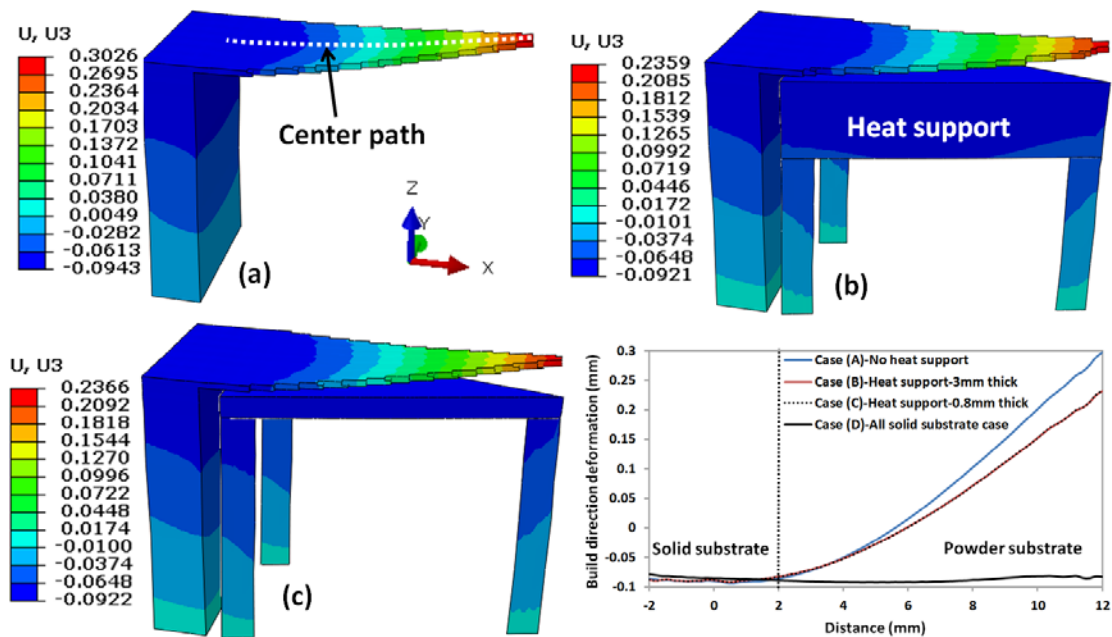


Figure 8.4. Deformation comparison of heat support cases and non-heat support case.

8.5.2 Typical Process for Anchor Support Design

The anchor support design will begin once the heat support design could not meet design requirement. In this study, the 0.8 mm heat support case has been used in support anchor design step. It has been observed that the deformation of the first layer, after cooling to preheating temperature, have a very important influence on the subsequent layer addition

and deformation. Simulation results indicate that the deformation of the first layer has a significantly contribution to the final deformation for the 0.8 mm heat support thickness case, as shown in Figure 8.5. Thus, the deformation of the first layer will be used for comparison and stress information extraction purpose.

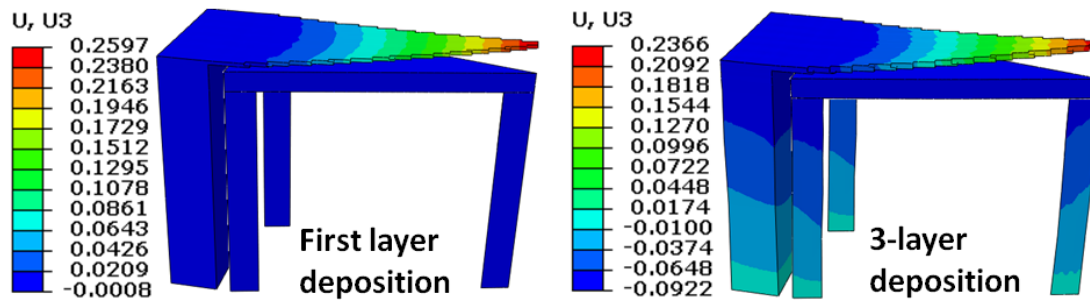


Figure 8.5. Deformation comparison between first layer (cooled to preheating temperature) and all 3 layer deposition (cooled down to room temperature).

Empirical support anchor design will be applied first to obtain stress and deformation information, the initial anchor size is user-defined, e.g., width=0.4 mm in this study. Thus, one support anchor with 0.4 mm width has been applied under the tip region of the overhang, as shown in Figure 8.6. A comparison between the two cases, with and without anchor support, has shown that even a small anchor can significantly reduce the deformation, as shown in Figure 8.6. The max deflection difference in build direction is about 0.018 mm when compared with all solid substrate case. The anchor thermal stress is also below the allowable value (plastic value at current temperature). Additional support anchor may be needed if the first round of support anchor application can not bring down the maximum deformation to tolerable range. There are plenty of locations to place additional columns in high stress concentration region. The location which gives minimum $E(v)$ will be selected for additional anchor placement. Let $f(\sigma) > 200$ MPa (maximum stress value from stress contour), the location with similar $f(\sigma)$ value have been examined, the coordinates of these locations

can be obtained. It can be seen that there are multiple positions which match $f(\sigma)$ value, as shown in Figure 8.7. Then the distance between $v1$ and $v2$ can be calculated, e.g., the distance for $v1$ and $v2-i$ ($i=1, 2, \dots$). Obviously, location $v2-1$ in Figure 8.7 (a), which gives the min $E(v)$, will be used to place the second anchor. The deformation results in Figure 8.7 (b) indicated that the application of second anchor could help to further reduce overhang warping. The max deformation difference, when compared with all solid substrate case, is about ~ 0.014 mm.

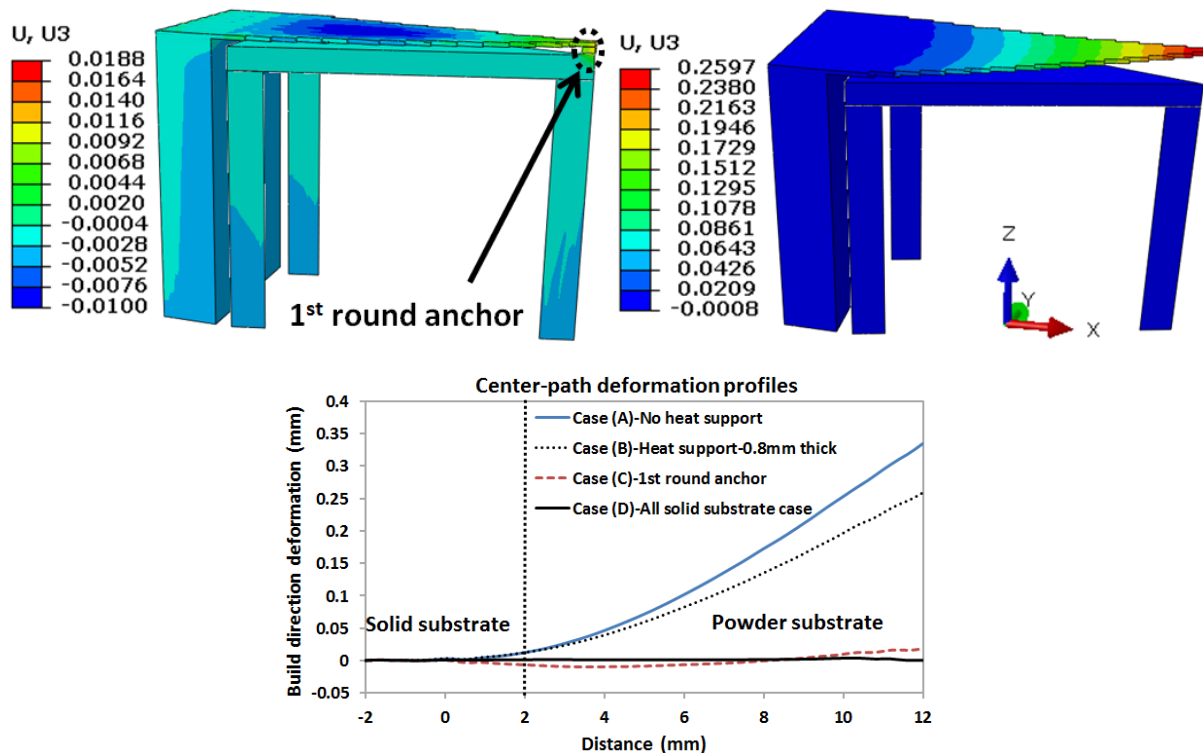


Figure 8.6. Empirical design of initial (1st round) support anchor, and deformation comparison after first layer deposition between with/without anchor support cases.

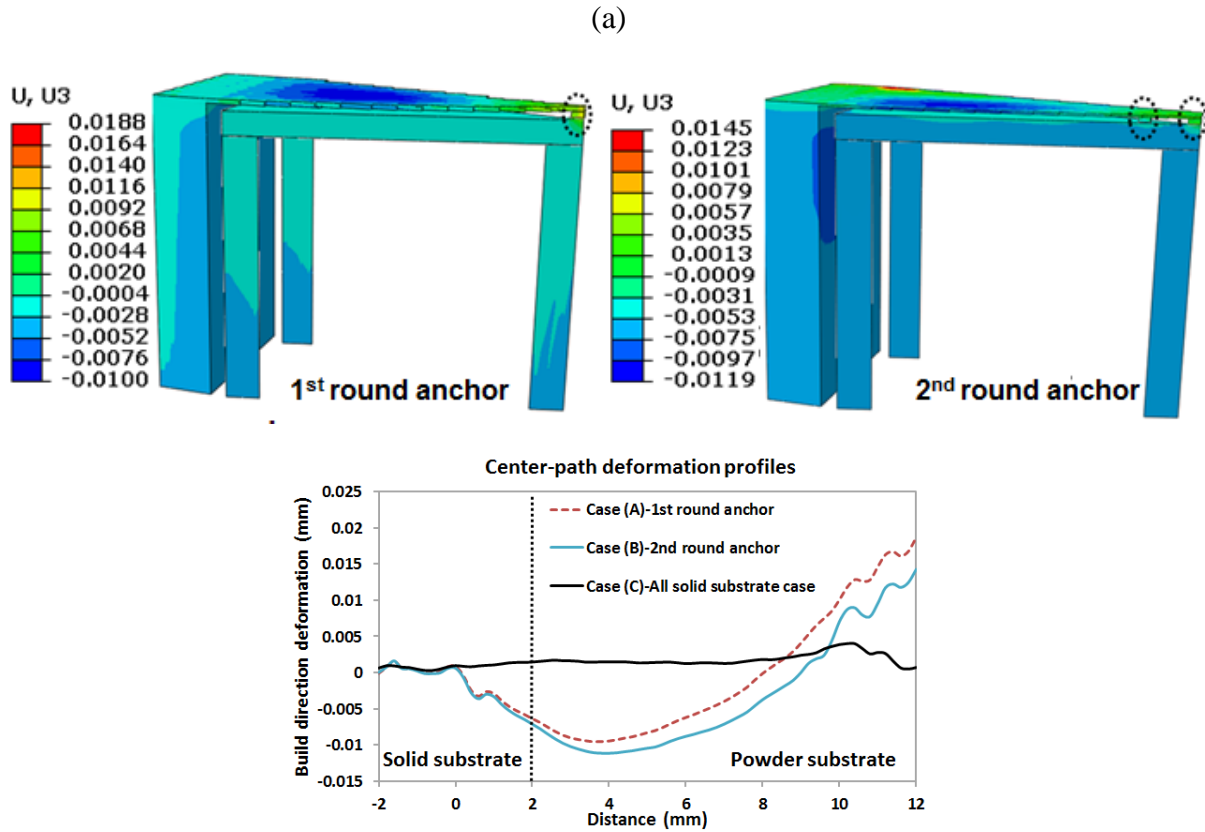


Figure 8.7. Second round support anchor application.

To further reduce the deformation, third round of anchor design is conducted. In the anchor application process, if there are multiple locations which may result in the same distance, they will be determined by the $f(bias)$ function which is acted as an anchor location selector. The idea of this function is to push possible anchors to be close to the overhang edge for easy removal purpose. For example, there are two locations, $v3-1$ and $v3-2$ in Figure 8.8 (a), match the $\max f(\sigma)$ requirement. The distance is the same for $(v2, v3-1)$ and $(v2, v3-2)$. Both locations will be selected since they have similar distance to overhang edge. After the application of each additional anchor, it has been observed that max difference (compared with all solid substrate case) is reduced to ~ 0.012 mm. Again, after the application of anchors, stress and deformation criteria check will be conducted based on simulation results. If

either of the criteria is matched, the procedure will continue; otherwise the iteration will stop and return the design parameters. In order to reduce the material usage for support anchor, another round of anchor design will be initiated with smaller anchor width. The anchor parameters such as width value and location information, which give minimum material usage while matching design criteria, will be adopted.

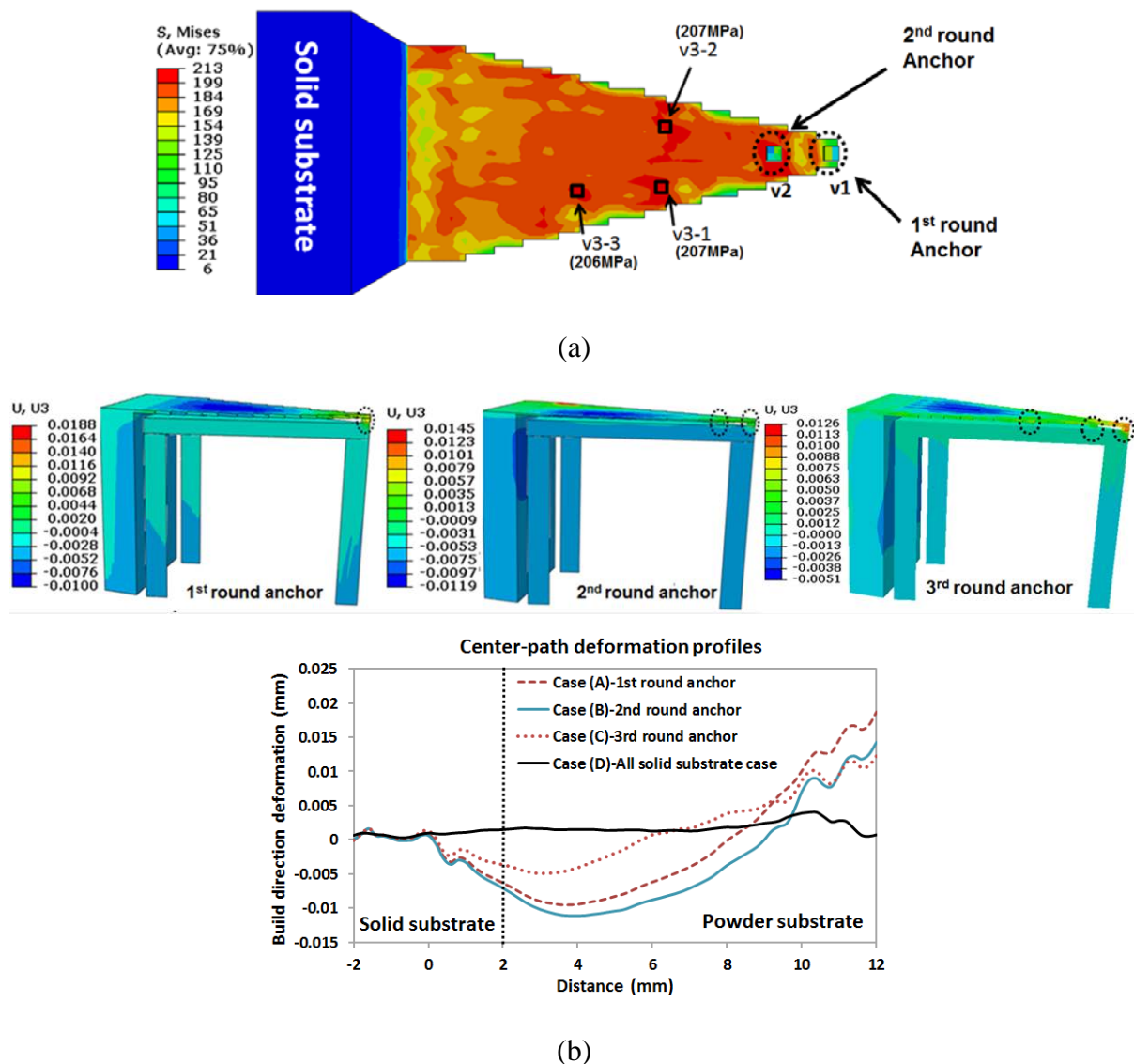


Figure 8.8. Third round support anchor application.

8.6 Conclusion

In this study, a 3D sequentially coupled thermomechanical model, using finite element method, was utilized for EBAM process overhang fabrication support design simulation. A general framework for overhang support structure design and optimization has been developed. The support structure design problem is formulated using the combined effective heat dissipation method and minimum energy method. Finite element simulation was used to determine heat support material usage and to search for locations where a support anchor is required. The developed support design method can be used for general powder bed overhang support design.

References

- Calignano, F. (2014). Design optimization of supports for overhanging structures in aluminum and titanium alloys by selective laser melting. *Materials & Design*, 64, 203-213.
- Chen, Y. (2007). 3d texture mapping for rapid manufacturing. *Computer-Aided Design and Applications*, 4(6), 761-771.
- Cheng, B., & Chou, K. (2014). Thermal Stresses Associated with Part Overhang Geometry in Electron Beam Additive Manufacturing: Process Parameter Effects. 25th Annual International Solid Freeform Fabrication Symposium - An Additive Manufacturing Conference, Austin, TX, USA, August 4-6, 2014.
- Cloots, M., Spierings, A., & Wegener, K. Assessing new support minimizing strategies for the additive manufacturing technology SLM. 24th Annual International Solid Freeform Fabrication Symposium - An Additive Manufacturing Conference, Austin, TX, USA, August 12-14, 2013.
- Hussein, A., Hao, L., Yan, C., Everson, R., & Young, P. (2013). Advanced lattice support structures for metal additive manufacturing. *Journal of Materials Processing Technology*, 213(7), 1019-1026.
- Jhabvala, J., Boillat, E., André, C., & Glardon, R. (2012). An innovative method to build support structures with a pulsed laser in the selective laser melting process. *The International Journal of Advanced Manufacturing Technology*, 59(1-4), 137-142.

Thomas, D. (2009). The development of design rules for selective laser melting. Ph.D. thesis, University of Wales, UK.

Vora, P., Mumtaz, K., Todd, I., & Hopkinson, N. (2015). AlSi12 in-situ alloy formation and residual stress reduction using anchorless selective laser melting. *Additive Manufacturing*, 7, 12-19.

CHAPTER 9

CONCLUSIONS AND RECOMMENDATIONS FOR FUTURE RESEARCH

9.1 Conclusions

Powder-bed beam based additive manufacturing technology fabricates metal parts by utilizing high energy beam to fuse metallic powder particles along cross sectional contours in a layer-by-layer fashion. Engineering components with complex geometry and internal features can be built in such a process. However, the complicated thermomechanical fabrication process makes the build parts have defects such as dimensional inaccuracy, quality inconsistency or even part failure. Thus, fundamental understanding of the process physics such thermal characteristics is critical to achieve the desired part properties. The goal of this research is to have fundamental understanding of the process physics, such as thermal characteristics and mechanical responses which are critical to achieve the desired part properties. Toward this end, numerical approach had been utilized to achieve these objectives. The major findings are summarized as follows.

(1) The thermal conductivity of Ti-6Al-4V powder is porosity dependent, and much smaller than solid sample. It was found to be critical for temperature predictions in EBAM process. At a beam speed of 632.6 mm/s to 728 mm/s, a beam current of 6.7 mA to 7.2 mA, and a diameter of 0.55 mm, it was noted that the maximum process temperatures were around 2700 °C, and the melt pools were around $2.94 \times 1.09 \times 0.12$ mm (length \times width \times depth). In addition, the simulated results have indicated that powder porosity is critical to the thermal

characteristics. The increase of the powder porosity can result in the increase of the melt pool size as well as peak temperature.

(2) The setting of speed function in EBAM machine would strongly affect the build part quality surface morphology; a higher SF could produce parts of rougher surfaces with more pore features. Both the experimental measurements and simulations indicated that the increase of the beam speed could reduce the peak temperatures as well as melt pool sizes. It has been noted that the peak temperature is 2572 °C and the melt pool length and width are 2.35 mm and 0.93 mm at a lower beam speed of 482 mm/s. On the other hand, at a higher beam speed of 1595 mm/s, the peak temperature and the melt pool length and width are 2326 °C, 1.25 mm and 0.82 mm, respectively.

(3) The thermal model was applied for SLM process simulation. The results showed the residual heat could significantly affect the melt pool size during raster scan. Larger melt pool dimensions would be observed in subsequent scanning path in raster scanning process. The melt pool evolution was found to be affected by beam process parameters. It was noted that, under given process parameters, the increase of beam power and decrease of beam speed could increase the beam traveling distance for a full melt pool evolution.

(4) The results of overhang thermomechanical simulation showed that the lower thermal conductivity of powder could result in higher temperatures and poor heat dissipation in overhang areas. Noticeable overhang deformation would also be caused by the retained higher temperatures. It is also found that a smaller porosity (e.g., 50% vs. 35%), which may be caused by higher preheating temperature, could reduce the process temperatures, residual

stresses and final part deformation in overhang region due to increased powder bed packing density and thermal conductivity.

(5) Three different geometric considerations of the overhang have been studied by a 2D thermomechanical model. It was found that the overhang length can affect the overhang deformation as expected; a longer overhang would have larger the deformation. The overhang warping could be eliminated by traditional solid column type supports but require time-consuming post-process to be removed. The size of the column may be minimized to reduce the amount of support materials while meeting a deformation constraint. The overhang deformation might also be reduced by inserting a heat support beneath an overhang.

(6) A general framework for overhang support structure design was found to be effective for overhang deformation minimization. It was demonstrated that the overhang deformation could be reduced with less material consumption by the combination of (a) heat support and (b) anchor design methods. Simulation examples have been presented to illustrate the design process.

9.2 Contributions of This Study

The contributions of this study are summarized below:

(1) The study correlates thermal information, mechanical response and part quality in powder bed additive manufacturing process.

(2) Numerical model has been developed to investigate the powder porosity and process parameter effects in EBAM process. The study would help to relate beam process parameters and EBAM part quality.

(3) A thermal model for SLM raster scan process has been developed to study the residual heat effect in a single scan patch. Using this model, the process parameters effect on melt pool evolution has been evaluated.

(4) Fundamental understanding of temperature, stress and deformation of EBAM overhang fabrications has been performed by thermomechanical model. The effect of different geometrical consideration of overhang and support structure has been investigated. Overhang support design method has been proposed to generate support structures with the minimum material usage to meet required constraint conditions.

9.3 Recommendations for Future Research

This study provides a fundamental understanding of the thermal response of powder bed additive manufacturing process. In addition, the thermomechanical modeling and overhang support design provide a framework for support generation with reduced material consumption. Future research can be pursued in the following directions:

(1) Current study has utilized thermal conduction model to investigate the temperature distribution, thermal history and melt pool of powder bed EBAM. Further efforts will be needed to focus on the melt pool fluid dynamics simulation. In addition, surface tension caused surface morphology should also be investigated so as to optimize the process parameters.

(2) In the current study, the SLM model was validated by literature data, thus further comprehensive validation is required to improve model prediction accuracy. NIR thermal imager will be utilized to collect thermal information, such as melt pool size (obtained based

on material phase change information), in SLM scanning/melting process. Current initial and boundary conditions need to be better defined by measured experiment results.

(3) The developed thermomechanical overhang model can only be used for temperature, stress and deformation trend prediction in EBAM process due to lack of experiment validation. Future study of this research will require build part stress measurements for comprehensive model validations. In addition, the separation of solidified overhang region and powder bed is not considered in the current overhang model, future work will need to include this feature. Future work will also investigate defect severity of different overhang patterns and study various configurations for designs of effective functional support structures for any specific types of overhang.